Buckling instabilities of semiflexible filaments in biological systems

Dissertation

zur Erlangung des akademischen Grades
Doktor der Naturwissenschaften (Dr. rer. nat.)
in der Wissenschaftsdisziplin Theoretische Physik

eingereicht an der
Mathematisch-Naturwissenschaftlichen Fakultät
der Universität Potsdam

angefertigt am
Max-Planck-Institut
für Kolloid- und Grenzflächenforschung Potsdam
Abteilung Theorie und Bio-Systeme

von

Krzysztof Konrad Baczyński

Potsdam, Mai 2009

Published online at the
Institutional Repository of the University of Potsdam:
URL http://opus.kobv.de/ubp/volltexte/2009/3792/
URN urn:nbn:de:kobv:517-opus-37927
[http://nbn-resolving.org/urn:nbn:de:kobv:517-opus-37927]

For my family

The mind is like a parachute.
It works only when it is open.

Frank Zappa

Abstract

We study buckling instabilities of filaments in biological systems. Filaments in a cell are the building blocks of the cytoskeleton. They are responsible for the mechanical stability of cells and play an important role in intracellular transport by molecular motors, which transport cargo such as organelles along cytoskeletal filaments. Filaments of the cytoskeleton are semiflexible polymers, i.e., their bending energy is comparable to the thermal energy such that they can be viewed as elastic rods on the nanometer scale, which exhibit pronounced thermal fluctuations. Like macroscopic elastic rods, filaments can undergo a mechanical buckling instability under a compressive load. In the first part of the thesis, we study how this buckling instability is affected by the pronounced thermal fluctuations of the filaments. In cells, compressive loads on filaments can be generated by molecular motors. This happens, for example, during cell division in the mitotic spindle. In the second part of the thesis, we investigate how the stochastic nature of such motor-generated forces influences the buckling behavior of filaments.

In Chapter 2 we review briefly the buckling instability problem of rods on the macroscopic scale and introduce an analytical model for buckling of filaments or elastic rods in two spatial dimensions in the presence of thermal fluctuations. We present an analytical treatment of the buckling instability in the presence of thermal fluctuations based on a renormalization-like procedure in terms of the non-linear sigma model where we integrate out short-wavelength fluctuations in order to obtain an effective theory for the mode the longest wavelength governing the buckling instability. We calculate the resulting shift of the critical force by fluctuation effects and find that, in two spatial dimensions, thermal fluctuations increase this force. Furthermore, in the buckled state, thermal fluctuations lead to an increase in the mean projected length of the filament in the force direction. As a function of the contour length, the mean projected length exhibits a cusp at the buckling instability, which becomes rounded by thermal fluctuations. Our main result is the observation that a buckled filament is stretched by thermal fluctuations, i.e., its mean projected length in the direction of the applied force increases by thermal fluctuations.

Our analytical results are confirmed by Monte Carlo simulations for buckling of semiflexible filaments in two spatial dimensions. We also perform Monte Carlo simulations in higher spatial dimensions and show that the increase in projected length by thermal fluctuations is less pronounced than in two dimensions and strongly depends on the choice of the boundary conditions.

In the second part of this work, we present a model for buckling of semiflexible filaments under the action of molecular motors. We investigate a system in which a group of motors moves along a firmly attached (immobilized) filament carrying a second filament as a cargo. The cargo-filament is pushed against the wall and eventually buckles. The force-generating motors can stochastically unbind and rebind to the filament during the buckling process. We formulate a stochastic model of this system and calculate the mean first passage time for the unbinding of all linking motors which corresponds to the transition back to the unbuckled state of the cargo filament in a mean-field model. Our results show that for sufficiently short microtubules the movement of kinesin-I-motors is affected by the load force generated by the cargo filament. Our predictions could be tested in future experiments.

Zusammenfassung

In dieser Arbeit werden Knickinstabilitäten von Filamenten in biologischen Systemen untersucht. Das Zytoskelett von Zellen ist aus solchen Filamenten aufgebaut. Sie sind für die mechanische Stabilität der Zelle verantwortlich und spielen eine große Rolle bei intrazellulären Transportprozessen durch molekulare Motoren, die verschiedene Lasten wie beispielsweise Organellen entlang der Filamente des Zytoskeletts transportieren. Filamente sind semiflexible Polymere, deren Biegeenergie ähnlich groß ist wie die thermische Energie, so dass sie auch als elastische Balken auf der Nanoskala gesehen werden können, die signifikante thermische Fluktuationen zeigen.

Wie ein makroskopischer elastischer Balken können auch Filamente eine mechanische Knickinstabilität unter Kompression zeigen. Im ersten Teil dieser Arbeit wird untersucht, wie diese Instabilität durch thermische Fluktuationen der Filamente beeinflusst wird. In Zellen können Kompressionskräfte durch molekulare Motoren erzeugt werden. Das geschieht zum Beispiel während der Zellteilung in der mitotischen Spindel. Im zweiten Teil der Arbeit untersuchen wir, wie die stochastische Natur einer von Motoren generierten Kraft die Knickinstabilität von Filamenten beeinflusst.

Zunächst stellen wir kurz das Problem von Knickinstabilitäten auf der makroskopischen Skala dar und führen ein Modell für das Knicken von Filamenten oder elastischen Stäben in zwei Raumdimensionen und in Anwesenheit thermischer Fluktuationen ein. Wir präsentieren eine analytische Lösung für Knickinstabilitäen in Anwesenheit thermischer Fluktuationen, die auf einer Renormierungsgruppenrechnung im Rahmen des nichtlinearen Sigma-Models basiert. Wir integrieren die kurzwelligen Fluktuationen aus, um eine effektive Theorie für die langwelligen Moden zu erhalten, die die Knickinstabilität bestimmen. Wir berechnen die Änderung der kritischen Kraft für die Knickinstabilität und zeigen, dass die thermischen Fluktuationen in zwei Raumdimensionen zu einer Zunahme der kritischen Kraft führen. Außerdem zeigen wir, dass thermische Fluktuationen im geknickten Zustand zu einer Zunahme der mittleren projizierten Länge des Filaments in Richtung der wirkenden Kraft führen. Als Funktion der Konturlänge des Filaments besitzt die mittlere projizierte Länge eine Spitze an der Knickinstabilität, die durch thermische Fluktuationen abgerundet wird. Unser Hauptresultat ist die Beobachtung, dass ein geknicktes Filament unter dem Einfluss thermischer Fluktuationen gestreckt wird, d.h. dass seine mittlere projizierte Länge in Richtung der Kompressionskraft auf Grund der thermischen Fluktuationen zunimmt.

Unsere analytischen Resultate werden durch Monte-Carlo Simulationen der Knickinstabilität semiflexibler Filamente in zwei Raumdimensionen bestätigt. Wir führen auch Monte-Carlo Simulationen in höheren Raumdimensionen durch und zeigen, dass die Zunahme der projizierten Länge unter dem Einfluss thermischer Fluktuationen weniger ausgeprägt ist und stark von der Wahl der Randbedingungen abhängt.

Im zweiten Teil der Arbeit formulieren wir ein Modell für die Knickinstabilität semiflexibler Filamente unter dem Einfluss molekularer Motoren. Wir untersuchen ein System, in dem sich eine Gruppe von Motoren entlang eines fixierten Filaments bewegt, und dabei ein zweites Filament als Last trägt. Das Last-Filament wird gegen eine Wand gedrückt und knickt. Während des Knickvorgangs können die Motoren, die die Kraft auf das Filament generieren, stochastisch von dem Filament ab- und an das Filament anbinden. Wir formulieren ein stochastisches Model für dieses System und berechnen die ”mean first passage time”, d.h. die mittlere Zeit für den Übergang von einem Zustand, in dem alle Motoren gebundenen sind zu einem Zustand, in dem alle Motoren abgebunden sind. Dieser Übergang entspricht auch einem Übergang aus dem gebogenen zurück in einen ungebogenen Zustand des Last-Filaments. Unser Resultat zeigt, dass für genügend kurze Mikrotubuli die Bewegung der Motoren von der durch das Last-Filament generierten Kraft beeinflusst wird. Diese Ergebnisse können in zukünftigen Experimenten überprüft werden.

Streszczenie

Badamy zjawisko odkształceń i wyboczeń półsztywnych filamentów w układach biologicznych. Filamenty w komórce są składowymi cytoszkieletu. Są odpowiedzialne za mechaniczną stabilność komórek i odgrywają ważną rolę w procesach transportu wewnątrz komórki, odbywających się dzięki motorom molekularnym, które transportują ładunki, takie jak organelle, wzdłuż filamentów cytoszkieletu. Filamenty te są półsztywnymi polimerami, tzn. ich energia zginania jest porównywalna z ich energią termiczną, a więc mogą być one postrzegane jako elastyczne pręty w skali mezoskopowej, które podlegają wyraźnym fluktuacjom termicznym. Tak jak makroskopowy elastyczny pręt, także filamenty mogą ulegać odkształceniom i wyboczeniom pod wpływem działającej siły, której kierunek jest równoległy do linii nieodkształconego pręta. W pierwszej części niniejszej pracy badamy jak wyraźne fluktuacje termiczne wpływają na taki proces wyboczania filamentu.

W komórkach siły związane z ładunkiem mogą być generowane przez motory molekularne. Tak dzieje się np. w trakcie podziału komórki w procesie mitozy. W drugiej części niniejszej rozprawy badamy jak stochastyczna natura sił generowanych przez te motory wpływa na zachowanie filamentów.

W przedstawionej pracy przeprowadzamy krótki przegląd problemu wyboczania prętów w skali makroskopowej i wprowadzamy analityczny model wyboczania filamentów lub elastycznych prętów w dwóch wymiarach przestrzennych w obecności fluktuacji termicznych. Prezentujemy analityczne podejście do procesów wyboczeń w obecności fluktuacji termicznych opartego na procedurze renormalizacji w ramach nieliniowego modelu sigma. W celu wprowadzenia efektywnej teorii dla modu o najdłuższej długości fali, opisującego niestabilność odkształceniową, odcałkowujemy fluktuacje krótkofalowe. Obliczamy przesunięcie siły krytycznej (siły Eulera) wskutek efektów fluktuacji i pokazujemy, że w przypadku dwóch wymiarów przestrzennych fluktuacje termiczne powodują wzrost wartości tej siły. Ponadto, w obecności fluktuacji termicznych w przypadku wyboczonego filamentu prowadzą one do wzrostu średniej długości rzutowanej filamentu na kierunek siły ściskakacej. Jako funkcja długości konturu filamentu, średnia długość rzutowana wykazuje ostry wierzchołek (ostrze krzywej), który zostaje zaokrąglony wskutek fluktuacji termicznych. Naszym głównym rezultatem jest obserwacja faktu, że fluktuujący wyboczony filament podlega rozciągnięciu, tzn. jego średnia długość rzutowana w kierunku przyłożonej siły wzrasta.

Nasze wyniki analityczne są potwierdzone za pomocą symulacji Monte Carlo dla wyboczeń półsztywnych filamentów w dwóch wymiarach przestrzennych. Wykonujemy także symulacje Monte Carlo dla wyższej liczby wymiarów przestrzennych i pokazujemy, że wzrost długości rzutowanej wskutek fluktuacji termicznych jest mniej wyrazisty niż w dwóch wymiarach oraz silnie zależy od wyboru warunków brzegowych.

W drugiej części niniejszej pracy prezentujemy model opisujący wyboczenia półsztywnych filamentów będących pod wpływem działania motorów molekularnych. Rozpatrujemy system, w którym grupa motorów porusza się wzdłuż nieruchomego filamentu transportując drugi filament jako ładunek, który jest oparty o ścianę i poddany sile ściskającej co prowadzi do jego wyboczenia. Motory generujące siłę mogą stochastycznie się odłączać oraz przyłączać do filamentu. Formujemy stochastyczny model dla takiego systemu i obliczamy średni czas pierwszego przejścia dla odłączenia się wszystkich łączących filamenty motorów, co dla filamentu będącego ładunkiem odpowiada przejściu ze stanu wyboczonego do nieodkształconego. Nasze wyniki pokazują, że dla wystarczająco krótkich mikrotubul ruch motorów jest podatny na zmiany pod wpływem siły obciążenia generowanej przez filament będący ładunkiem. Nasze przewidywania mogą być testowane w przyszłych eksperymentach.

Contents

Chapter 1

Introduction

Living organisms are very complex systems. Except very sophisticated, complex and still not completely understood biochemical processes, the living organism needs a well defined structure. This function is fulfilled by the cytoskeleton. The cytoskeleton plays also an important role in transport processes in cell. Various loads, like vesicles or organelles, are transported through the cell by molecular motors. These are complex molecules, which can move along the filaments driven by biochemical processes. Well investigated systems of molecular motor and corresponding filament are the kinesin motor on a microtubule and myosin on actin filament.

In this chapter we will present some basic knowledge on polymers, biological filaments and introduce a model of semiflexible polymers used in further parts of this thesis. We review shortly the molecular motors. We introduce also the parameters describing filaments which we will use in further parts of this thesis.

1.1 Cytoskeleton of Eucaryotic Cells

Just as buildings are supported by structural reinforcement, cells require a structural reinforcement. In eucaryotic cells this function is fulfilled by the *cytoskeleton*. Prokaryotes also have a cytoskeleton, though its genetic sequence is quite different from that of the eukaryote. In eukaryotic cells the cytoskeleton is a dynamic system of filaments. It builds the basic structure for cell. It provides not only the mechanical support for the structure of cells but also guide the intracellular transport processes of organelles, vesicles and other loads. One should also remember that also polymerization forces fulfill the role in motility processes in the cell.

The protein cytoskeleton is composed of *microfilaments*, *microtubules* and *intermediate filaments* connected by a three dimensional *microtrabecular lattice* (the network of filaments, tubules, and interconnecting filamentous bridges which give shape, structure, and organization to the cytoplasm and interconnect the cytoplasmic filaments). The microtrabecular lattice and intermediate filaments fulfill only constructive functions [1]. A schematic cartoon of a cell is presented in (a) in Fig. 1.1. The actin filaments are two-stranded helical polymers build by actin monomers [4]. The actin subunits assemble head-to-tail to generate filaments with a distinct structural polarity. Along actin filaments can move Myosin motor proteins. The intermediate filaments are fibers made of the intermediate filament proteins. The microtubules are long, hollow cylinders formed from 13 parallel protofilaments, each composed of alternating α- and β-tubulins. The inner diameter of a microtubule (MT) is 15 nm and the outer diameter is 25 nm. The length varies according to the function and polymerization and depolymerization processes. The polymerization of microtubules starts at *centrioles* or *basal bodies*. Two centrioles compose the *centrosome* which duplicates before *mitosis*. As mitosis proceeds from the two centrosomes on opposite sides of a dividing cell, the *mitotic spindle* grows up and joins with the *chromosomes*, structures with the cell's genetic information. For a complete description of the cell, see e.g. Refs. [1, 4].

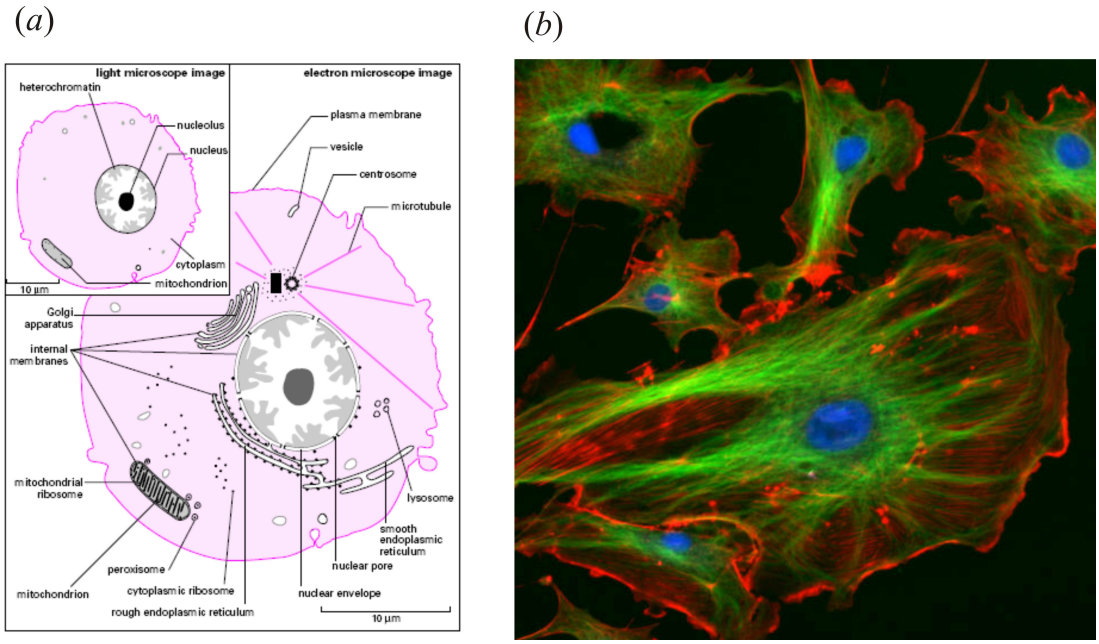

Figure 1.1: (a) Cell structure as seen through the light and transmission electron microscopes. From [2]. (b) The eukaryotic cytoskeleton. Actin filaments are shown in red, microtubules in green, and the nuclei are in blue. From [3].

The microtubules have a distinct structural polarity - they have a so-called plus and a minus end. The minus end is a germ at the organization center and the plus end is subjected to growth or shrinkage. The protofilaments of microtubules serve as paths for kinesin and dynein motor proteins.

1.2 Semiflexible Polymers and Filaments

We can find polymers everywhere - in nature and in industrial products. Examples are wood, silk, fibres, gels, synthetic polymers (called plastics), fibres and finally DNA straights. A polymer is a large molecule (macromolecule) composed of repeating structural units (monomers). In case of synthetic polymers the monomers are connected by the covalent chemical bonds.

The simplest model for a flexible polymer is to interpret the conformation of bonds as the path of a random walker with fixed step size. At finite temperature, a flexible polymer assumes a shape that maximizes the conformational entropy. For a complete description of flexible polymers, see e.g. Refs. [5, 6].

A polymer is called *semiflexible* if its persistence length L_p which is the length scale over which correlations in the orientation of single polymer segments decay is larger or of the order of its contour length L. The polymer can be considered as effectively flexible if $L > L_p$. In case of three spatial dimensions the persistence length L_p is given by the ratio of the intrinsic polymer *bending rigidity* κ and the thermal energy

$$L_p \equiv \frac{\kappa}{T} \ , \tag{1.1}$$

where T is measured in energy units, i.e., the Boltzmann constant k_B has been included in the symbol T. We will use this form of the persistence length in further parts of this thesis. This ratio characterizes the polymer's resistance to thermal forces arising from its bending rigidity. Note that there is renormalization of the bending rigidity in $d > 2$ spatial dimensions [7, 8]. In general the persistence length L_p depends also on the number of spatial dimensions and reads

$$L_p \equiv \frac{2}{d-1}\frac{\kappa_0}{T} \ , \tag{1.2}$$

where κ_0 denotes the unrenormalized bending rigidity. Semiflexible polymers behave as homogenous elastic rods on length scales comparable to their persistence length L_p, and their length is significantly larger than their diameter. This separation of length scales implies that architectural details, such as individual monomers and helical structure, can be neglected on the scale defined by L_p.

Semiflexible polymers play an important role in many biomaterials and biomimetic systems. From the biological point of view, a study of the mechanical and statistical properties of semiflexible filaments is important in order to understand the behavior of cytoskeletal networks.

For a polymer chain with a contour length that is comparable to its persistence length the two end bonds are always correlated. Such polymer chains may be regarded as semiflexible polymers. The statistical properties of semiflexible polymers are dominated by their bending rigidity and entropy. In the limit of large persistence lengths, a semiflexible polymer approaches a rigid rod. A useful model of a semiflexible polymer is the worm-like chain model presented in next section.

1.2.1 Examples

As mentioned in previous section, the cytoskeleton is made of various types of filaments. These filaments are so-called semiflexible filaments. Another example for a semiflexible polymer is provided by double-stranded DNA which is the carrier of genetic information and has the persistence length of order of 50 nm [9]. It is composed of two polynucleotide chains that form a right-handed double helical structure. A common example of synthetic polymer is polyethylene. Its backbone is a chain made up of carbon-carbon bonds and has an effective diameter of a few Ångström. Another example of a synthetic macromolecule which is a semiflexible polymer is a carbon nanotube. These promise a wide range of technical applications. The molecular structure of nanotubes resembles a single layer, that has been wrapped up into a seamless cylinder. In the same way, nanotubes consisting of several concentric layers can be fabricated. Accordingly, one speaks of single-walled and multi-walled nanotubes. Some examples of semiflexible polymers are presented in Fig. 1.2.
The semiflexible polymers presented schematically in Fig. 1.2 *a*) - *d*) occur only as open linear chains. This is not always the case. In fact, various types of filaments create closed loops (self-assemble), e.g. DNA minicircles [17] and amyloid fibrils [18]. Particularly for DNA this closed form is important for many biological processes, e.g. the genetic material of prokaryotes is stored in DNA rings. However, we will not consider such "looped" configurations in this thesis.

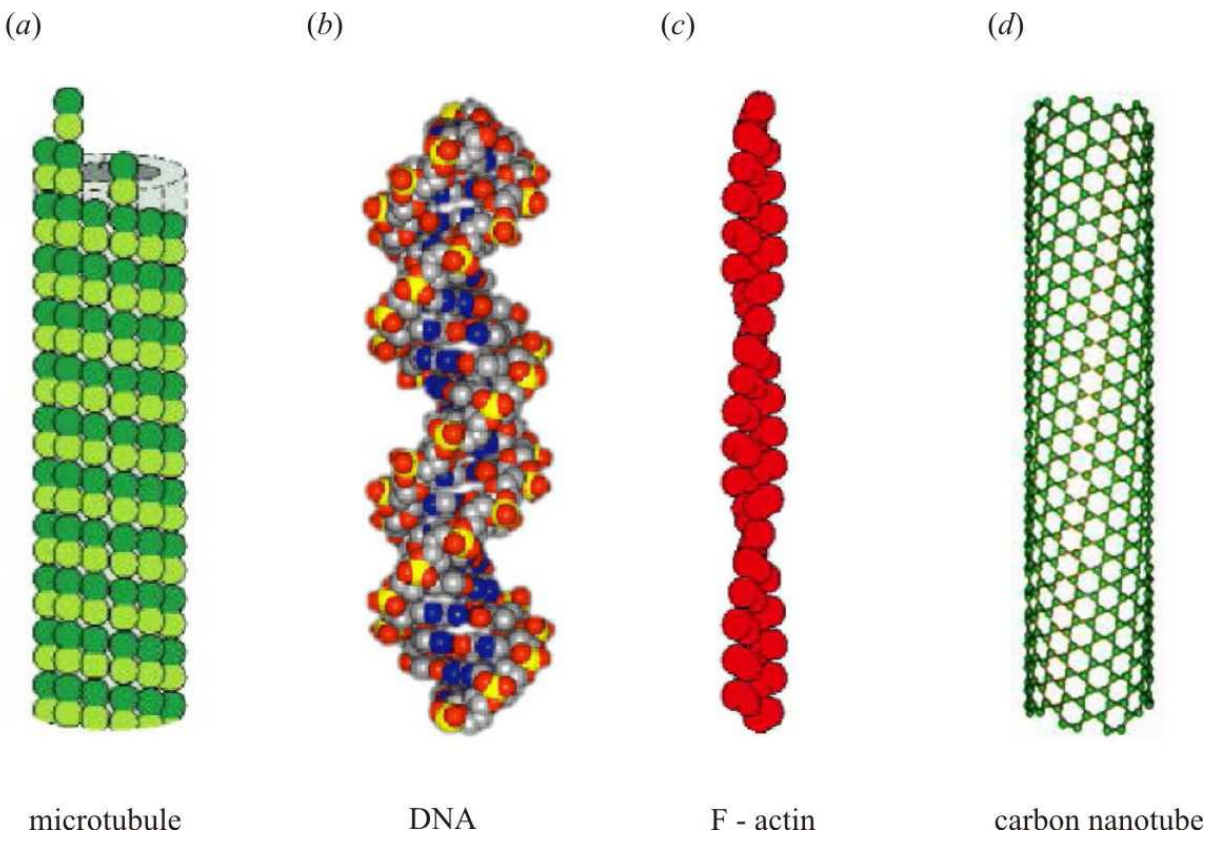

Figure 1.2: Examples of semiflexible polymers. *a*) microtubule with diameter $D = 25\ nm$ and $L_p = \sim 1-5\ mm$ [10, 11], *b*) double-stranded DNA with diameter $D = 2\ nm$ and $L_p = 50\ nm$ [12, 13], *c*) F-actin with diameter $D = 7\ nm$ and $L_p = 10\ \mu m$ [10, 14], *d*) carbon nanotube with diameter $D = 1 - 2\ nm$ and $L_p = 0.8\ \mu m$ [15, 16].

1.3 Polymer models

Many models have been proposed to describe the configurational properties of polymers during the last decades and a variety of methods have been employed to study these systems. We review shortly some of those models which are useful to describe statistical properties of a polymer. A very useful group of models of polymers are the *ideal chain models* [19]. We present here three of them.

We consider a polymer of $n+1$ backbone atoms A_i (with $0 \leqslant i \leqslant n$). We parametrize such a chain with bond vectors $\mathbf{r}_i$. We introduce the end-to-end vector as the sum of all n bond vectors in the chain:

$$\mathbf{R}_n = \sum_{i=1}^{n} \mathbf{r}_i. \tag{1.3}$$

It is useful to talk about average properties of the end-to-end vectors distribution.

If all bond vectors have the same length $l = |\mathbf{r}_i|$, the scalar product can be represented in terms of the angle θ_{ij} between bond vectors $\mathbf{r}_i$ and $\mathbf{r}_j$:

$$\mathbf{r}_i \cdot \mathbf{r}_j = l^2 \cos(\theta_{ij}). \tag{1.4}$$

The mean square end-to-end distance becomes a double sum of average cosines

$$\langle R^2 \rangle = \sum_{i=1}^{n} \sum_{j=1}^{n} \langle \mathbf{r}_i \cdot \mathbf{r}_j \rangle = l^2 \sum_{i=1}^{n} \sum_{j=1}^{n} \langle \cos(\theta_{ij}) \rangle, \tag{1.5}$$

where $\langle\ \rangle$ denotes the average over all possible states of the system.

1.3.1 The jointed chain model

One of the simplest models of an ideal polymer is the *freely jointed chain model* with a constant bond length $l = |\mathbf{r}_i|$. In terms of this model there are no correlations between the directions of different bond vectors, $\langle \cos\theta_{ij} \rangle = 0$ for $i \neq j$. The mean - square end-to-end distance of a freely jointed chain is simple and given by

$$\langle R^2 \rangle = \sum_{i=1}^{n} \sum_{j=1}^{n} \langle \mathbf{r}_i \cdot \mathbf{r}_j \rangle = nl^2, \tag{1.6}$$

However, in a typical polymer chain, there are correlations between bond vectors (especially between neighbouring ones) and $\langle \cos\theta_{ij} \rangle \neq 0$.

Flexible polymers have many universal properties that are independent of local chemical structure. A simple unified description of all ideal polymers is provided by an *equivalent freely jointed chain*. The equivalent chain has the same mean-square end-to-end distance $\langle R^2 \rangle$ and the same maximum end-to-end distance R_{max} as the actual polymer, but has N freely jointed effective bonds of length L_K. This effective bond length is called the *Kuhn length*. The contour length of this equivalent freely jointed chain is

$$NL_K = R_{max} \ . \tag{1.7}$$

The equivalent freely jointed chain has equivalent bonds (*Kuhn monomers*) of length

$$L_K = \frac{\langle R^2 \rangle}{R_{max}} \ . \tag{1.8}$$

1.3.2 The freely rotating chain model

As the name suggests, this model ignores differences between the probabilities of different torsion angles and assumes all torsion angles $-\pi < \varphi_i \leqslant \pi$ to be equally probably. The freely rotating chain model ignores the variations of the potential $U(\varphi_i)$. This model assumes all bond lengths and bond angles are fixed (constant) and all torsion angles are equally likely and independent of each other.

The correlations from bond vector $\mathbf{r}_j$ at bond vector $\mathbf{r}_i$ are reduced by the factor $(\cos\theta)^{|j-i|}$ due to independent free rotations of $|j - i|$ torsion angles between these two vectors so the correlation between bond vectors $\mathbf{r}_i$ and $\mathbf{r}_j$ is

$$\langle \mathbf{r}_i \cdot \mathbf{r}_j \rangle = l^2 (\cos\theta)^{|j-i|} \ . \tag{1.9}$$

The mean-square end-to-end distance of the freely rotating chain is a simple function of the number of bonds in the chain backbone n, the length of each backbone bond l and the bond angle θ and reads

$$\langle R^2 \rangle = nl^2 \frac{1 + \cos(\theta)}{1 - \cos(\theta)}. \tag{1.10}$$

Polymer chains are bever as flexible as the freely rotating chain model predicts because there is steric hindrance to bond rotation in all polymers [19].

1.3.3 The worm-like chain model

A widely used theoretical description of a semiflexible polymer is given by the *worm-like chain model* (*WLC*) presented by Kratky and Porod [20], and since then sometimes also called the Kratky-Porod model. The worm-like chain model is an extesion of the freely rotating chain model for very small values of the bond angle [5]. In this model, the neutral axis of the polymer is represented by a smooth space curve $\mathbf{r}(s)$ parametrized by the arc length s. The polymer's endpoints are at $s = 0$ and $s = L$, where L denotes the contour length of the polymer, see

Fig. 1.3. The arc length parametrization implies that the tangent vector $\mathbf{t}(s) \equiv \partial_s \mathbf{r}(s)$ (where $\partial_s \equiv \frac{\partial}{\partial s}$), has unit length. The bending energy is proportional to the square of the curvature of the space curve $\mathbf{r}(s)$ integrated over the contour length and the Hamiltonian of the WLC model is given by

$$\mathcal{H}_{WLC}\{\mathbf{t}(s)\} = \int_0^L ds \frac{\kappa}{2} (\partial_s \mathbf{t})^2 \tag{1.11}$$

with $\mathbf{t}^2(s) = 1$. This condition ensures the local and global inextensibility of semiflexible polymers within the WLC model. It also implies that only $d-1$ components of tangent vector are independent.

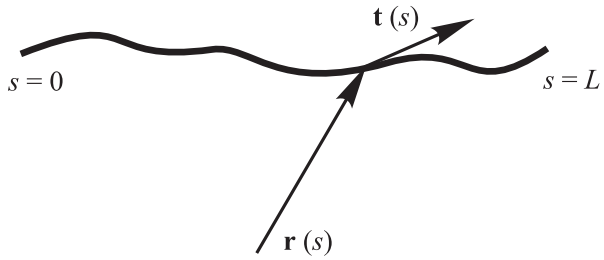

Figure 1.3: Schematic representation of a semiflexible polymer in the worm-like chain model.

On the basis of the WLC Hamiltonian (1.11), the persistence length L_p is defined as the length scale over which the correlation of tangent orientation decays [20, 21]. The corresponding correlation function is given by

$$\left\langle \mathbf{t}(s) \cdot \mathbf{t}(s') \right\rangle = e^{-\frac{|s-s'|}{L_p}} \tag{1.12}$$

and L_p is given by (1.2). The corresponding Kuhn length is twice the persistence length [19]

$$L_K = 2L_p. \tag{1.13}$$

For polymer with contour length $L < L_p$ the tangent vectors at the polymer ends would exhibit significant correlations, whereas they have little correlation for $L > L_p$.

At $T = 0$ semiflexible polymers assume a conformation of minimal bending energy with respect to appropriate boundary conditions. In case of $T = 0$ thermal fluctuations are small compared to the stiffness of the semiflexible polymer and the system is equilibrated. The stationary shapes of semiflexible polymers are found by solving the respective Euler-Lagrange equation, i.e., the first variation of $\mathcal{H}_{WLC}$ vanishes. Therefore, without further constraints, an open polymer gets a straight conformation.

1.4 Bending Rigidity of Rods and Filaments

If a single rod is not subjected to any external force his description follows with the help of (1.11). Then, the shape of the rod at $T = 0$ (no fluctuations) is completely described by the elastic energy and the only parameter is the **bending rigidity** κ, also called the **flexural rigidity**.

On the macroscopic scale, if a rod is made of an anisotropic and homogenous material, the bending rigidity can be separated into two terms - the Young's modulus, E_Y (a property of the material) and the second moment of inertia of the crosssection, I (determined by the shape of the rod) and given by

$$I \equiv \int dS_{\text{cross}} R^2 \ , \tag{1.14}$$

where S_{cross} indicates the area of the cross section and R is the distance of a point on the cross section to the neutral axis. The bending rigidity has units energy times length and reads

$$\kappa = E_Y \cdot I \ . \tag{1.15}$$

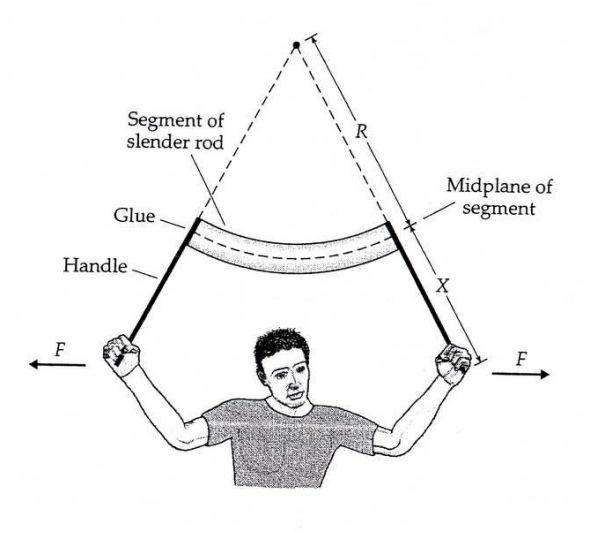

Figure 1.4: Bending of a slender rod due to a bending moment. From [22]. We grab a small length of rod and bent it into a circular arc as shown on the left. Provided that we don't apply too much force, the curvature of the bend, $1/R_c$ (R_c is the radius of curvature), will be proportional to the torque, or bending moment $M = F \cdot X$.

In biological and chemical systems, thermal fluctuations play an important role so that energies are commonly measured in units of T, where we use $k_B \equiv 1$ and the temperature is given in energy units.

The equation which relates the bending rigidity to the bending moment $M = F \cdot X$ (force times the distance), see Fig. 1.4, is the **beam equation**, and reads

$$M = \kappa \frac{1}{R_c} \ . \tag{1.16}$$

Here, R_c denotes the radius of curvature. The beam equation is analogous to Hook's law for a spring: the bending moment corresponds to force, the curvature to elongation and the bending rigidity is analogous to the spring constant.

1.5 Molecular Motors

Transport of organelles, vesicles and other loads trough the cell interior occurs thanks to molecular motors. Molecular motors are complicated protein complexes, as illustrated for the motors kinesin 1 and cytoplasmic dynein in Fig. 1.5.

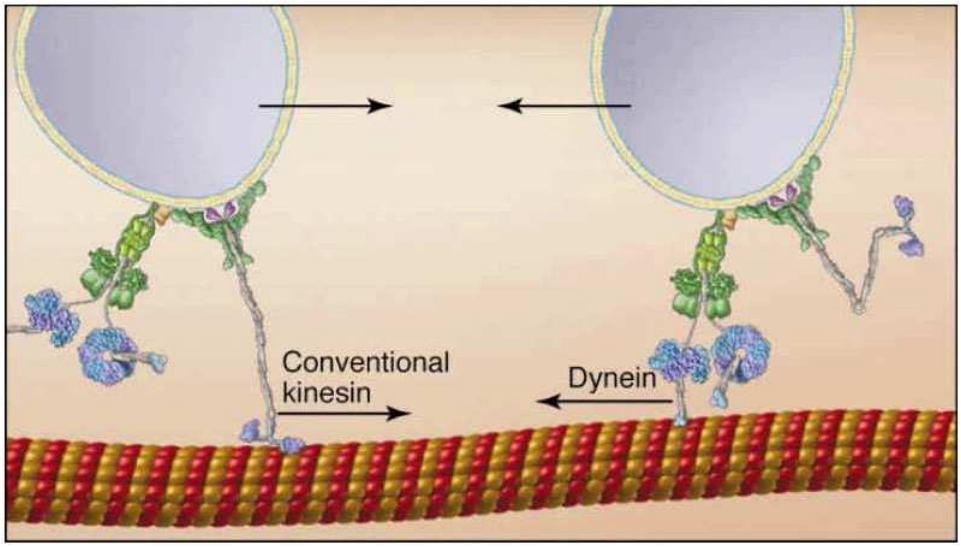

Figure 1.5: Cargo transport by molecular motors. Kinesin and dynein transport cargo to the microtubule plus and minus end, respectively. Both motors are complicated protein complexes. The main motor functionality is accomplished by two homodimerized heavy chains which form a stalk (gray). One of its ends binds to microtubule (blue) and the other to cargo (purple). Microtubule binding occurs at the heads (blue). Heads serve as feet during the motor steps forward. Cargo binding involves several light or intermediate chains (green). From [23].

Molecular motors walk along filaments. There are three types of motor proteins which can transport cargos: kinesin, dynein and myosin [1].

Kinesins are a large family of motor proteins which move along microtubules. Kinesins normally move to the plus end direction, some types of kinesin move, however, to the minus end direction and some move randomly to both directions. The structure of kinesin contains the core motor domain, the neck and two chains: the heavy chain and the light chain, see Fig. 1.5 and description there. The microtubule filament consists of 13 protofilaments aligned in parallel, each of which provides a track for the motor with a binding site every 8 nm so kinesins have a step size of 8 nm. Kinesin moves forward by a hand-over-hand mechanism (similar to a walking human) alternately throwing forward one of the two heads while the other remains bound to the microtubule. For each step, it consumes one ATP (Adenosine Triphosphate) molecule. The motor domain with the neck linker has a length of about 340 amino acids and contains the ATPase catalytic pocket and the major microtubule binding site.

Dyneins are another family of motor proteins moving along microtubules, normally to the minus end direction. They are composed of two or three heavy chains which include the motor domain and a large and variable number of associated light chains, see Fig 1.5. Dyneins also have the step size of 8 nm.

Myosins are motor proteins which can walk along actin filaments (processive myosins, i.e., Myosin V or VI) or not (non-processive myosins like Myosin V_c). Most of myosins is composed of a head domain which binds the actin filament and a tail domain which interacts with cargos or other myosin subunits. Processive myosins such as Myosin V or VI have the step size of 36 nm. Myosin motors play an important role during the muscle contraction [1].

The motors considered here act as *ATPases*, i.e., as enzymes that catalyze the hydrolysis of ATP into Adenosine Diphosphate ADP and inorganic phosphate P_i. The concentrations of ATP,

ADP and P_i are kept far from equilibrium in the cell. The hydrolysis releases a free energy of about 20 $k_BT \approx 80\ pN \cdot nm$ [22]. The motor uses this energy to move forward on the microtubule and accomplishes chemomechanical coupling - it converts chemical energy stored in the ATP molecule into mechanical motion. Thanks to this coupling the order of breaking and making bonds is not microscopically reversible.

1.6 Summary

In this chapter we presented the basic knowledge about polymers and filaments. We also reviewed shortly basic informations about molecular motors. We introduced basic parameters we will need in describing our theory of buckling of semiflexible polymers. This thesis is organized as follows. In the next chapter we will present the theory of buckling instabilities of rods in absence of thermal fluctuations. We will introduce such parameters as the critical buckling force (also called Euler force) and critical buckling length. Different cases of buckling depending on boundary conditions will be discussed and the projected length as function of applied force and as function of contour length will be plotted.

The third chapter will treat about buckling instabilities in the presence of thermal fluctuations. We will present an analytical solution for the case of two dimensions based on a renormalization-like procedure where we integrate out short-wavelength fluctuations in order to obtain an effective theory governing the buckling instability. We calculate the resulting shift of the critical force by fluctuation effects and the average projected filament length parallel to the force direction as a function of the applied force and of the contour length of the filament. Results presented in this chapter have been already presented in [8, 24].

The topic of the fourth chapter will be Monte Carlo simulations. Our analytic results from the third chapter are confirmed by Monte Carlo simulations, which also show that the increase in projected length by thermal fluctuations is less pronounced in higher dimensions and depends on the choice of boundary conditions.

In the fifth chapter we present a model of buckling a filament under the action of molecular motors. We introduce some basic knowledge about motors and parameters which we use in our approach. We estimate the mean first passage time after motors carrying a filament as a cargo detach from their path and the cargo-filament gets straight. We assume linear dependence of the load force on the position of the motors. We compare numerical results for a mean field theory results with results coming from numerical solution of simplified stochastic equations for the probability $p_n(t)$ that n motors link the cargo filament with the clamped filament at time t.

Finally, we end with a summary of discussed topics and an outlook on possible extensions and open questions for future work.

Chapter 2

Buckling instabilities in the absence of thermal fluctuations

In the previous chapter we presented a short review about the cytoskeleton, polymers and filaments and molecular motors walking along them. As already mentioned, all rods and filaments undergo a so-called buckling instability. In this chapter we will present a model of buckling instabilities of rods in the absence of thermal fluctuations, i.e., at $T = 0$ [25, 26, 27]. This simply corresponds to mechanical buckling on the macroscale. We will introduce basic parameters which will be used in further parts of this thesis. We will show that different boundary conditions lead to different values of these parameters.

The buckling instability problem is a common question in everyday life, for example in engineering problems like building of bridges or building's behavior under action of wind and other loads. The fact that under load a rod or plate [27] undergoes bending and buckling was investigated already by Leonardo da Vinci, see (a) in Fig. 2.1 [28]. In engineering, buckling is

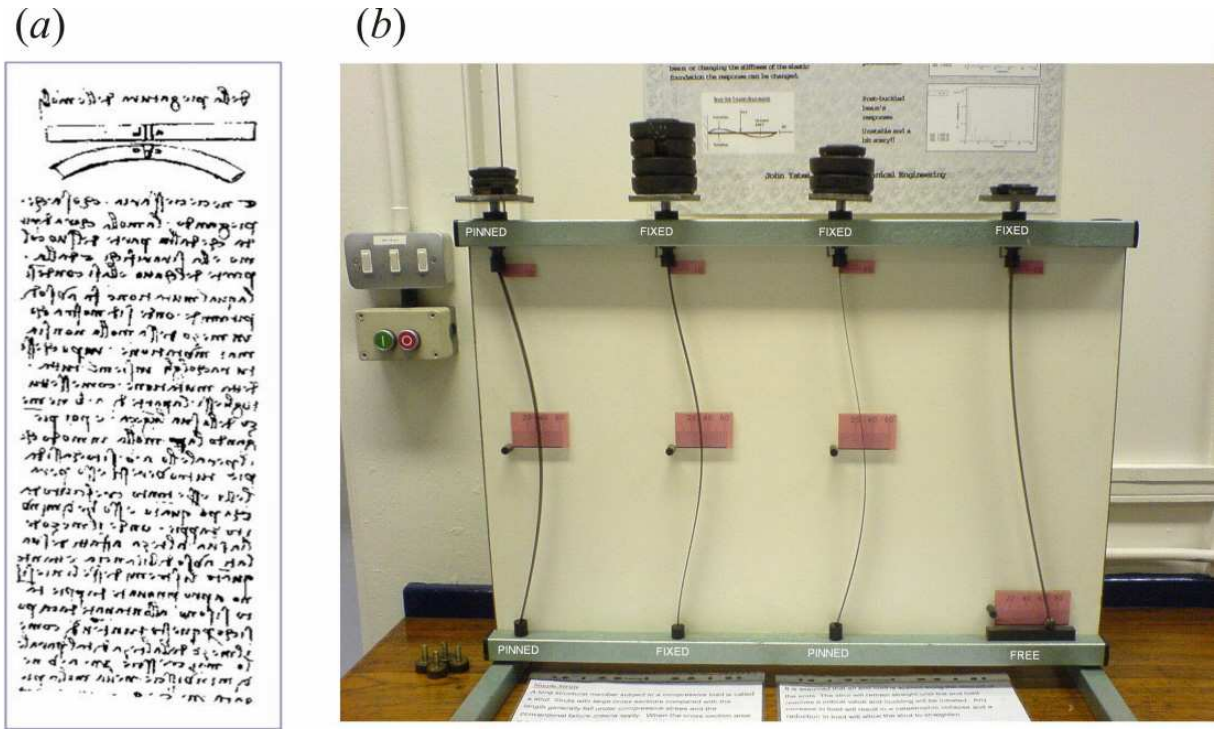

Figure 2.1: (a) A page from the Leonardo da Vinci's notebook treating the buckling problems considering bending of springs, from [28]. (b) An experimental setup presenting different behavior of a rod put under a compressional force depending on different boundary conditions. From [29].

a sudden failure of a structure subjected to high compressive stresses and refers to loss of the load-carrying capacity of a component within a structure or of the structure itself. Ultimate failure strength is one of the limit states that must be accounted for in structural engineering and structural designs, e.g. buildings or bridges. In reality, it is very easy to investigate the buckling instability of small systems like a single homogenous rod. Building an experimental setup one can consider defferent boundary conditions, see (b) in Fig. 2.1.

2.1 Model

We consider an inextensible, bendable rod in the two-dimensional xz-plane, i.e., $d = 2$, see Fig. 2.2. The rod has contour length L and is parametrized by its arc length s with $0 < s < L$. The buckling of a rod in three spatial dimensions occurs always in one direction and we can establish one plane and neglect the third (as well as higher) dimension because of the rotational symmetry. Therefore, we can always reduce the buckling instability of a rod in three spatial dimensions (at $T = 0$) to the case for two dimensions, and the description below treats the three dimensional case as well. In case of two spatial dimensions, $d = 2$, the shape of the rod can be

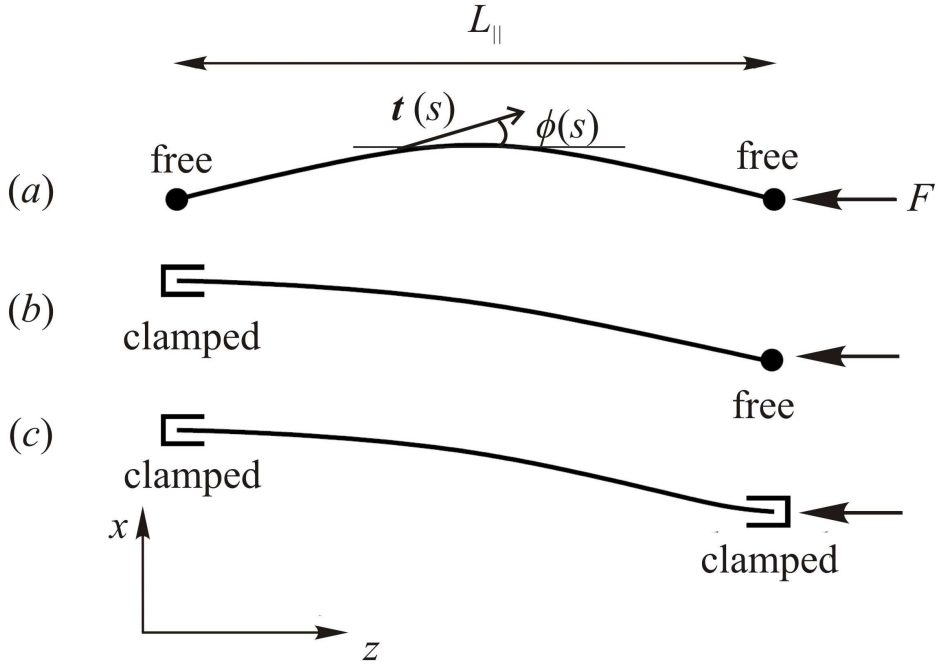

Figure 2.2: Different boundary conditions for a rod under compressional force F. Here, $\mathbf{t}(s)$ and $\phi(s)$ are the tangent vector and the tangent angle, respectively. $L_{||}$ denotes the projected length and $L_{||} = L$ before buckling and $L_{||} < L$ after buckling. (a) presents the case when both ends of the rod are free and the tangent vector $\mathbf{t}(s)$ is free to rotate. (b) shows the mixed boundary conditions: one end is free and the second end is clamped, i.e., $\phi\,|_{\text{end}}$ is given. (c) presents the case when the tangent vector at both ends are given and can not rotate - both ends are clamped.

parameterized by unit tangent vectors $\mathbf{t}(s) = (\cos\phi(s);\ \sin\phi(s))$ where $\phi(s)$ is their angle with the z-axis and s denotes the arc length. In this representation the elastic bending energy of the rod is given by

$$E_b = \int_0^L ds \frac{\kappa}{2} \left(\partial_s \phi(s)\right)^2 \ , \tag{2.1}$$

where κ is the bending rigidity (dimensions energy times length). A compression force F (dimensions energy over length) in z-direction ($\mathbf{F} = -F\hat{\mathbf{z}}$ with $F > 0$ giving a compression force)

gives rise to an additional energy

$$E_F = F L_{||} = F \int_0^L ds \cos\phi(s), \tag{2.2}$$

where

$$L_{||} \equiv \int_0^L ds \cos\phi(s) \tag{2.3}$$

is the *projected length* $L_{||}$ of the rod in the z-direction of the force with $L_{||} = L$ before buckling and $L_{||} < L$ after buckling. In further parts of this thesis this will be the most important observable we will use for description of buckling instabilities.

In mechanical equilibrium the shape of the rod is obtained by minimizing the total energy

$$E_b + E_F = \int_0^L ds \left[\frac{\kappa}{2} \left(\partial_s \phi(s)\right)^2 + F\cos\phi(s)\right] \tag{2.4}$$

with respect to the angles $\phi(s)$. Variation with respect to $\phi(s)$ gives the Euler-Lagrange equation

$$\kappa\, \partial_s^2 \phi(s) + F \sin\phi(s) = 0 \tag{2.5}$$

which has to be complemented by boundary conditions. The most common boundary conditions (bc's) are

$$\text{clamped ends:} \quad \phi\,|_{\text{end}} \ \text{ given} \tag{2.6}$$

$$\text{free ends:} \quad \partial_s \phi\,|_{\text{end}} = 0 \tag{2.7}$$

at each end, see Fig. 2.2. Clamped end means that the tangent vector $\mathbf{t}(s)$ can not rotate at this end and the bending moment does not vanish. The free end means the tangent vector $\mathbf{t}(s)$ can freely rotate at this end, i.e., the bending moment vanishes. There are also more complicated boundary conditions which pose additional restrictions on the positions of the end points, for example, we can require both ends to have the same x-coordinate (pinned end) during compression, see Figs. 2.1 (b) and 2.2. In this work we will consider only the case when at least one end is fixed. Otherwise the system would exhibit a zero mode corresponding to the translation (or diffusion) of the whole rod or filament perpendicular to the straight, unbent conformation.

In general case an inextensible rod in d spatial dimensions is governed by the general worm-like chain Hamiltonian (see Chapter 1) with the force term and is given by

$$\mathcal{H} = \int_0^L ds \left[\frac{\kappa}{2} \left(\partial_s \mathbf{t}(s)\right)^2 - \mathbf{F}\cdot\mathbf{t}(s)\right], \tag{2.8}$$

where s is the arc length and $\mathbf{t}(s)$ are the unit tangent vectors. For an inextensible rod considered here $|\mathbf{t}(s)| = 1$. $\mathbf{F}$ is a homogeneous external compressive force and the product $\mathbf{F}\cdot\mathbf{t}(s)$ is the compressional energy term.

2.2 Buckling instability for a rod with free ends

We can now start to investigate the buckling instability of a straight rod with both ends free (see Fig. 2.2, (a)) under a compressional force acting along the z axis. In this case equation (2.5) has to be solved with the following boundary conditions $\partial_s\phi(s=0) = \partial_s\phi(s=L) = 0$. Equation (2.5) can be interpreted as the equation of motion of a mathematical pendulum or of a particle of unit mass κ in ϕ-space within the external force field $-(F/\kappa)\sin\phi$ or within a potential $V(\phi) = -F\kappa\cos\phi$. Then, the first integral of (2.5) is the conserved energy C of this particle and reads

$$\frac{\kappa}{2}\left(\partial_s\phi(s)\right)^2 - F\cos\phi(s) = C\ . \tag{2.9}$$

Now, applying the boundary conditions for free ends (2.7) we find

$$C = -F\cos\phi(0) = -F\cos(L)\ . \tag{2.10}$$

In case of two free ends the solution has a mirror symmetry, i.e., $\phi(s) = -\phi(L-s)$ and thus also $\phi(0) = -\phi(L)$. This symmetry implies that $\phi(L/2) = 0$, i. e., the tangent vector at $L/2$ is parallel to the force vector.

There always exists the trivial solution $\phi(s) = 0$ representing the *unbuckled state*. To obtain possible non-trivial (*buckled*) solutions we solve starting from (2.9) by separation of variables

$$\begin{aligned} \partial_s\phi(s) &= -\left(\frac{2}{\kappa}(C + F\cos\phi(s))\right)^{1/2} \\ s &= \sqrt{\frac{\kappa}{2\ F}}\int_{\phi(s)}^{\phi(0)} \frac{d\phi}{(\cos\phi - \phi(0))^{1/2}}\ , \end{aligned} \tag{2.11}$$

where we assumed $\phi(0) > 0$ leading to $\phi(s) < \phi(0)$ and $\partial_s\phi(s) < 0$.

By setting $s = L$ (and using $\phi(L) = -\phi(0)$) or $s = L/2$ (and using $\phi(L/2) = 0$) in the solution (2.11) we obtain the relation between the *buckling angle* $\phi(0)$ and the parameter FL^2/κ,

$$\begin{aligned} \frac{L}{2} &= \sqrt{\frac{\kappa}{2\ F}}\int_0^{\phi(0)} \frac{d\phi}{(\cos\phi - \cos\phi(0))^{1/2}} \\ \sqrt{\frac{FL^2}{2\ \kappa}} &= \int_0^{\phi(0)} \frac{d\phi}{(\cos\phi - \cos\phi(0))^{1/2}} \equiv \mathcal{F}[\phi(0)], \end{aligned} \tag{2.12}$$

where the integral on the right hand side defines the function $\mathcal{F}[\phi(0)]$, which can also be expressed in terms of elliptic integrals (elliptic integral of the first kind) [30, 31]. If we consider the simple mathematical pendulum problem [30] and take ϕ as the angle between the spring and the vertical direction and use ϕ_{max} to denote the maximal value of ϕ, then $\mathcal{F}[\phi_{max}]$ defines the period (as the time required to go from $\phi = 0$ to $\phi = \phi_{max}$) of the pendulum. The arc length s from buckling problem corresponds to time t in the pendulum problem.

2.2.1 Critical force and critical length

$\mathcal{F}[\phi(0)]$ is a monotonously increasing function of $\phi(0)$ and takes on a positive value for $\phi(0) = 0$, which can be obtained by expanding the cosines in (2.12) in ϕ and $\phi(0)$,

$$\mathcal{F}[0] = \int_0^{\phi(0)} d\phi \frac{\sqrt{2}}{(\phi(0)^2 - \phi^2)^{1/2}} = \int_0^1 du \frac{\sqrt{2}}{(1-u^2)^{1/2}} = \frac{\pi}{\sqrt{2}}\ . \tag{2.13}$$

Therefore, any buckled solution with $\phi(0) > 0$ has to fulfill the inequality

$$\frac{FL^2}{\kappa} > 2F^2(0) = \pi^2. \tag{2.14}$$

For a given contour length L, the inequality can be fulfilled by increasing the force to

$$F > F_{c,0} \equiv \pi^2\frac{\kappa}{L^2}, \tag{2.15}$$

where $F_{c,0}$ denotes the *critical force* (also called *Euler force*) [27] which has to be exceeded to buckle the rod. Index 0 denotes that this solution corresponds to zero temperature. The critical force is contour length dependent and vanishes for an infinite long rod.

For a given force F, the inequality can be fulfilled by increasing the contour length to

$$L > L_{c,0} \equiv \pi\left(\frac{\kappa}{F}\right)^{1/2}, \tag{2.16}$$

i.e., for a contour length exceeding the critical value $L_{c,0}$ (which is force dependent).

Other boundary conditions are considered in the next sections and lead to the same parameter dependence but different numerical prefactors in expressions (2.15) and (2.16) for the critical force and critical contour length, respectively. Expanding the cosines in (2.12) to the fourth order we find

$$\begin{aligned}\mathcal{F}[\phi(0)] &= \mathcal{F}[0] + \frac{\phi^2(0)}{12}\int_0^1 du \frac{\left(1-u^4\right)}{\sqrt{2}\left(1-u^2\right)^{3/2}} + \mathcal{O}(\phi^4(0)) \\ &= \frac{\pi}{\sqrt{2}}\left(1+\frac{\phi^2(0)}{16}\right) + \mathcal{O}(\phi^4(0)). \end{aligned} \tag{2.17}$$

This expansion or numerical evaluation of the function $\mathcal{F}[\phi(0)]$ can be used to obtain the reduced force $F/F_{c,0}-1$ as a function of the buckling angle $\phi(0)$,

$$\begin{aligned}\frac{FL^2}{\kappa} &= 2\mathcal{F}^2[\phi(0)] \\ \frac{F}{F_{c,0}} - 1 &= \frac{\mathcal{F}^2[\phi(0)]}{\mathcal{F}^2[0]} - 1 \approx \frac{1}{8}\phi^2(0) \end{aligned} \tag{2.18}$$

or the reduced contour length $L/L_{c,0}-1$ as a function of the buckling angle $\phi(0)$,

$$\frac{L}{L_{c,0}} - 1 = \frac{\mathcal{F}[\phi(0)]}{\mathcal{F}[0]} - 1 \approx \frac{1}{16}\phi^2(0). \tag{2.19}$$

2.2.2 Projected length as a function of applied force

The projected length of the buckled solution is given by

$$\begin{aligned} L - L_{||} &= \int_0^L ds\,(1-\cos\phi(s)) \\ \sqrt{\frac{F}{2\kappa}}\left(L-L_{||}\right) &= \int_0^{\phi(0)} d\phi \frac{1-\cos\phi}{\left(\cos\phi-\cos\phi(0)\right)^{1/2}} \equiv \mathcal{G}[\phi(0)], \end{aligned} \tag{2.20}$$

where we used (2.11) and the mirror symmetry. This defines the function $\mathcal{G}[\phi(0)]$ [31].

The relations (2.12) and (2.20) give

$$1 - \frac{L_{||}}{L} = \sqrt{\frac{2\kappa}{FL^2}}\,\mathcal{G}[\phi(0)] = \frac{\mathcal{G}[\phi(0)]}{\mathcal{F}[\phi(0)]}, \tag{2.21}$$

which can be used together with relation (2.18) to obtain numerically a parametric plot of $1-L_{||}/L$ as a function of $F/F_{c,0}-1$, which is shown in Fig. 2.3 (red curve).

To obtain the behavior close to buckling analytically we expand the function $\mathcal{G}[\phi(0)]$ in ϕ and $\phi(0)$ in (2.20),

$$\begin{aligned}\mathcal{G}[\phi(0)] &= \int_0^{\phi(0)} d\phi \frac{\phi^2}{\sqrt{2}\left(\phi(0)^2-\phi^2\right)^{1/2}} + \mathcal{O}(\phi^4(0)) \\ &= \phi^2(0)\int_0^1 du \frac{u^2}{\sqrt{2}\left(1-u^2\right)^{1/2}} + \mathcal{O}(\phi^4(0)) \\ &\approx \frac{\pi}{4\sqrt{2}}\phi^2(0). \end{aligned} \tag{2.22}$$

Using the expansions (2.22) and (2.17) in (2.21) to expand in $\phi(0)$ and then employing (2.18), we find a linear dependence on $F/F_{c,0}-1 \ll 1$,

$$1 - \frac{L_{||}}{L} = \frac{\mathcal{G}[\phi(0)]}{\mathcal{F}[\phi(0)]} = \frac{1}{4}\phi^2(0) + \mathcal{O}(\phi^4(0)) \approx 2\left(\frac{F}{F_{c,0}} - 1\right). \tag{2.23}$$

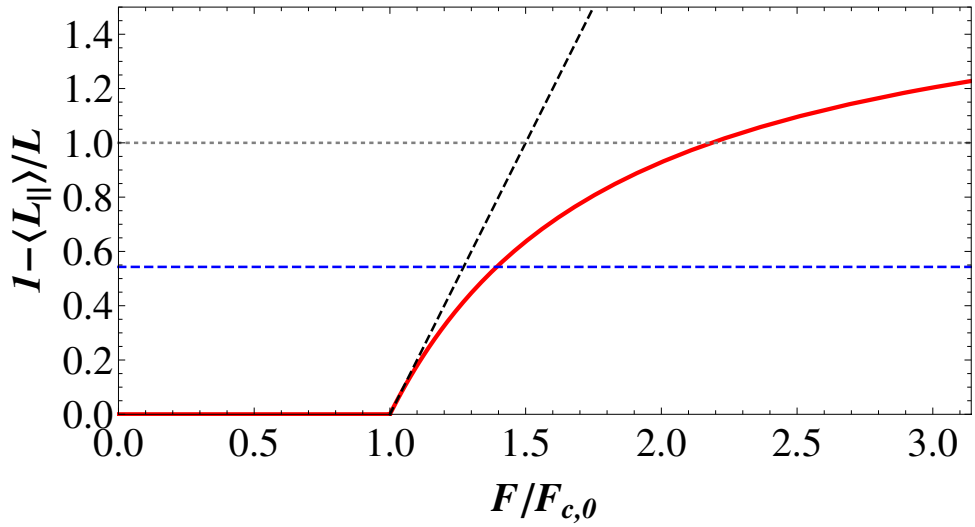

Figure 2.3: Plot of the reduced projected length $1 - L_{||}/L$ as a function of the reduced force $F/F_{c,0}$. The buckled solution appears for $F > F_{c,0}$ or $F/F_{c,0} > 1$, the unbuckled solution with $1 - L_{||}/L = 0$ does always exist. The red curve is obtained numerically by a parametric plot using (2.21) and (2.18) and $\phi(0)$ as parameter. The black dashed line is the linear approximation (2.23) valid for $F/F_{c,0} \ll 2$. For $1 - L_{||}/L > 1$ or $F/F_{c,0} > 2.183$, i.e., above the dotted gray line, $L_{||}$ becomes negative leading to "looped" configurations. For infinite forces $L_{||}$ approaches $-L$ or $1 - L_{||}/L \approx 2$. For the case when one end of the rod is free and the other is clamped the blue dashed line at $1 - L_{||}/L \simeq 0.543$ corresponds to the buckling angle $\phi(L) = \pi/2$.

Also this linear relation is shown in Fig. 2.3 as a black dashed line.

One can see that $L_{||}$ can become negative at large forces. Then the buckled conformations transforms into a **looped** configuration, i.e., the problem becomes equivalent to the problem of pulling on a looped rod, see Fig. 2.3. The problem of pulling of a looped rod will not be considered in this thesis. $L_{||} = 0$ corresponds to $1 - L_{||}/L = 1$; solving (2.21) numerically, we find that $L_{||} = 0$ corresponds to $\phi(0) \simeq 2.281$ and using (2.18), this corresponds to $F/F_{c,0} - 1 \simeq 1.183$ or $F \simeq 2.183\ F_{c,0}$.

For infinite forces, the buckling angle becomes $\phi(0) \approx \pi$, and the loop is "pulled" tight and reduces to zero in size leading to $L_{||} \approx -L$ or $1 - L_{||}/L \approx 2$. One can show that indeed $\mathcal{G}[\phi(0)]/\mathcal{F}[\phi(0)] \approx 2$ for $\phi(0) \approx \pi$.

The approximate solution (2.23) has a big advantage because it can be rewritten giving the analytical solution for reduced force $F/F_{c,0}$ as function of reduced projected length $1 - L_{||}/L$.

2.2.3 Projected length as a function of contour length

Alternatively, we can work at given force and use the relation (2.21) together with (2.19) in order to obtain parametrically the reduced projected length $1 - L_{||}/L$ as a function of the reduced contour length $L/L_{c,0} - 1$. In order to make one quantity L-independent it is more useful to consider the modified reduced projected length

$$\begin{aligned} 1 - \frac{L_{||}}{L_{c,0}} &= \left(1 - \frac{L_{||}}{L}\right)\frac{L}{L_{c,0}} - \left(\frac{L}{L_{c,0}} - 1\right) \\ &= \frac{\mathcal{G}[\phi(0)]}{\mathcal{F}[0]} - \frac{\mathcal{F}[\phi(0)]}{\mathcal{F}[0]} + 1 \\ &= \frac{\sqrt{2}}{\pi}\int_0^{\phi(0)} d\phi \frac{-\cos\phi}{(\cos\phi - \cos\phi(0))^{1/2}} + 1, \end{aligned} \tag{2.24}$$

where we used (2.19) and (2.21).

The result (2.24) together with (2.19) can be used to obtain numerically a parametric plot of $1 - L_{||}/L_{c,0}$ as a function of $L/L_{c,0} - 1$, which is shown in Fig. 2.4 (red curve).

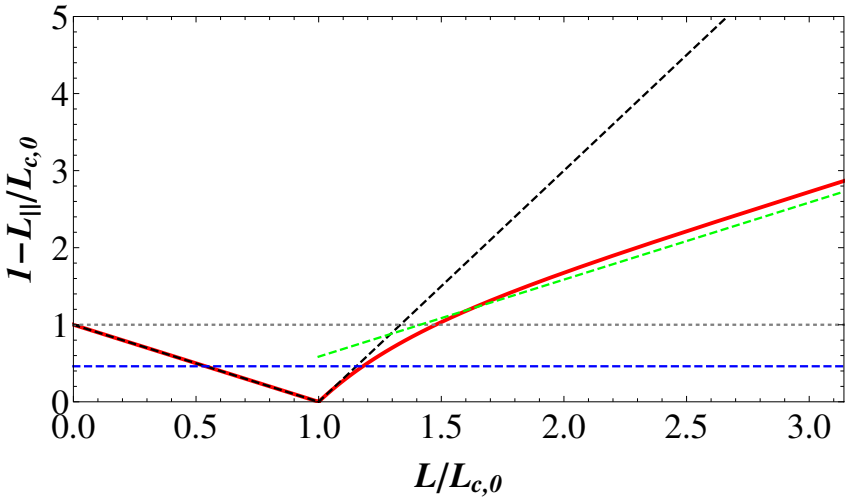

Figure 2.4: Plot of the reduced projected length $1 - L_{||}/L_{c,0}$ as a function of the reduced contour length $L/L_{c,0}$. The buckled solution (as sketched below the dashed line) appears for $L > L_{c,0}$ or $L/L_{c,0} - 1 > 0$, the unbuckled solution exists for $L/L_{c,0} < 1$ and has $L_{||} = L$. The red curve is obtained numerically by a parametric plot using (2.21) and (2.18) and $\phi(0)$ as parameter. The black dashed line is the linear approximation (2.25) valid for $L/L_{c,0} \ll 2$. For $1 - L_{||}/L_{c,0} > 1$ or $L/L_{c,0} > 1.478$, i.e., above the dotted gray line, $L_{||}$ becomes negative leading to "looped" configurations. For large lengths $L/L_{c,0}$, $1 - L_{||}/L_{c,0}$ approaches the linear asymptotics (2.29) as shown as dashed green line. For the case when one end of the rod is free and the other is clamped the blue dashed line at $1 - L_{||}/L_{c,0} \simeq 0.461$ corresponds to the buckling angle $\phi(L) = \pi/2$.

Using the expansions (2.22) and (2.17) in (2.24) to expand in $\phi(0)$ and then employing (2.19), we find a linear dependence on $0 < L/L_{c,0} - 1 \ll 1$,

$$\begin{aligned} 1 - \frac{L_{||}}{L_{c,0}} &= \frac{\mathcal{G}[\phi(0)]}{\mathcal{F}[0]} - \frac{\mathcal{F}[\phi(0)]}{\mathcal{F}[0]} + 1 = \frac{3}{16}\phi^2(0) + \mathcal{O}(\phi^4(0)) \\ &\approx 3\left(\frac{L}{L_{c,0}} - 1\right). \end{aligned} \tag{2.25}$$

Also this linear relation is shown in Fig. 2.4 (black dashed line).

These expressions are valid after buckling for $L/L_{c,0} - 1 > 0$. Before buckling, i.e., for $-1 \leqslant L/L_{c,0} - 1 < 0$ we have a straight rod with $L_{||} = L$ and, thus,

$$1 - \frac{L_{||}}{L_{c,0}} = -\left(\frac{L}{L_{c,0}} - 1\right). \tag{2.26}$$

The different behaviors in (2.25) and (2.26) give rise to the *cusp-like singularity* in the red curve in Fig. 2.4. For large contour length, the buckled conformations develop a **loop** exactly as discussed for large forces in the previous section. Then $L_{||}$ becomes negative or $1 - L_{||}/L_{c,0} > 1$; as discussed above $L_{||} = 0$ corresponds to $\phi(0) \simeq 2.281$ (from solving (2.21) numerically) and, using (2.18), to $L/L_{c,0} - 1 \simeq 0.478$ or $L \simeq 1.478\ L_{c,0}$.

For very large lengths L, the buckling angle approaches $\phi(0) \approx \pi$. Because we are working now at a given force, the "loop" cannot be pulled tight at large lengths L. It rather converges to a fixed loop length L_l, which can be obtained approximately by estimating and minimizing its energy cost E_l. We assume a circular loop with radius $R_l = L_l/2\pi$. E_l is the sum of bending and pulling energy, which is for a circular loop

$$E_l \approx \frac{\kappa}{2} L_l \frac{1}{R_l^2} + F L_l = 2\pi^2 \frac{\kappa}{L_l} + F L_l. \tag{2.27}$$

Minimizing (2.27) gives an optimal loop length

$$L_l = \sqrt{2}\pi \left(\frac{\kappa}{F}\right)^{1/2} = \sqrt{2} L_{c,0} \tag{2.28}$$

which is proportional to the critical length for buckling $L_{c,0}$. This suggests that we should obtain $L_{||} \approx -L + L_l$ or

$$1 - \frac{L_{||}}{L_{c,0}} \approx 1 + \frac{L}{L_{c,0}} - \frac{L_l}{L_{c,0}} \approx 2 - \sqrt{2} + \left(\frac{L}{L_{c,0}} - 1\right) \tag{2.29}$$

for large L. Fig. 2.4 shows that this linear asymptotics (green dashed line) is indeed a very good approximation for large L. Therefore, buckling instability at $T = 0$ close to critical force can be well described using the linear equations (2.25) and (2.26). For large forces one could use the approximation (2.29).

2.3 Buckling instability for a rod with clamped ends

Now, we consider a rod with both ends clamped, i. e., the bending moment vanishes and the boundary conditions are given by (2.6) and $\phi(0) = \phi(L) = 0$. For two clamped ends we have a mirror symmetry $\phi(s) = \phi(L - s)$ and, therefore, $\partial_s \phi(L/2) = 0$. Then we can establish a connection to the case of one clamped and one free end. The condition $\partial_s \phi(L = 2) = 0$ can be interpreted as a free boundary condition for a rod of half the size, and one half of a buckled rod with two clamped boundary conditions is equivalent to a buckled rod with one clamped and one free boundary conditions. In particular, the rod of length $2L$ with clamped boundary conditions has the same critical force as the rod of length L with one clamped and one free boundary condition, which leads to

$$F_{c,0} = \pi^2 \frac{\kappa}{L^2}, \tag{2.30}$$

i.e., the same result as for two free ends.

Using this analogy we can find

$$\begin{aligned} \frac{L}{2} &= \sqrt{\frac{\kappa}{2\ F}} \int_0^{\phi(L/2)} \frac{d\phi}{(\cos\phi - \cos\phi(L/2))^{1/2}} \\ \sqrt{\frac{FL^2}{2\ \kappa}} &= \int_0^{\phi(L/2)} \frac{d\phi}{(\cos\phi - \cos\phi(L/2))^{1/2}} \equiv \mathcal{F}[\phi(L/2)], \end{aligned} \tag{2.31}$$

where the function $F[\phi(L = 2)]$ is defined as previously in (2.12). Any buckled solution has to fulfill the inequality $FL^2 = 2\kappa > F^2[0]$. Using $F[0] = \pi/\sqrt{2}$, see (2.13), this leads to the above result (2.30) for the critical force $F_{c,0}$. For a given force F, we find analogously the critical contour length

$$L_{c,0} = \pi \sqrt{\frac{\kappa}{F}} \tag{2.32}$$

as for two free ends.

We can now use the expansion (2.17) and obtain the reduced force $F/F_{c,0} - 1$ as a function of the buckling angle $\phi(L/2)$, which leads to the same result (2.18) as for free bc's (with the buckling angle $\phi(L/2)$ instead of $\phi(0)$)

$$\begin{aligned} \frac{FL^2}{\kappa} &= 2\ \mathcal{F}^2[\phi(L/2)] \\ \frac{F}{F_{c,0}} - 1 &= \frac{\mathcal{F}^2[\phi(L/2)]}{\mathcal{F}^2[0]} - 1 \approx \frac{1}{8}\phi^2(L/2) \end{aligned} \tag{2.33}$$

or the reduced contour length $L/L_{c,0} - 1$ as a function of the buckling angle $\phi(L/2)$, which also leads to the same result (2.19) as for free bc's,

$$\frac{L}{L_{c,0}} - 1 = \frac{\mathcal{F}[\phi(L/2)]}{\mathcal{F}[0]} - 1 \approx \frac{1}{16}\phi^2(L/2)\ . \tag{2.34}$$

2.3.1 Projected length as a function of force (both ends clamped)

The projected length of the buckled solution

$$\begin{aligned} \frac{1}{2}\left(L - L_{||}\right) &= \int_0^{L/2} ds\,(1-\cos\phi(s)) \\ \sqrt{\frac{F}{2\,\kappa}}\left(L - L_{||}\right) &= \int_0^{\phi(L/2)} d\phi \frac{1-\cos\phi}{(\cos\phi - \cos\phi(L/2))^{1/2}} \equiv \mathcal{G}[\phi(L/2)] \end{aligned} \tag{2.35}$$

with the function $\mathcal{G}[\phi(L=2)]$ defined as previously in (2.20). The relations (2.31) and (2.35) give

$$1 - \frac{L_{||}}{L} = \sqrt{\frac{2\,\kappa}{F\,L^2}}\,\mathcal{G}[\phi(L/2)] = \frac{\mathcal{G}[\phi(L/2)]}{\mathcal{F}[\phi(L/2)]} \tag{2.36}$$

which is **the same** relation as (2.21) and can be used together with relation (2.42) to obtain numerically a parametric plot of $1 - L_{||}/L$ as a function of $F/F_{c,0} - 1$. Because both (2.36) and (2.33) are identical to their counterparts (2.21) and (2.18) for two free ends also the resulting plot is identical to Fig. 2.3 (red curve).

Also the projected length as a function of contour length is identical with solution for two free ends and the resulting plot is identical to Fig. 2.4 (red curve).

2.4 Buckling instability for a rod with one end clamped and one end free

Now, we consider the case where one end is clamped, i.e., $\phi(0) = 0$ and the other end is free, $\partial_s\phi(L) = 0$. Applying these boundary conditions into the first integral C, see eq. (2.9), we find

$$C = \frac{1}{2}\kappa\,(\partial_s\phi(0))^2 = -F\cos(L)\ . \tag{2.37}$$

2.4.1 Critical force and critical length

For one clamped and one free end, the mirror (anti-)symmetry $\phi(s) = -\phi(L-s)$ of the problem with two free ends is lost. However, both types of problems are intimately related. With two free ends the mirror symmetry always leads to $\phi(L/2) = 0$, which can be interpreted as a clamped boundary condition for a rod of half the size. Therefore one half of a buckled rod with two free boundary conditions behaves in the same way as a buckled rod with one clamped and one free boundary conditions. In particular, the rod of length $2L$ with free boundary conditions has the same critical force as the rod of length L with one clamped and one free boundary condition, which leads to

$$F_{c,0} = \frac{\pi^2}{4}\frac{\kappa}{L^2}. \tag{2.38}$$

Again, there always exists the trivial solution $\phi(s) = 0$ representing the unbuckled state. To obtain possible non-trivial (buckled) solutions we solve starting from (2.9) by separation of variables

$$\begin{aligned} \partial_s\phi &= \left(\frac{2}{\kappa}(C + F\cos\phi)\right)^{1/2} \\ s &= \sqrt{\frac{\kappa}{2F}}\int_{\phi(s)}^{\phi(L)} \frac{d\phi}{(\cos\phi(L) - \cos\phi)^{1/2}}\ , \end{aligned} \tag{2.39}$$

where we assumed $\phi(L) > 0$ leading to $\phi(s) < \phi(L)$ and $\partial_s\phi > 0$. By setting $s = 0$ (and using $\phi(0) = 0$) in the solution (2.11) we obtain the relation between the buckling angle $\phi(L)$ at the

free end and the parameter FL^2/κ,

$$\begin{aligned} L &= \sqrt{\frac{\kappa}{2F}} \int_0^{\phi(L)} \frac{d\phi}{(\cos\phi - \cos\phi(L))^{1/2}} \\ \sqrt{\frac{2FL^2}{\kappa}} &= \int_0^{\phi(L)} \frac{d\phi}{(\cos\phi - \cos\phi(L))^{1/2}} \equiv \mathcal{F}[\phi(L)], \end{aligned} \tag{2.40}$$

where the function $\mathcal{F}[\phi(L)]$ is defined as previously in (2.12).

Any buckled solution has to fulfill the inequality $2FL^2/\kappa > \mathcal{F}^2[0]$. Using $\mathcal{F}[0] = \pi/\sqrt{2}$, see (2.13), this leads to the above result (2.38) for the critical force $F_{c,0}$. For a given force F, we find analogously the critical contour length

$$L_{c,0} = \frac{\pi}{2} \left(\frac{\kappa}{F}\right)^{1/2}. \tag{2.41}$$

We can use the expansion (2.17) to obtain the the reduced force $F/F_{c,0} - 1$ as a function of the buckling angle $\phi(L)$, which leads to **the same result** (2.18) as for both ends with free bc's (with the buckling angle $\phi(L)$ instead of $\phi(0)$)

$$\begin{aligned} \frac{FL^2}{\kappa} &= \frac{\mathcal{F}^2[\phi(L)]}{2} \\ \frac{F}{F_{c,0}} - 1 &= \frac{\mathcal{F}^2[\phi(L)]}{\mathcal{F}^2[0]} - 1 \approx \frac{1}{8}\phi^2(L) \end{aligned} \tag{2.42}$$

or the reduced contour length $L/L_{c,0} - 1$ as a function of the buckling angle $\phi(L)$, which also leads to the same result (2.19) as for both ends free bc's,

$$\frac{L}{L_{c,0}} - 1 = \frac{\mathcal{F}[\phi(L)]}{\mathcal{F}[0]} - 1 \approx \frac{1}{16}\phi^2(L). \tag{2.43}$$

2.4.2 Projected length as a function of applied force

The projected length of the buckled solution

$$\begin{aligned} L - L_{||} &= \int_0^L ds\,(1 - \cos\phi(s)) \\ \sqrt{\frac{2F}{\kappa}}\,(L - L_{||}) &= \int_0^{\phi(L)} d\phi \frac{1 - \cos\phi}{(\cos\phi - \cos\phi(L))^{1/2}} \equiv \mathcal{G}[\phi(L)] \end{aligned} \tag{2.44}$$

with the function $\mathcal{G}[\phi(L)]$ defined as previously in (2.20). The relations (2.40) and (2.44) give

$$1 - \frac{L_{||}}{L} = \sqrt{\frac{\kappa}{2FL^2}}\ \mathcal{G}[\phi(L)] = \frac{\mathcal{G}[\phi(L)]}{\mathcal{F}[\phi(L)]} \tag{2.45}$$

which is the same relation as (2.21) and can be used together with relation (2.42) to obtain numerically a parametric plot of $1 - L_{||}/L$ as a function of $F/F_{c,0} - 1$. Because both (2.45) and (2.42) are identical to their counterparts (2.21) and (2.18) for two free ends also the resulting plot is identical and is presented in Fig. 2.3 (red curve). The discussion of the linear behaviour for small buckling angles $\phi(L)$ as well as the discussion of the "looping" for negative $L_{||}$ is exactly the same as for the case of free ends. One interesting question for this geometry is at which force a buckling angle $\phi(L) = \pi/2$ is attained. Using (2.45) and (2.42) we find that $\phi(L) = \pi/2$ corresponds to $1 - L_{||}/L \simeq 0.543$ or $L_{||} = 0.457\ L$ and $F/F_{c,0} - 1 \simeq 0.393$ or $F \simeq 1.393\ F_{c,0}$. This corresponds to the blue dashed line in Fig. 2.3.

If the filament polymerizes against a wall which is exerting the force F, the filament can polymerize without having to push the wall further away for buckling angles $\phi(L) > \pi/2$, i.e., above the lower dashed line in Fig. 2.3.

2.4.3 Projected length as a function of length

We can also obtain the projected length as a a function of the contour length. Using (2.43) and (2.45) we find for the reduced projected length

$$\begin{aligned} 1 - \frac{L_{||}}{L_{c,0}} &= \left(1 - \frac{L_{||}}{L}\right) \frac{L}{L_{c,0}} - \left(\frac{L}{L_{c,0}} - 1\right) \\ &= \frac{\mathcal{G}[\phi(L)]}{\mathcal{F}[0]} - \frac{\mathcal{F}[\phi(L)]}{\mathcal{F}[0]} + 1 \end{aligned} \tag{2.46}$$

the same result as in (2.24) for two free ends. Because also (2.43) is identical to the result (2.19) for two free ends also the resulting plot is identical to Fig. 2.4 (red curve). The discussion of the linear behaviour for small buckling angles $\phi(L)$ as well as the discussion of the "looping" for negative $L_{||}$ is exactly the same as for the case of free ends. The buckling angle $\phi(L) = \pi/2$ is attained for $1 - L_{||}/L_{c,0} \simeq 0.461$ or $L_{||} = 0.539\ L_{c,0}$ and $L/L_{c,0} - 1 \simeq 0.180$ or $L \simeq 1.180\ L_{c,0}$. This corresponds to the blue dashed line in Fig. 2.4.

2.5 Summary

One can see that the projected length as a function of applied force or projected length as function of contour length presented in Fig. 2.3 and 2.4 look the same and the only difference is included in the value of critical force or critical length, respectively.

For purpose of simplicity and clearness in further parts of this thesis we introduce two dimensionless parameters

$$\bar{F} \equiv F/F_{c,0} \tag{2.47}$$

$$\bar{L} \equiv L/L_{c,0} \tag{2.48}$$

for reduced force and reduce length, respectively. Here, both critical values are taken at $T = 0$.

In this chapter we presented a model of buckling of rods in two spatial dimensions in absence of thermal fluctuations. We introduced several important parameters, like projected length $L_{||}$, critical force $F_{c,0}$, critical length $L_{c,0}$, and presented the force - extension curves for buckling instabilities which looks identical for different boundary conditions. We investigated three cases of boundary conditions. In the next chapter we will consider an analogous model of buckling but in presence of thermal fluctuations, i.e., $T > 0$. We will show, that a thermal fluctuating filament in two dimensional space behaves different and thermal fluctuations lead to change of parameters introduced in this chapter.

Chapter 3

Buckling instabilities in two dimensional space in the presence of thermal fluctuations

In the previous chapter we presented a short review about buckling instabilities on the macro scale. In this chapter we will study the buckling instability of filaments or elastic rods in two spatial dimensions in the presence of thermal fluctuations, i.e., at $T > 0$. We will present an analytical solution based on a renormalization-like procedure where we integrate out short-wavelength fluctuations in order to obtain an effective theory governing the buckling instability. We calculate the resulting shift of the critical force by fluctuation effects and the average projected filament length parallel to the force direction as a function of the applied force and of the contour length of the filament.

We find that, in the buckled state, thermal fluctuations lead to an *increase* in the mean projected length of the filament in the force direction. As a function of the contour length, the mean projected length exhibits a cusp at the buckling instability, which becomes rounded by thermal fluctuations.

Recently three other papers were published [32, 33, 34]. Lee *et all* in [32] established the same result as in [24]. The approach of Emanuel *et all* [33] does not give any insight into the shift of the critical force for buckling. Blundell *et all* in [34] investigate semiflexible filaments in three spatial dimensions using a mean-field approximation to filament inextensibility and show that the critical force decreases for filaments in a thermal environment.

3.1 Introduction

Buckling of elastic rods is a ubiquitous mechanical problem, which is relevant in elasticity theory and mechanical engineering [27]. An elastic rod undergoes a buckling instability if the compressional force F exceeds a certain threshold value, the critical force F_c, for constant rod length or if the rod length L exceeds a certain critical length L_c for constant force. Such buckling instabilities also play a role in biological systems, whenever rigid filaments or semiflexible polymers, such as cytoskeletal filaments or DNA, are under a compressive load. In a living cell compressive loads can be generated by the ATP or GTP driven polymerization of filaments or by molecular motors, which are also driven by the hydrolysis of ATP [22]. Both processes can generate forces in the piconewton range. On the other hand, biological nanorods also show pronounced thermal shape fluctuations, which give rise to a number of interesting cooperative phenomena [35]. Therefore, thermal fluctuations should influence the buckling behavior of filaments as well.

It has been shown experimentally that polymerization forces are sufficient to buckle microtubules of micrometer length [36]. In Ref. [36], the shape of buckled microtubules growing against a hard obstacle has been analyzed to measure microtubule polymerization forces, which

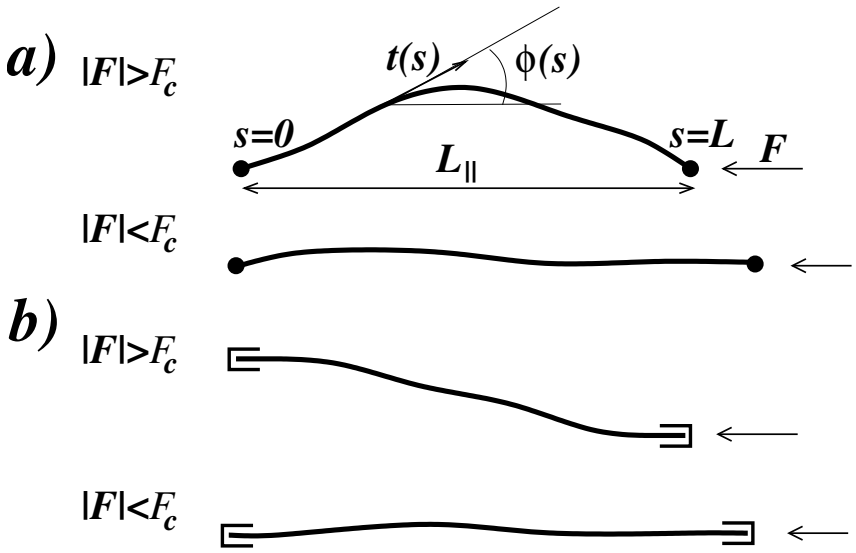

Figure 3.1: Thermally fluctuating filament under a compressive force $\mathbf{F}$ for (a) free and (b) clamped boundary conditions at both ends. For absolute values $|\mathbf{F}|$ of the force larger than the critical buckling force F_c the filament is buckled, for forces smaller than F_c it remains unbuckled. The filament has contour length L, and $\mathbf{t}(s)$ is the unit tangent vector and $\phi(s)$ the corresponding tangent angle at arc length s. $L_\parallel$ is the projected length in force direction.

were found to lie in the piconewton range. Forces in the piconewton range can also be generated by motor proteins, and it has also been demonstrated experimentally that molecular motors can buckle microtubules of micrometer length [37]. Experiments on microtubules growing inside lipid vesicles demonstrate that microtubules also buckle under the compressive forces exerted by a lipid bilayer under tension [38]. All these experiments show that small forces in the piconewton range are sufficient to buckle cytoskeletal filaments. Such small buckling forces suggest that additional thermal forces, which also generate piconewton forces on a nanometer scale, where $1k_BT \approx 4\ pN \cdot nm$, could modify the buckling instability considerably.

Some extensions of the classical buckling instability have been already considered before. The buckling of twisted filaments, which is relevant to many biological filaments, has been studied in Ref. [39]. For charged polymers the buckling instability is related to the collapse of a stiff polyelectrolyte under the action of attractive intra-chain interactions, which has also been analyzed in the presence of thermal fluctuations [40]. Also the dynamics of buckling rods has been investigated theoretically [41, 42].

The effect of thermal fluctuations on the buckling instability, on the other hand, has received much less attention. The strength of thermal fluctuations of semiflexible polymers is characterized by their persistence length $L_p = \kappa/T$ [7], see Chapter 1. On length scales larger than the persistence length a semiflexible polymer decays into uncorrelated Kuhn segments of length $2L_p$ and becomes an effectively flexible polymer with no resistance to buckling, i.e., the critical buckling force vanishes. In this chapter of the thesis, we will focus on the semiflexible regime $L \ll L_p$, where the buckling instability is still governed by a nonzero threshold force but strongly modified by thermal fluctuations. The only discussion of thermal fluctuations on the buckling instability has been given by Odijk [43] in the framework of a harmonic approximation for filaments in three spatial dimensions. In a similar semiclassical approximation the influence of quantum fluctuations on buckling instabilities has been studied [44].

In this chapter, we will systematically consider the influence of anharmonic corrections for buckling in two spatial dimensions, which can be realized experimentally in confined geometries, i.e., for filaments adsorbed or confined to a planar substrate. We use a systematic expansion in the ratio L/L_p of contour length to persistence length, and integrate out small scale fluctuations

to obtain an effective theory governing the buckling instability. We calculate the shift of the buckling force in the presence of thermal fluctuations and find that the buckling force *increases* in two dimensions in contrast to the perturbative result of Odijk for three spatial dimensions [43].

We also calculate the mean projected length as a function of the applied force (at fixed contour length) and as a function of the contour length (at fixed applied force) in the presence of thermal fluctuations. Our results show that thermal fluctuations lead to a *stretching* of buckled filaments, whereas they compress unbuckled filaments.

3.2 Model

An inextensible semiflexible polymer or filament of contour length L in d spatial dimensions is governed, as already mentioned in Chapter 1, by the general worm-like chain Hamiltonian as given by

$$\mathcal{H} = \int_0^L ds \left[\frac{\kappa}{2} (\partial_s \mathbf{t}(\mathbf{s}))^2 - \mathbf{F} \cdot \mathbf{t}(s) \right], \tag{3.1}$$

where s is the arc length and $\mathbf{t}(s)$ are the unit tangent vectors of the contour with $|\mathbf{t}(s)| = 1$, see Fig. 3.1. $\mathbf{F}$ is a homogeneous external force, which will be taken to be compressive in the following. The Hamiltonian (3.1) only contains contributions from the bending energy and the external force and applies to inextensible filaments without torsional degrees of freedom. In the figure the unbuckled filament is not exactly straight when compared to the Fig. 2.2 because of the thermal fluctuations.

There is a close analogy between the Hamiltonian (3.1) for a filament in d spatial dimensions and a one-dimensional magnetic system of d-component magnetic spins. The Hamiltonian (3.1) with the constraint $|\mathbf{t}(s)| = 1$ is equivalent to a nonlinear σ-model in one dimension in an external field for a d-component spin vector of unit length; the compressive force plays the role of an external magnetic field, which acts to reverse the magnetization. In this analogy the buckling instability corresponds to the onset of magnetization reversal upon reversal of the magnetic field, and the critical threshold force F_c for buckling is analogous to the coercive magnetic field. In the context of magnetic systems, it is well-known that there is no ordered phase in one-dimensional systems *in the thermodynamic limit* of infinite system size. Thus, for the buckling instability it is crucial that we consider a *finite* system. This is reflected in the result $F_{c,0} \sim \kappa/L^2$ for the critical buckling force at zero temperature, which vanishes in the thermodynamic limit of large contour lengths L.

In two spatial dimensions we can fulfill the constraint $|\mathbf{t}(s)| = 1$ explicitly by using a parameterization in terms of the tangent angle $\phi(s)$, i.e., $\mathbf{t}(s) = (\cos\phi(s), \sin\phi(s))$. The Hamiltonian becomes

$$\mathcal{H} = \int_0^L ds \left[\frac{\kappa}{2} (\partial_s \phi(s))^2 + F \cos\phi(s) \right] \tag{3.2}$$

where $F \equiv |\mathbf{F}|$ is the absolute value of the compressive force. We consider the buckling instability of the straight state $\phi(s) = 0$ and the compressive force is acting in the direction $\phi = \pi$. An important quantity, which can serve as order parameter for the buckling instability, is the projected length $L_\parallel$, which is given by

$$L_\parallel = \int_0^L ds \cos\phi(s). \tag{3.3}$$

Note that in the presence of thermal fluctuations the projected length $L_{||}$ is smaller than L already before the filament buckles (compare Chapter 2).

3.3 Perturbation theory for buckling in the presence of thermal fluctuations

In the first approach to the buckling of a fluctuating in two spatial dimensions filament we use the perturbation theory up to quadratic order in $\phi(s)$. We expand the tangent angle $\phi(s)$ in the Hamiltonian (3.2) to the second order around the buckling angle

$$\phi(s) \approx \phi_0(s) + \epsilon(s) \ , \tag{3.4}$$

where $\phi_0(s)$ is the buckling angle, see Chapter 2. Since the projected length $L_{||}$ at $T = 0$ reads $L_{||} = \int_0^L ds \cos\phi(s)$ we introduce the projected length in the presence of thermal fluctuations as the integral of the mean value of the cosine, i.e.,

$$\langle L_{||} \rangle = \int_0^L ds \langle \cos\phi(s) \rangle \ . \tag{3.5}$$

As we will see later, the mean projected length $\langle L_{||} \rangle$ is given by the partial derivative of the Gibbs free energy G [45] respect to the compressional force F, where $G(F)$ reads

$$G(F) = -T \ln Z \ , \tag{3.6}$$

where T is the temperature in k_B units and Z is the partition function of the system.

We consider the expansion around the unbuckled state, i.e., for $\phi_0(s) = 0$. Then, the Hamiltonian of the system reads

$$\mathcal{H} = \int_0^L ds \left\{ \frac{\kappa}{2} \left(\partial_s \epsilon(s)\right)^2 + F \cos\left(\epsilon(s)\right) \right\} . \tag{3.7}$$

For small buckling angles we can expand the cosine on the right hand side of (3.7) to the second order and get

$$\mathcal{H} = \int_0^L ds \left\{ \frac{\kappa}{2} \left(\partial_s \epsilon(s)\right)^2 + F \left(1 - \frac{1}{2}\epsilon^2(s)\right) \right\} . \tag{3.8}$$

We can rewrite the Hamiltonian of the system in the following way

$$\begin{aligned} \mathcal{H} &= \int_0^L ds \left\{ -\frac{\kappa}{2} \epsilon(s) \partial_s^2 \epsilon(s) + F \left(1 - \frac{1}{2}\epsilon^2(s)\right) \right\} \\ &= LF + \int_0^L ds \epsilon(s) \left[-\frac{\kappa}{2}\partial_s^2 - \frac{1}{2}F \right] \epsilon(s), \end{aligned} \tag{3.9}$$

where we integrated by parts using boundary conditions $\epsilon(s = 0) = \epsilon(s = L) = 0$ for both ends clamped. Since the operator on the right hand side of (3.9) is a Hermitian operator we have the following representation for $\epsilon(s)$

$$\epsilon(s) = \sum_\nu A_\nu \psi_\nu(s), \tag{3.10}$$

where $\psi_\nu(s)$ are the eigenfunctions of the operator $\left[-\frac{\kappa}{2}\partial_s^2 - \frac{1}{2}F\right]$ and with coefficients A_ν and we rewrite the Hamiltonian as follows

$$\mathcal{H} = FL + \sum_\nu \lambda_\nu A_\nu^2, \tag{3.11}$$

where λ_ν are the eigenvalues to eigenvectors ψ_ν. Now, we have to solve an eigenvalue problem for

$$\left[-\frac{\kappa}{2}\partial_s^2 - \frac{1}{2}F \right] \psi_\nu(s) = \lambda_\nu(F) \psi_\nu(s) \tag{3.12}$$

where $\lambda_\nu(F)$ depend on the force F. We propose Ansatz for eigenfunction $\psi_\nu(s)$ in form

$$\psi(s) = C_1 \sin(Ks) + C_2 \cos(Ks) \tag{3.13}$$

with constants C_1 and C_2 determined by the boundary conditions and

$$K^2 = \frac{2\lambda + F}{\kappa}. \tag{3.14}$$

We use the boundary conditions for a filament with both ends clamped, i.e., $\psi(0) = 0$ and $\psi(L) = 0$ and get the condition for the wave vector K,

$$K = \nu\pi/L \tag{3.15}$$

with $\nu = 1, 2, 3, ..., \infty$. The eigenvalues read

$$\lambda_\nu(F) = \frac{\kappa\pi^2\nu^2}{2L^2} - \frac{F}{2}. \tag{3.16}$$

Now, we can write the partition function using (3.11) and (3.16)

$$Z = \int \mathcal{D}A_\nu \exp\left\{\frac{1}{T}\left(-LF + \sum_\nu \left(\frac{F}{2} - \frac{\kappa\pi^2\nu^2}{2L^2}\right) A_\nu^2\right)\right\} \tag{3.17}$$

$$= \prod_\nu \int dA_\nu \exp\left\{\frac{1}{T}\left(-LF + \sum_\nu \left(\frac{F}{2} - \frac{\kappa\pi^2\nu^2}{2L^2}\right) A_\nu^2\right)\right\}, \tag{3.18}$$

where $\int \mathcal{D}A_\nu$ denotes a path integral over all possible A_ν. Using the Gauss integral formula [31]

$$\int dx \exp\left(-ax^2 + bx\right) = \left(\frac{\pi}{a}\right)^{1/2} \exp\left(\frac{b^2}{4a}\right) \tag{3.19}$$

we get

$$Z = \exp\left(-\frac{LF}{T}\right) \cdot \prod_\nu \left(\frac{\pi}{\xi_\nu}\right)^{1/2} \tag{3.20}$$

with

$$\xi_\nu \equiv \frac{\lambda_\nu}{T}. \tag{3.21}$$

Now, we can calculate the Gibbs free energy (3.6) and the mean projected length $\langle L_{||} \rangle$ using

$$\langle L_{||}(F) \rangle \equiv \frac{\partial G(F)}{\partial F}. \tag{3.22}$$

We get the expression for the mean projected length in the form

$$\langle L_{||}(F) \rangle = L - \frac{1}{4} \sum_\nu \left(\frac{\kappa\pi^2\nu^2}{2L^2T} - \frac{F}{2T}\right)^{-1}. \tag{3.23}$$

Note, that for $T = 0$ we get the projected length equal the contour length, i.e., $\langle L_{||}(F) \rangle = L$, since we expanded $\phi(s)$ around the unbuckled state, see (3.4). Now, we convert the sum in (3.23) into an integral over all modes $\nu \to \infty$ and get

$$\langle L_{||}(F) \rangle = L - \frac{1}{4} \int_1^\infty d\nu \left(\frac{\kappa\pi^2\nu^2}{2L^2T} - \frac{F}{2T}\right)^{-1}. \tag{3.24}$$

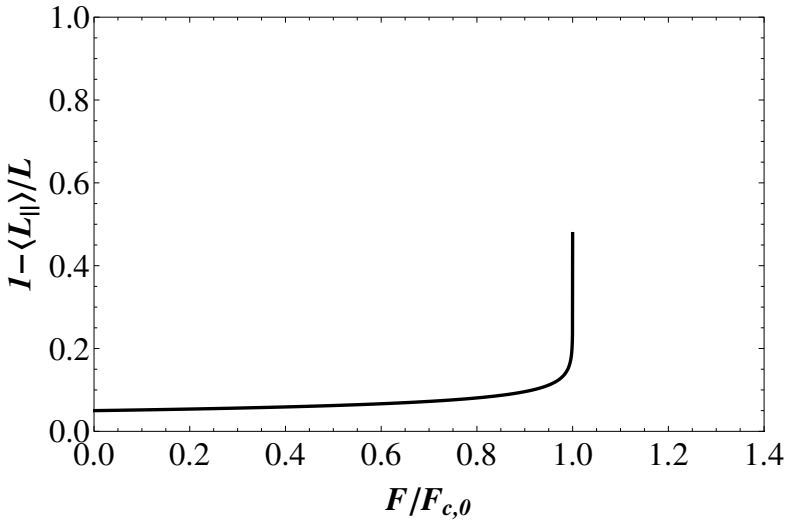

Figure 3.2: Force-extension relation (3.25) for a filament with the stiffness parameter $L_p/L = 1$. The logarithm in (3.25) diverges at $F/F_{c,0} = 1$ and one clamped and one free end. This shows that a simple expansion (3.4) of $\phi(s)$ around the buckling angle does not give any insight into the critical force of buckling in the presence of thermal fluctuations.

The solution of (3.24) leads to the formula for the reduced mean projected length $1 - \langle L_{||}\rangle/L$ as a function of compressional force F, i.e., force-extension relation, and reads

$$1 - \langle L_{||}\rangle/L = \frac{1}{4\pi^2}\frac{L}{L_p}\sqrt{\frac{F_{c,0}}{F}}\ln\left(\frac{1+\sqrt{F/F_{c,0}}}{1-\sqrt{F/F_{c,0}}}\right), \tag{3.25}$$

where $F_{c,0} = \kappa\pi^2/L^2$ is the critical force for filaments with both ends clamped, see Chapter 2. However, the logarithm on the right hand side of (3.25) diverges at the critical force $F = F_{c,0}$ and we can not observe any change of the critical force value caused by thermal fluctuations. The force-extension relation (3.25) is plotted in Fig. 3.2. The stiffness parameter of the filament was chosen to be $L_p/L = 1$.

In this section we showed that the perturbation theory for buckling up to the quadratic order in the tangent angle $\phi(s)$ around the buckling angle ϕ_0 does not give a good insight into the critical force of buckling in the presence of thermal fluctuations nor a complete solution for the force-extension relation. Integrating out the first mode $n = 1$ together with all higher modes causes the divergence in (3.25). Here, the zero mode $n = 0$ defines the spatial configuration of the filament.

Since the logarithm in (3.25) diverges at $F = F_{c,0}$ one has to consider a different model of filament buckling at $T > 0$. We present a proper model which goes beyond the perturbation theory in the next sections of this chapter. We will expand the tangent angle $\phi(s)$ in the Taylor series. After integrating out all higher modes (with short wavelengths) we will observe only the first $n = 1$ mode which will define the filament configuration.

3.4 Non-linear sigma model: Brief review

The non-linear sigma model is a widely used model in quantum field theory [46, 47]. In statistical physics it appears in the study of the large distance properties, in the ordered phase at low temperature, of lattice spin models with $O(N)$ symmetry and short-range interactions. From the statistical point of view the properties of this model derived from renormalization group (RG) considerations provide additional information about the large-distance behaviour of spin models, in the whole low-temperature ordered phase. In general the non-linear sigma model is a statistical field theory invariant under the group $O(N)$ acting on an N-component field (or classical spin) Φ with $\Phi^2 = 1$.

The non-linear sigma model provides a particular example (a classical spin model on a lattice with the nearest-neighbour ferromagnetic interactions) of a class of $O(N)$ symmetric lattice models: N-component classical spins with unit length interact through ferromagnetic,

short-range pair interactions. In zero external field, the partition function of such models takes the general form

$$Z = \int \prod_{i\in\mathbb{Z}^d} d\mathbf{S}_i \; \delta\left(\mathbf{S}_i^2 - 1\right) \exp\left[-\mathcal{H}_H(\mathbf{S})/T\right], \tag{3.26}$$

where $\mathbf{S}_i$ is an N-component vector, i denotes lattice sites, and the configuration energy is determined by the pair interaction V_{ij} and is given by the Heisenberg Hamiltonian [48]

$$\mathcal{H}_H(\mathbf{S}) = -\sum_{i,j\in\mathbb{Z}^d} V_{ij}\mathbf{S}_i \cdot \mathbf{S}_j. \tag{3.27}$$

The critical properties of such models can be inferred from RG analysis of a $(\Phi^2)^2$ effective field theory whose critical properties can be analyzed by RG methods near the upper-critical dimension (so called ϕ^4 field theory, see [46]).

In the case of buckling of an inextensible filament the Hamiltonian is given by the worm-like chain model (3.1),

$$\mathcal{H} = \int_0^L ds \left[\frac{\kappa}{2}\left(\partial_s \mathbf{t}(\mathbf{s})\right)^2 - \mathbf{F}\cdot\mathbf{t}(\mathbf{s})\right]. \tag{3.28}$$

In case when the tangent vector has only two components (two spatial dimensions, $d = 2$) we get the Hamiltonian (3.2),

$$\mathcal{H} = \int_0^L ds \left[\frac{\kappa}{2}(\partial_s\phi(s))^2 + F\cos\phi(s)\right]. \tag{3.29}$$

This model is often called the Sine-Gordon model. Now, for small values of the angle $\phi(s)$ one can expand the cosine in the second term on the right side of (3.29) and gets

$$\mathcal{H} = \int_0^L ds \left[\frac{\kappa}{2}(\partial_s\phi(s))^2 + F\cdot\left(1 - \frac{1}{2}\phi^2(s) + \frac{1}{4!}\phi^4(s) + \ldots\right)\right]. \tag{3.30}$$

This corresponds to the Ginzburg-Landau theory [21] and this approach will be used in this thesis.

3.5 Non-linear sigma model for buckling in the presence of thermal fluctuations

In order to consider the effects of thermal fluctuations on the buckling instability, several approaches are possible. We can expand around the 'classical' configuration obtained in the previous Chapter and integrate out fluctuations up to quadratic (or higher) order. This approach, however, does not allow to calculate a fluctuation-induced shift of the threshold force for buckling, see Section 3.3. Therefore, we employ a renormalization-like procedure where we integrate out short-wavelength fluctuations in order to obtain an effective theory governing the long-wavelength buckling instability. We focus on the regime close to the buckling instability where we can expand the Hamiltonian (3.2) in tangent angles up to quartic order, and obtain

$$\mathcal{H} = \int_0^L ds \left[\frac{\kappa}{2}(\partial_s\phi)^2 + F\left(1 - \frac{1}{2}\phi^2(s) + \frac{1}{24}\phi^4(s)\right)\right]. \tag{3.31}$$

For free and clamped boundary conditions, Fourier expansion of $\phi(s)$ leads to

$$\phi(s) = \sum_{n=1}^{N} \tilde{\phi}_n \cos(n\pi s/L) \quad \text{(free)} \tag{3.32}$$

$$\phi(s) = \sum_{n=1}^{N} \tilde{\phi}_n \sin(n\pi s/L) \quad \text{(clamped)}, \tag{3.33}$$

respectively, with Fourier coefficients $\tilde{\phi}_n$. The maximal wave number N is given by the number of degrees of freedom, $N = L/a$, where a is a microscopic cutoff, which is set by the monomer size or the filament diameter. For a microtubule $a \approx 25nm$ and for an F-actin filament $a \approx 7nm$. The $n = 0$ mode is absent for free boundary conditions because we apply the additional constraint $z(L) - z(0) = \int_0^L ds \sin\phi(s) = 0$ that the end points have the same height coordinate (perpendicular to the force direction). This constraint is automatically fulfilled by the zero temperature solution but has to be imposed separately in the presence of thermal fluctuations. The condition $\tilde{\phi}_0 = 0$ satisfies this constraint up to terms of order $\mathcal{O}(\tilde{\phi}_n^3)$.

In order to investigate the effect of the anharmonic quartic terms, we write the Hamiltonian (3.31) as

$$\mathcal{H} = \mathcal{H}_2 + \mathcal{H}_4, \tag{3.34}$$

where $\mathcal{H}_2$ contain all terms up to quadratic order and $\mathcal{H}_4$ the remaining terms up to quartic order. Using the Fourier expansions (3.32) or (3.33), the quadratic part can be rewritten as

$$\mathcal{H}_2\{\tilde{\phi}_n\} \;=\; FL + \sum_{n\geqslant 1} \frac{F_{c,0}L}{4}\left(n^2 - \bar{F}\right)\tilde{\phi}_n^2, \tag{3.35}$$

where

$$\bar{F} \equiv F/F_{c,0}. \tag{3.36}$$

This representation in Fourier modes shows that buckling is an instability of the $n = 1$ mode for $\bar{F} > 1$, which attains a non-zero equilibrium value in this regime at zero temperature. Higher modes $n > 1$ remain stable up to higher order buckling forces, i.e., for $\bar{F} < n^2$. In the following we focus on the regime $\bar{F} \ll 4$ where only the $n = 1$ mode can become unstable and large. Expectation values for higher modes $n, m \geqslant 2$,

$$\langle\tilde{\phi}_n\tilde{\phi}_m\rangle = \delta_{nm}\frac{2T}{F_{c,0}L}\frac{1}{n^2 - \bar{F}} \tag{3.37}$$

as calculated with the Hamiltonian (3.35) are of the order of

$$\frac{T}{F_{c,0}L} = \frac{1}{\pi^2}\frac{L}{L_p} \equiv \bar{T}. \tag{3.38}$$

The dimensionless parameter $\bar{T}$ is a reduced temperature, which is small for semiflexible filaments with $L \lesssim L_p$. Expectation values $\langle\tilde{\phi}_n^2\rangle \sim \bar{T}$ of higher modes are, thus, small as well. The parameter $\bar{T}$ will be used in the following as an expansion parameter for the systematic treatment of fluctuations. This parameter is small in the limit of small temperature, large bending rigidity, or small contour length. A typical value for a microtubule of contour length $L = 10\mu$m and $L_p = 1$mm is $\bar{T} \simeq 10^{-3}$, whereas an actin filament of contour length $L = 10\mu$m and $L_p = 15\mu$m has a much larger value $\bar{T} \simeq 6.7 \times 10^{-2}$.

This motivates our treatment of the quartic Hamiltonian $\mathcal{H}_4$. Because fluctuations of higher Fourier modes $n \geqslant 2$ will remain small at the buckling transition we neglect terms of cubic and quartic order in the Fourier modes $n \geqslant 2$. The corresponding terms for the unstable $n = 1$ mode have to be retained, and we obtain

$$\begin{aligned}\mathcal{H}_4\{\tilde{\phi}_n\}/T \;=\; & \frac{\bar{F}}{64\bar{T}}\,\tilde{\phi}_1^4 \pm \frac{\bar{F}}{48\bar{T}}\,\tilde{\phi}_1^3\tilde{\phi}_3 \\ & + \sum_{n\geqslant 2}\frac{\bar{F}}{16\bar{T}}\left(\tilde{\phi}_1^2\tilde{\phi}_n^2 \pm \tilde{\phi}_1^2\tilde{\phi}_n\tilde{\phi}_{n+2}\right).\end{aligned} \tag{3.39}$$

The upper and lower signs in (3.39) are for free and clamped boundary conditions, respectively.

We first trace over all higher order modes $n \geqslant 2$ in order to obtain an effective Hamiltonian for the single mode $n = 1$, which is the relevant mode for the buckling instability:

$$e^{-\mathcal{H}_{\rm eff}\{\tilde{\phi}_1\}/T} = \left(\prod_{n \geqslant 2} \int_{-\infty}^{\infty} d\tilde{\phi}_n \right) e^{-\mathcal{H}_2\{\tilde{\phi}_n\}/T - \mathcal{H}_4\{\tilde{\phi}_n\}/T}. \tag{3.40}$$

The Hamiltonian $\mathcal{H}_2 + \mathcal{H}_4$ as given by eqs. (3.35) and (3.39) is quadratic in the higher order modes and the Gaussian integrals in (3.40) can be performed to obtain

$$\mathcal{H}_{\rm eff}\{\tilde{\phi}_1\}/T \;=\; \bar{F}/\bar{T} + \alpha\tilde{\phi}_1^2 + \beta\tilde{\phi}_1^4 \tag{3.41}$$

with

$$\alpha \;\equiv\; \frac{1}{4}\left[\frac{1-\bar{F}}{\bar{T}} + \frac{1}{2}\mathrm{h}(\bar{F})\right], \tag{3.42}$$

$$\mathrm{h}(\bar{F}) \;\equiv\; \sum_{n \geqslant 2} \frac{\bar{F}}{n^2 - \bar{F}}\,, \tag{3.43}$$

$$\beta \;\equiv\; \frac{1}{64}\frac{\bar{F}}{\bar{T}} \tag{3.44}$$

to leading order in the small parameter $\bar{T}$. We point out that to this order there is no difference between clamped and free boundary conditions. Therefore, our results regarding the critical force and the mean projected length will be identical for both types of boundary conditions also in the presence of thermal fluctuations. The function $\mathrm{h}(\bar{F})$ can be approximated by $\mathrm{h}(\bar{F}) \simeq \sqrt{\bar{F}}\ \mathrm{arccoth}\left(2/\sqrt{\bar{F}}\right)$ by converting the sum into an integral. Close to the buckling threshold around $\bar{F} = 1$ we can also find an exact expression for the Taylor expansion $\mathrm{h}(\bar{F}) \approx 3/4 + (1 - \bar{F})(\pi^2/12 + 1/16)$. For $|\bar{T}| \ll 1$ we can therefore use

$$\alpha \approx \frac{1}{4}\left[\frac{3}{8} + \frac{1-\bar{F}}{\bar{T}}\right] \tag{3.45}$$

to a good approximation.

3.5.1 Critical force

The resulting effective theory (3.41) for the single mode $\tilde{\phi}_1$ is a fourth order Ginzburg-Landau-type theory. The buckling instability occurs if the coefficient $\alpha(\bar{F})$ of the quadratic term changes sign. This determines the critical force F_c in the presence of thermal fluctuations,

$$F_c = F_{c,0}\left[1 + \frac{\bar{T}}{2}\mathrm{h}(\bar{F}_c)\right] \approx F_{c,0}\left[1 + \frac{3\bar{T}}{8}\right], \tag{3.46}$$

where the last approximation is to leading order in the reduced temperature $\bar{T}$ such that $\mathrm{h}(\bar{F}_c) \approx \mathrm{h}(1) = 3/4$. The buckling event is the transition from parabolic potential (green curve on the Fig.3.3) to the double well potential (red curve on the Fig.3.3) with a bifurcation of the configuration of minimal energy. After buckling the system has two degenerated solutions. These two minima correspond to the buckling up or down events, i.e., in the direction of positive or negative x coordinate. In the ferromagnetic system this transition is a phase transition of the second kind (Landau-Ginzburg theory, [21]).

Using the relation $\bar{F} = \bar{L}^2$, we obtain the corresponding result for the critical contour length L_c in the presence of thermal fluctuations

$$\bar{L}_c = \sqrt{\bar{F}_c} \approx 1 + \frac{3\bar{T}}{16} \tag{3.47}$$

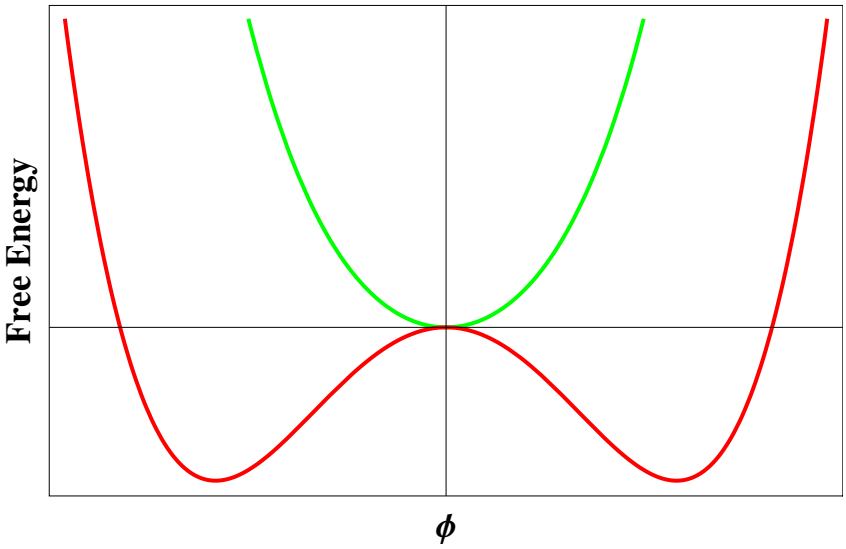

Figure 3.3: A schematic representation of the free energy as a function of the order parameter ϕ. The green parabolic curve corresponds to the unbuckled state of the filament ($\alpha(\bar{F}) > 0$). After the coefficient $\alpha(\bar{F})$ changes the sign the filament gets into the buckled conformation (red double-well potential). This transition is a bifurcation.

to leading order in $\bar{T}$.

It is remarkable that, in two dimensions as considered so far, the critical buckling force *increases* because of fluctuations effects as described by eq. (3.46). In the special case of two dimensions, the short-wavelength fluctuations always *weaken* the effect of the applied force on a larger scale because the fourth order contribution to the force term in the Hamiltonian (3.31) has a sign opposite to the leading quadratic contribution. We can define an effective compressive force $F_{\rm eff}(L)$ for the mode $n = 1$ of wavelength L by re-writing the coefficient α of the quadratic term of the effective theory (3.41) in an analogous form as the $n = 1$ term in the original Hamiltonian (3.35),

$$\alpha = \frac{1}{4\bar{T}}(1 - \bar{F}_{\rm eff}). \tag{3.48}$$

This effective compressive force is *smaller* than the original force,

$$\bar{F}_{\rm eff}(L) = \bar{F} - \frac{\bar{T}}{2}{\rm h}(\bar{F}) < \bar{F}, \tag{3.49}$$

as can be read off from (3.42). On the other hand, it is well known that short-wavelength fluctuations do *not* affect the bending rigidity on a larger scale in two dimensions because there is no bending rigidity renormalization in two dimensions for the continuous worm-like chain model (3.2) [7]. Thus, the effective buckling threshold $F_{\rm eff,c}(L)$ is not affected by short-wavelength fluctuations, and $F_{\rm eff,c}(L) = F_{c,0} = \pi^2\kappa/L^2$. The condition that the effective force needs to be sufficient to buckle the filament becomes $F_{\rm eff}(L) > F_{\rm eff,c}(L) = F_{c,0}$. Since the effective force is smaller than the "bare" force according to relation (3.49), this condition is equivalent to an increase of the "bare" critical buckling force: $F_c > F_{c,0}$. Because the bending rigidity is renormalized towards smaller values in dimensions $d > 2$ [7], this argument only applies to two spatial dimensions.

The argument can be generalized to arbitrary spatial dimensions by considering the behavior of the bending rigidity κ and the force F under the action of the renormalization group (RG) transformation, which has been worked out in the context of the equivalent nonlinear σ-model [49]. The continuous RG flow equations for the equivalent one-dimensional and d-component

nonlinear σ-model under an infinitesimal change of the length scale by a factor $b = 1 + d\ell$ are

$$\frac{d\kappa}{d\ell} = -\kappa + \frac{2-d}{2\pi\Lambda}T \tag{3.50}$$

$$\frac{dF}{d\ell} = F - \frac{d-1}{4\pi\Lambda}\frac{FT}{\kappa} , \tag{3.51}$$

where $\Lambda \sim 1/a$ is a large scale momentum cutoff. The buckling instability is governed by the dimensionless force $\bar{F} = F/F_{c,0} = FL^2/\pi^2\kappa$. Using the RG flow equations (3.50) and (3.51) (and the trivial flow under rescaling, $dL/d\ell = -L$), we find the RG equation for the dimensionless force,

$$\frac{d\bar{F}}{d\ell} = \frac{L^2}{\pi^2\kappa}\frac{dF}{d\ell} - \frac{FL^2}{\pi^2\kappa^2}\frac{d\kappa}{d\ell} + 2\frac{FL}{\pi^2\kappa}\frac{dL}{d\ell} \tag{3.52}$$

$$= \frac{d-3}{4\pi}\frac{1}{L_p\Lambda}\bar{F} , \tag{3.53}$$

i.e., $d\bar{F}/d\ell < 0$ for $d < 3$ and $d\bar{F}/d\ell > 0$ for $d > 3$. The effective dimensionless force for a mode of wavelength L is obtained by following the RG flow from the "bare" initial dimensionless force, $\bar{F}(0) = \bar{F}$, to the logarithmic scale $\ell = \ln(L/a)$, where $\bar{F}_{\rm eff}(L) = \bar{F}(\ln(L/a))$. The condition for buckling in the presence of thermal fluctuations is $\bar{F}_{\rm eff}(L) > 1$. If $d\bar{F}/d\ell < 0$ small fluctuations weaken the effective force as compared to the buckling threshold and an increased "bare" force is needed to achieve buckling, as in our above argument for two dimensions. The RG treatment thus shows that the critical force F_c in the presence of thermal fluctuations should be increased by thermal fluctuations for all dimensions $d < 3$, i.e., $F_c > F_{c,0}$, whereas it decreases for dimensions $d > 3$, i.e., $F_c < F_{c,0}$. The three dimensional case $d = 3$ is marginal, and higher order terms in the RG equations would need to be considered. For three spatial dimensions it has been argued by Odijk that the critical force decreases in the presence of thermal fluctuations [43] based on a calculation up to quadratic order.

The RG equation (3.52) shows that the behavior of the critical buckling force in the presence of thermal fluctuations is a result of two competing effects:

(i) The decrease of the effective compressive force by thermal fluctuations, which is present in all dimensions $d > 1$ according to the RG equation (3.51) and

(ii) the softening of the filament by thermal fluctuations, which decreases the renormalized bending rigidity in dimensions $d > 2$, as can be seen from the RG equation (3.50). The softening of the filament for $d > 2$ is related to the existence of out-of-plane fluctuations, which lead to additional anharmonic terms governing the fluctuations of azimuthal angles. The weakening of the effective force (i) gives rise to an increase in the critical buckling force and dominates for dimensions $d < 3$, whereas the softening of the filament (ii) leads to a decrease of the critical buckling force and dominates in dimensions $d > 3$.

3.5.2 Mean projected length

The partition sum Z is obtained by performing the one-dimensional integral over the remaining Fourier amplitude mode $\tilde{\phi}_1$,

$$Z = \int_{-\infty}^{\infty} d\tilde{\phi}_1 e^{-\mathcal{H}_{\rm eff}\{\tilde{\phi}_1\}/T}. \tag{3.54}$$

The partition sum defines the free energy $G \equiv -T \ln Z$. If the force dependence $G = G(F)$ is known the mean value of the projected filament length $L_\parallel$ from eq. (3.3) can be determined from the relation

$$\langle L_\parallel \rangle = \partial_F G(F) = -T\partial_F \ln Z(F). \tag{3.55}$$

The remaining integral over $\tilde{\phi}_1$ in (3.54) gives

$$\begin{aligned} Z &= e^{\bar{F}/\bar{T}} \int_{-\infty}^{\infty} d\tilde{\phi}_1 e^{-\alpha\tilde{\phi}_1^2 - \beta\tilde{\phi}_1^4} \\ &= \beta^{-1/4} \mathcal{P}(\alpha\beta^{-1/2}) \end{aligned} \tag{3.56}$$

with

$$\begin{aligned} \mathcal{P}(y) &\equiv \frac{1}{2}\sqrt{|y|} e^{y^2/8} \mathrm{K}_{1/4}(y^2/8) \quad \text{for } y > 0 \\ \mathcal{P}(y) &\equiv \frac{1}{2}\sqrt{|y|} e^{y^2/8} \frac{\pi}{\sqrt{2}} \left[\mathrm{I}_{1/4}(y^2/8) + \mathrm{I}_{-1/4}(y^2/8) \right] \quad \text{for } y < 0, \end{aligned} \tag{3.57}$$

where $\mathrm{I}_\nu(x)$ and $\mathrm{K}_\nu(x)$ denote modified Bessel function [31]. The parameters α and β are given by eqs. (3.42) and (3.44), respectively. The mean projected length is obtained by differentiating expression (3.56) with respect to the force according to (3.55). For the reduced mean projected length $\langle L_\parallel \rangle / L$ we finally obtain

$$1 - \frac{\langle L_\parallel \rangle}{L} = \bar{T} \left[-\frac{\partial_{\bar{F}}\beta}{4\beta} + \frac{\mathcal{P}'(\alpha/\beta^{1/2})}{\mathcal{P}(\alpha/\beta^{1/2})} \left(\frac{\partial_{\bar{F}}\alpha}{\beta^{1/2}} - \frac{\alpha \partial_{\bar{F}}\beta}{2\beta^{3/2}} \right) \right]. \tag{3.58}$$

We further evaluate this expression using the approximation (3.45) for α, which leads to the following dependence on the reduced force $\bar{F}$,

$$1 - \frac{\langle L_\parallel \rangle}{L} = -\frac{\bar{T}}{4\bar{F}} - \mathcal{P}_1 \left(\frac{\alpha}{\beta^{1/2}} \right) \frac{\bar{T}^{1/2}}{\bar{F}^{3/2}} \left(\bar{F}_c + \bar{F} \right) \tag{3.59}$$

with

$$\frac{\alpha}{\beta^{1/2}} \approx \frac{2}{\bar{T}^{1/2}\bar{F}^{1/2}} \left(\bar{F}_c - \bar{F} \right), \tag{3.60}$$

where

$$\begin{aligned} \mathcal{P}_1(y) &\equiv \frac{\mathcal{P}'(y)}{\mathcal{P}(y)} = \frac{y}{4} \left[1 - \frac{\mathrm{K}_{3/4}(y^2/8)}{\mathrm{K}_{1/4}(y^2/8)} \right] \quad \text{for } y > 0 \\ \mathcal{P}_1(y) &\equiv \frac{y}{4} \left[1 + \frac{\mathrm{I}_{3/4}(y^2/8) + \mathrm{I}_{-3/4}(y^2/8)}{\mathrm{I}_{1/4}(y^2/8) + \mathrm{I}_{-1/4}(y^2/8)} \right] \quad \text{for } y < 0 \end{aligned} \tag{3.61}$$

is a monotonously increasing, negative function. The solid curves in Fig. 3.4 show the result (3.59) for $1 - \langle L_\parallel \rangle / L$ as a function of the reduced force $\bar{F}$ for different values of the parameter $\bar{T}$.

For $\bar{F} < \bar{F}_c$ and $\bar{T} \ll (\bar{F}_c - \bar{F})^2$, we use the asymptotic behavior $\mathcal{P}_1(y) \approx -1/2y$ for $y \gg 1$ and find

$$1 - \frac{\langle L_\parallel \rangle}{L} \approx \frac{\bar{T}}{2(\bar{F}_c - \bar{F})}, \tag{3.62}$$

which is reminiscent of the shortening of a free filament by thermal fluctuations $1 - \langle L_\parallel \rangle / L \approx \langle \phi^2 \rangle / 2 \sim \bar{T}$. For $\bar{F} > \bar{F}_c$ and $\bar{T} \ll (\bar{F}_c - \bar{F})^2$ we use $\mathcal{P}_1(-y) \approx -y/2 + 5y/16$ for $y \gg 1$ and obtain the asymptotics

$$1 - \frac{\langle L_\parallel \rangle}{L} \approx 1 - \left(\frac{\bar{F}_c}{\bar{F}} \right)^2 - \frac{\bar{T}}{4\bar{F}} \left(1 + \frac{5}{8} \frac{\bar{F}_c + \bar{F}}{\bar{F} - \bar{F}_c} \right), \tag{3.63}$$

which describes the suppression of thermal fluctuations and the approach to the zero temperature solution $1 - L_\parallel / L = 1 - \bar{F}^{-2}$ in the strongly buckled state. Note that this zero temperature solution differs from the results presented in Chapter 2, which are also shown in Fig. 3.4 as solid

black line, because of the expansion of the full Hamiltonian (3.2) up to fourth order in (3.31). The asymptotics (3.62) and (3.63) show that thermal fluctuations as described by the small parameter $\bar{T}$ *decrease* the mean projected length $\langle L_\parallel \rangle$ below its zero temperature value $L_\parallel = L$ for $\bar{F} < \bar{F}_c$ whereas they *increase* the mean projected length above the zero temperature value $L_\parallel = L\bar{F}^{-2}$ in the buckled state for $\bar{F} > \bar{F}_c$.

We thus conclude that thermal fluctuations lead to a stretching of buckled filaments, whereas they compress unbuckled ones. This implies that two curves for the mean projected length $\langle L_\parallel \rangle$ as a function of force, which are taken at different temperatures $\bar{T}$, should *intersect* in the vicinity of the buckling force. This characteristic behavior is clearly confirmed in Figs. 3.4, where the full analytical result (3.59) is shown at different temperatures. The force value F_i of the intersection point of a projected length curve taken in the presence of thermal fluctuations with the zero temperature curve can be obtain approximately by expanding both curves around $\bar{F} = 1$. Using the expansion $\mathcal{P}_1(y) \approx a_0 + a_1 y$ for $y \ll 1$ with $a_0 = -\Gamma(3/4)/\Gamma(1/4) \simeq -0.34$ and $a_1 = 1/4 - a_0^2 \simeq 0.14$, where $\Gamma(x)$ is the Gamma function [31], in eq. (3.59) we find

$$1 - \frac{\langle L_\parallel \rangle}{L} \approx 2a_0 \bar{T}^{1/2} + 4a_1(\bar{F} - 1) \tag{3.64}$$

in the presence of thermal fluctuations and $1 - L_\parallel/L \approx 2(\bar{F} - 1)$ at zero temperature. Equating both results we obtain the intersection force

$$\bar{F}_i \approx 1 + \frac{2a_0}{1 + 4a_0^2} \bar{T}^{1/2}. \tag{3.65}$$

The intersection force F_i exceeds $F_{c,0}$ by a force $\sim \bar{T}^{1/2} F_{c,0}$ and, thus, also exceeds F_c for small $\bar{T}$, see (3.46). The increase of the force value for the intersection of the solid curves with the dashed black zero temperature curve with increasing $\bar{T}$ can also be clearly recognized in Fig. 3.4.

A characteristic feature of the buckling instability at zero temperature is the cusp in the relation between projected and contour length at the critical contour length $L_{c,0}$, see the solid black curve in Fig. 3.5 (compare Chapter 2). For $L < L_{c,0}$ in the unbuckled state, the projected length is given by $L_\parallel = L$ and grows with the contour length. The projected length becomes maximal at the critical length $L = L_{c,0}$, where the filament buckles. If the filament grows further after buckling, $L > L_{c,0}$, the projected length decreases and $L_\parallel < L_{c,0}$. In the presence of thermal fluctuations, the cusp becomes modified, and we obtain the reduced mean projected length $1 - \langle L_\parallel \rangle / L_{c,0}$ as a function of the reduced contour length $\bar{L} \equiv L/L_{c,0}$ by applying the relations $\bar{F} = \bar{L}^2$ and

$$1 - \frac{\langle L_\parallel \rangle}{L_{c,0}} \;=\; \left(1 - \frac{\langle L_\parallel \rangle}{L}\right) \bar{L} + (1 - \bar{L}) \tag{3.66}$$

to our previous result (3.59). This gives

$$1 - \frac{\langle L_\parallel \rangle}{L_{c,0}} = 1 - \bar{L} - \frac{\bar{T}}{4\bar{L}} - \mathcal{P}_1\left(\frac{\alpha}{\beta^{1/2}}\right) \frac{\bar{T}^{1/2}}{\bar{L}^2} \left[\bar{L}_c^2 + \bar{L}^2\right] \tag{3.67}$$

with

$$\frac{\alpha}{\beta^{1/2}} \approx \frac{2}{\bar{T}^{1/2}\bar{L}} \left[\bar{L}_c^2 - \bar{L}^2\right]. \tag{3.68}$$

The solid curves in Fig. 3.5 represent the expression $1 - \langle L_\parallel \rangle / L_{c,0}$ as a function of $\bar{L}$ according to eq. (3.67). Thermal fluctuations lead to a rounding of the zero temperature cusp to a pronounced minimum and to a shift of the location $\bar{L}_m$ of this minimum. Because thermal fluctuations lead to a stretching of buckled filaments, whereas they compress unbuckled filaments, curves for different temperatures $\bar{T}$ *intersect* in Fig. 3.5. In principle, the contour length $\bar{L}_m$, where the mean projected length $\langle L_\parallel \rangle$ is maximal, could be determined experimentally by observing filaments growing against an obstacle as in Ref. [36]. A prediction for the value of $\bar{L}_m$ can be

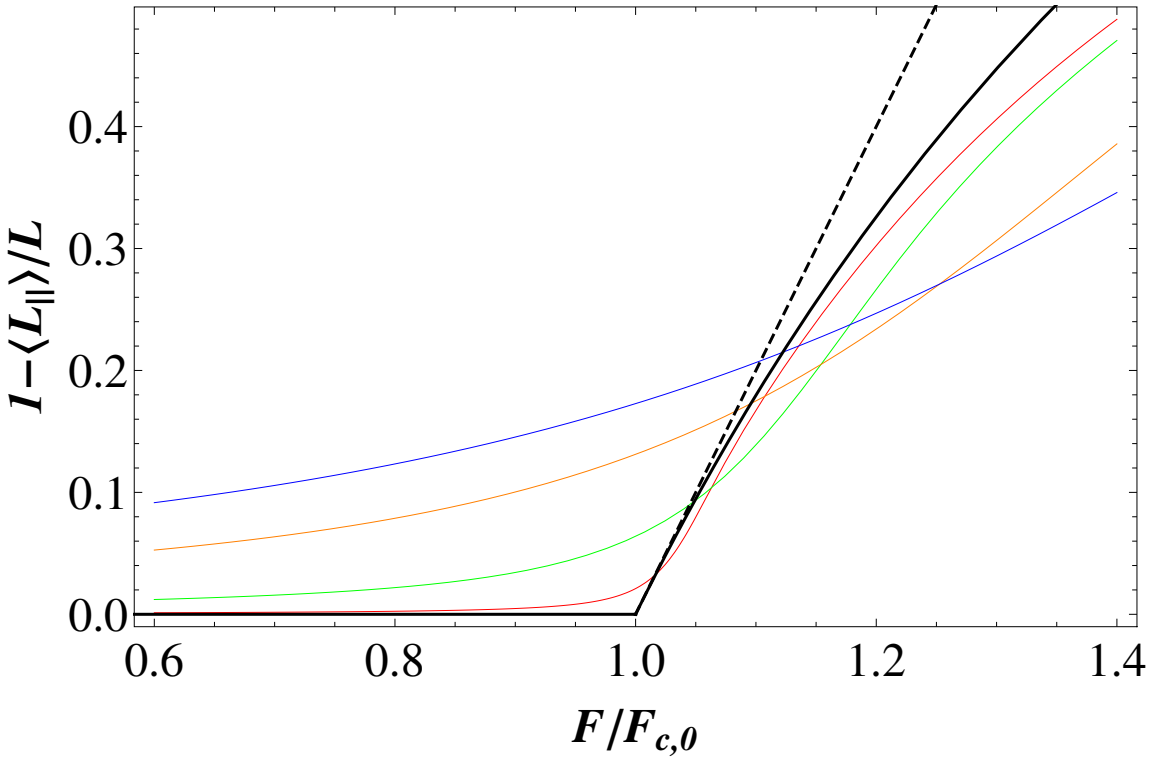

Figure 3.4: Reduced projected length $\langle L_\parallel \rangle / L$ as a function of the reduced force $F/F_{c,0}$ for $L_p/L = 100$ (red), 10 (green,), 2 (orange), and 1 (blue) corresponding to $\bar{T} \simeq 10^{-3}, 10^{-2}, 5 \times 10^{-2}$, and 10^{-1}. The solid curves show the analytic result (3.59). The black line corresponds to the zero temperature solution shown in Fig. 2.3 and the dashed line corresponds to the linear approximation (2.23).

calculated from the result (3.67) by considering the limit $\alpha\beta^{-1/2} \ll 1$ and extending the Taylor expansion $\mathcal{P}_1(y) \approx a_0 + a_1 y + a_2 y^2/2$ for $y \ll 1$ to quadratic order with $a_2 = -|a_0|^3 \simeq -0.08$, which finally gives

$$\bar{L}_m \approx \bar{L}_c \left(1 + \bar{T}^{1/2} \frac{8a_1 - 1 + 2a_0 \bar{T}^{1/2}}{32a_2 + 24a_1 \bar{T}^{1/2}} \right), \tag{3.69}$$

i.e., the contour length $\bar{L}_m$, where the mean projected length $\langle L_\parallel \rangle$ becomes maximal, is shifted by a length $\sim \bar{T}^{1/2}$ from the actual critical length L_c as given by eq. (3.47) and the zero temperature critical length $L_{c,0}$. For small values $\bar{T} \ll 1$, L_m is a non-monotonic function of $\bar{T}$ and first decreases to values $L_m < L_{c,0} < L_c$ before it becomes an increasing function of $\bar{T}$ and grows beyond L_c.

3.6 Conclusions

We presented a systematic study of the buckling instability in the presence of thermal fluctuations in two spatial dimensions. By integrating over all short-wavelength modes we derived an effective theory, see (3.41), which governs the buckling instability of the Fourier mode with the longest wavelength given by the filament length. We find that thermal fluctuations *increase* the critical force for buckling in two spatial dimensions. The increase in the critical buckling force is closely related to our main result that curves for the mean projected length $\langle L_\parallel \rangle$ measuring the end-to-end extension of the filament as a function of the applied compressive force, which are taken at different temperatures, *intersect* in the vicinity of the buckling force. This leads to the conclusion that thermal fluctuations lead to a stretching of buckled filaments, whereas they compress unbuckled filaments.

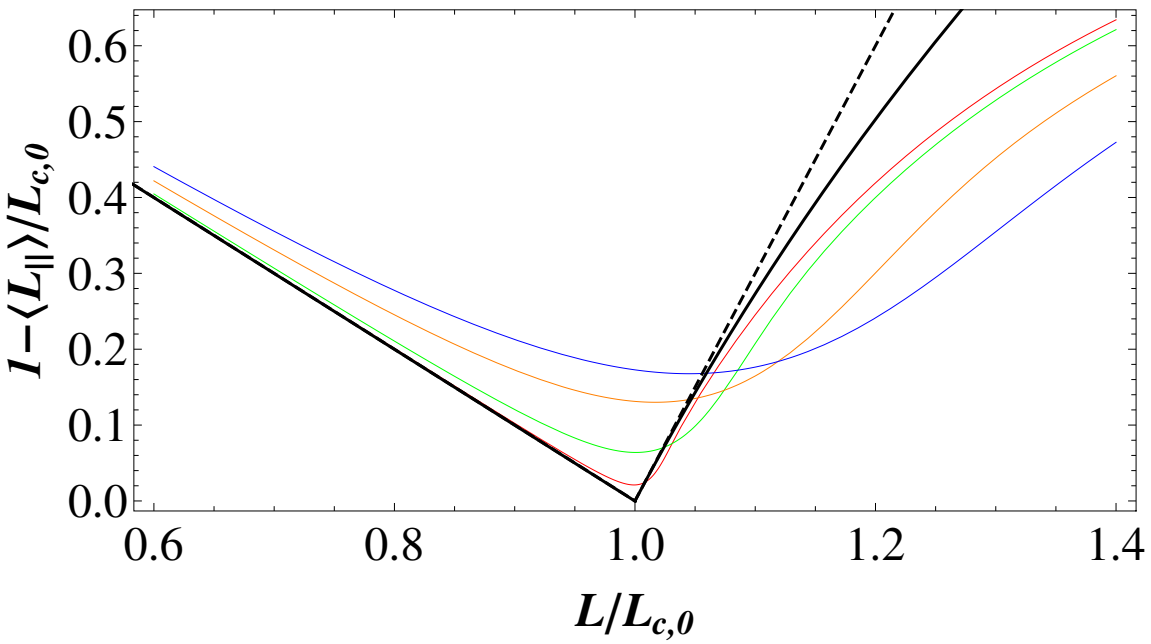

Figure 3.5: Reduced projected length $\langle L_\parallel\rangle/L_{c,0}$ as a function of the reduced contour length $L/L_{c,0}$ for $L_p/L = 100$ (red), 10 (green), 2 (orange), and 1 (blue) corresponding to $\bar{T} \simeq 10^{-3}, 10^{-2}, 5\times10^{-2}$, and 10^{-1}. The solid curves show the analytic result. The analytical zero temperature solution from Fig. 2.4 is shown as black line and its linear approximation (2.25) as black dashed line. The analytical zero temperature solution $1 - L_\parallel/L = 1 - \bar{L}^{-4}$ is included as a black line.

We presented arguments based on renormalization results for the nonlinear σ-model which suggest that an increase in the critical force is found for all spatial dimensions $d < 3$, whereas the critical force should decrease for dimensions $d > 3$. The exact behavior in the marginal three-dimensional case remains an open question for future studies. It also remains an open question whether the effect of stretching by thermal fluctuations persists for spatial dimensions $d > 2$.

Our main result is the observation that a buckled filament stretches, i.e., increases its mean projected length in the direction of the applied force, upon increasing the temperature. This effect might have interesting consequences for a crosslinked network of filaments, which is under uniaxial compression such that a large fraction of filaments is buckled. The stretching of filaments by thermal fluctuations on the single filament level should lead to a *swelling* of the crosslinked filament network by thermal fluctuations. This is qualitatively different from the typical behavior of a network of flexible polymers, i.e., a rubber-like material, which stiffens and shrinks upon increasing the temperature [50]. The main reason for this qualitative difference lies in the role of entropy. Before buckling a filament is governed by entropy and an increasing temperature leads to a shortening of the filament in order to maximize its configurational entropy, similar to the well-known elastic behavior of a flexible polymer, which gives rise to classical rubber elasticity [50]. A buckled filament, on the other hand, is governed by its bending energy and for increasing temperature also the bending energy decreases in favor of the entropy, which gives rise to the observed effect of stretching by thermal fluctuations.

3.7 Summary

In this chapter we presented an analytical model of buckling of filaments in two spatial dimensions in the presence of thermal fluctuations.

In Section 3.3 we showed that the perturbation theory for buckling with a simple expansion up to quadratic order of the tangent angle $\phi(s)$ does not give a complete solution for the force-extension relation. Since the integral in (3.24) diverges at $F = F_{c,0}$ this approach does not give

any insight into the change of the critical force caused by the thermal fluctuations. In this case one has to consider a different model of filament buckling at $T > 0$.

Using the non-linear sigma model, we proved in Section 3.5 that, in the buckled state, thermal fluctuations lead to an *increase* in the mean projected length of the filament in the force direction. As a function of the contour length, the mean projected length exhibits a cusp at the buckling instability, which becomes rounded by thermal fluctuations.

In the following chapter we will investigate the buckling instabilities of fluctuating filaments in two spatial dimensions using Monte Carlo simulations. The simulation results will confirm the analytical solution presented here. The case of $d > 2$ dimensions will be considered as well. We will present the simulation results for two different boundary conditions.

Chapter 4

Monte Carlo simulations of buckling instabilities in the presence of thermal fluctuations

In the previous Chapter, we presented a model of buckling instabilities of rods in two dimensional space in the presence of thermal fluctuations. Using the non-linear sigma model, we calculated a shifted critical force F_c which turned out to be larger than in the absence of fluctuations. We calculated the force-extension relation for buckling of fluctuating filaments as well as the reduced projected length as a function of contour length of the filament. Now, we will confirm our analytical results by numerical simulations. For this purpose we perform Monte Carlo simulations investigating a discrete worm-like chain model representing the fluctuating filament in two spatial dimensions. The results are compared with the analytically predicted relations for different stiffness parameters L_p/L. We investigate also filaments in three and four spatial dimensions by extending the simulation code to these cases.

4.1 Monte Carlo method

The analytical results presented in Chapter 3 are checked using the Monte Carlo (MC) simulation method. The goal of Monte Carlo simulation is to find the mean values of observables. In order to do so one has to sample many configurations according to their Boltzmann weight. The configurations can be created in two different ways: the *statical* and the *dynamical* way [51]. In a static MC simulation a new configuration which a polymer can take in the phase space is being created in each step of the simulation. The Boltzmann weight is calculated for each configuration. In a *dynamic* MC simulation the simulation starts with a given (randomly created or specially chosen) initial configuration and is randomly changed during the simulation. In this way new configurations are created in every step of simulation. This stochastic process corresponds to a Markov chain [52, 53, 54]. The changes of configurations are accepted or rejected to ensure convergence to a Boltzmann distribution. During the simulation the measurements of observables are taken at equal time intervals and their mean values are calculated. In this work we will use dynamic MC simulations using the Metropolis algorithm.

4.1.1 The Metropolis Algorithm

In our simulation we use the Metropolis algorithm [55] which is based on a Markovian process and fullfils the requirements for detailed balance and ergodicity. An important condition that our simulation should satisfy is detailed balance. In statistical physics this condition ensures that the Boltzmann distribution is reached in equilibrium. The definition for equilibrium is that

the total transition probabilities into and out of a given state i have to be equal, that is

$$\sum_j W(j \to i) w_j = \sum_i W(i \to j) w_i, \tag{4.1}$$

where $w_i(t)$ is the probability of being in state i at time t and $W(i \to j)$ is the transition probability from state i to state j per unit time. Eq. (4.1) is a necessary condition for equilibrium. A sufficient condition for equilibrium is the detailed balance condition

$$w_j W(j \to i) = w_i W(i \to j), \tag{4.2}$$

for all i, j which gives rise to equilibrium between each pair of states i and j.

A possible way to realize detailed balance in a MC simulation is the use of the Metropolis algorithm, which is presented below. First, one establishes the initial energy of the system E_{init}.

Now we offer the system a transition into a new configuration, which usually represents a randomly chosen local change of the initial configuration (e.g. moving a small polymer segment or flipping an individual spin in the Ising model simulation). These changes proposed to the system are called Monte Carlo moves. This new state has energy E_{new}. The next step is the computation of the energy change $\Delta E = E_{new} - E_{init}$. If $\Delta E \leqslant 0$ the new configuration is accepted. Otherwise, if $\Delta E > 0$, we compute $w = \mathrm{e}^{-(\Delta E/T)}$. Now, we compare w with a random number r from a uniform distribution on $[0, 1]$. If $r \leqslant w$ the change is accepted, otherwise the old configuration is kept. In order to sample enough microstates one repeats the above steps. Mean values of observables can be computed by performing a sufficient number of MC steps between measurements to ensure a statistically independent configuration. This algorithm satisfies the conditions of detailed balance and ergodicity, i.e., the whole phase space is sampled (note, that the ergodicity depends on what kind of MC moves one offers) [56, 57].

4.2 Monte Carlo procedure

An inextensible semifexible polymer or filament of contour length L in d spatial dimensions is governed by the general worm-like chain Hamiltonian (see Chapter 1)

$$\mathcal{H} = \int_0^L ds \left[\frac{\kappa}{2} (\partial_s \mathbf{t})^2 - \mathbf{F} \cdot \mathbf{t}(s) \right], \tag{4.3}$$

where s is the arc length and $\mathbf{t}(s)$ are d-dimensional unit tangent vectors along the contour with $|\mathbf{t}(s)| = 1$. The homogeneous external force $\mathbf{F}$ will be taken to be compressive in the following. The Hamiltonian (4.3) only contains contributions from the bending energy and the external force and applies to inextensible filaments without torsional degrees of freedom.

In our MC simulations we study fluctuating filaments in two, three and four spatial dimensions under a compressional force $\mathbf{F}$. We use two different boundary conditions. First we consider filaments with both ends clamped which means that the tangent vector $\mathbf{t}(s)$ is fixed at $s = 0$ and $s = L$. In the case of a filament in two dimensions this corresponds to

$$\phi(s = 0) = \phi(s = L) = 0. \tag{4.4}$$

In the second case one end is clamped ($\phi(s = 0) = 0$) and the other end is free. A free end means that the tangent vector $\mathbf{t}(s)$ can freely rotate at $s = L$ which corresponds to the condition

$$\partial_s \phi(s = L) = 0 \tag{4.5}$$

for two dimensions. For free boundary conditions (both ends free), the simulation is complicated by the fact that the filament "flips around" and reaches its trivial absolute minimum at $\phi(s) = \pi$ (for the Hamiltonian (3.2)) by thermal activation out of the metastable buckled state. In this

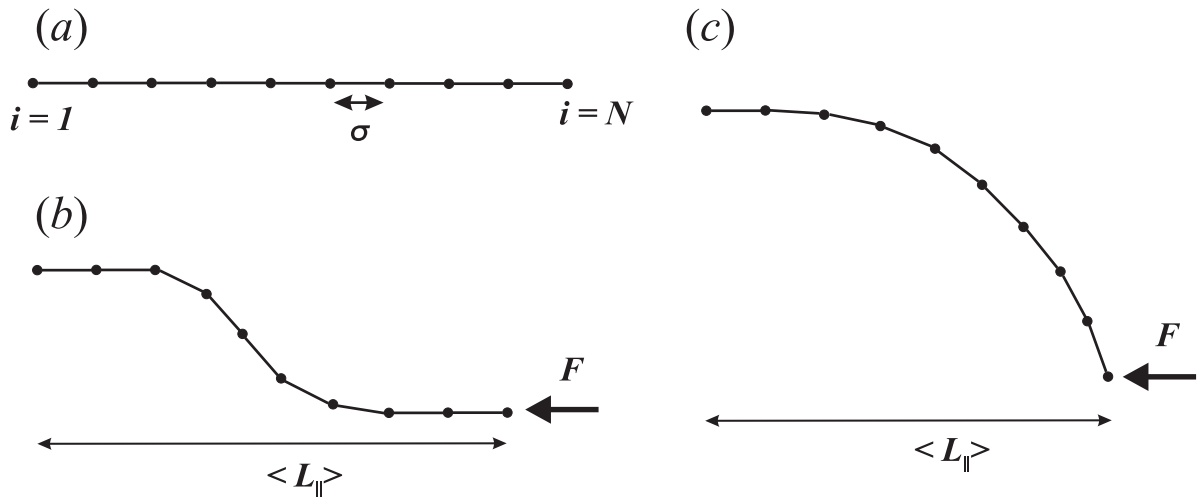

Figure 4.1: Discrete worm-like chain model used for Monte Carlo simulations. The index i denotes the bead number, σ the bond length, $\langle L_{\|}\rangle$ the mean projected length and $\mathbf{F}$ the compressional force. The cartoons show a straight filament (a) and a buckled filament with (b) both ends clamped and (c) with one end free and one end clamped.

case one has to introduce the constraints that the height (x position) of the ends is fixed. This case is not considered in further parts of this chapter.

Simulations of the system in two, three and four dimensional space are performed in tangent vector representation. For the case of two dimensions we also run simulations in tangent angle representation. For the purpose of simulations we rewrite the WLC Hamiltonian (4.3) as a discrete WLC

$$\mathcal{H}_{dWLC}\{\mathbf{t}_i\} = \sum_{i=2}^{N-1} \frac{\kappa}{\sigma}\,(1 - \mathbf{t}_i \cdot \mathbf{t}_{i-1}) - \sum_{i=2}^{N} \sigma \mathbf{F} \cdot \mathbf{t}_i \ , \tag{4.6}$$

where N is the number of beads and σ is the bond length and $\mathbf{t}_i$ denotes the tangent vector on the i-th bead. The bond length is the minimal length on which a change of the shape can occur and corresponds to the monomer size or the diameter of the filament. The discrete WLC Hamiltonian depends on the three parameters L/L_p, N, and LF/T.

The simulations are performed for four values of the stiffness parameter $L_p/L = 100$, 10, 2 and 1 corresponding to $\bar{T} \simeq 10^{-3}$, 10^{-2}, 5×10^{-2} and 10^{-1}, respectively, where $\bar{T} \equiv L/(L_p\pi^2) = T/(F_{c,0}L)$, see Chapter 3. Three cases of $N = 50$, $N = 100$ and $N = 200$ are studied in order to check the dependence of the results on the discretization. Since the value $N = 100$ ensures a good compromise between simulation precision and duration, mainly this case will be considered.

The following procedure is used for simulation of buckling of semiflexible polymer in $d = 2, 3, 4$ spatial dimensions. The system is described by the Hamiltonian (4.6). At first, we investigate a filament with both ends clamped and the compressional force $\mathbf{F}$ is taken to be parallel to the z-axis. The polymer is represented as a WLC (4.6) with $N = 50$, N=100 or N=200 beads. First, an array of tangent vector components is created giving the initial, straight configuration of the polymer. Next, one bead is randomly chosen. The x,y,z components of the tangent vector are changed randomly. The energy change on the chosen bead is calculated and the Metropolis algorithm is used for acceptance of the simulation step. For two clamped ends the tangent vectors on the first and the last bead are not changed. We perform $300{\cdot}10^6$ MC sweeps of the whole chain. Then the force is increased and the whole procedure is repeated. The step size of Monte Carlo moves is chosen in such a way that the acceptance of the procedure is ensured to be $\approx 50\%$, i.e., each MC move is accepted in probability ≈ 0.5. For each force step $F/F_{c,0}$ the projected length $\langle L_{||}\rangle$ is sampled 3000 times for the calculation of the final mean value for the projected length $\langle L_{||}\rangle$.

In case of a filament with one clamped and one free end the tangent vector $\mathbf{t}_i$ at the free end can freely rotate. A possible configuration of buckled filament with one free end is schematically shown in Fig. 4.1 (c).

The goal of our simulations is to determine the force-extension relation, i.e., the mean projected length $1 - \langle L_{||} \rangle / L$ in the force direction as a function of the reduced force $\bar{F} \equiv F/F_{c,0}$ and the reduced projected length $1 - \langle L_{||} \rangle / L_{c,0}$ as a function of the reduced length $\bar{L} \equiv L/L_{c,0}$ in the presence of thermal fluctuations. Since there is no torsion the buckling occurs always in one plane. The parameter $F_{c,0}$ defines the critical buckling force for a filament at $T = 0$ with

$$F_{c,0} \equiv \pi^2 \frac{\kappa}{L^2} \quad \text{(both ends clamped)}, \tag{4.7}$$

$$F_{c,0} \equiv \frac{\pi^2}{4} \frac{\kappa}{L^2} \quad \text{(one free end)}, \tag{4.8}$$

see Chapter 2. The parameter $L_{c,0}$ defines the critical buckling length (at fixed force) for a filament at $T = 0$ with

$$L_{c,0} \equiv \pi \sqrt{\frac{\kappa}{F}} \quad \text{(both ends clamped)}, \tag{4.9}$$

$$L_{c,0} \equiv \frac{\pi}{2} \sqrt{\frac{\kappa}{F}} \quad \text{(one free end)}, \tag{4.10}$$

see Chapter 2. At $T = 0$ the critical length $L_{c,0}$ is related to critical force $F_{c,0}$ by relation

$$L/L_{c,0} = \sqrt{F/F_{c,0}}. \tag{4.11}$$

4.3 Buckling in two spatial dimensions

First we consider a filament in two spatial dimensions. In this case the tangent vector $\mathbf{t}(s)$ has only two components and the filament fluctuates only in the plane in which it buckles. The projected length $\langle L_{||} \rangle$ is the end-to-end distance projected on the z-axis along which the compressional force F is acting. We investigate four cases of stiffness parameter values, i.e., $L_p/L = 100$ (red, $\circ$), 10 (green, $\triangle$), 2 (orange, $\triangledown$), and 1 (blue, $\square$) corresponding to $\bar{T} \simeq 10^{-3}, 10^{-2}, 5\times10^{-2}$, and 10^{-1}. Simulations of filaments with both ends clamped can be compared to the analytical solution (3.59) from Chapter 3. In Fig. 4.2 we present a sample configuration of a filament with $N = 100$ beads in $d = 2$ spatial dimensions before (a) and after buckling (b).

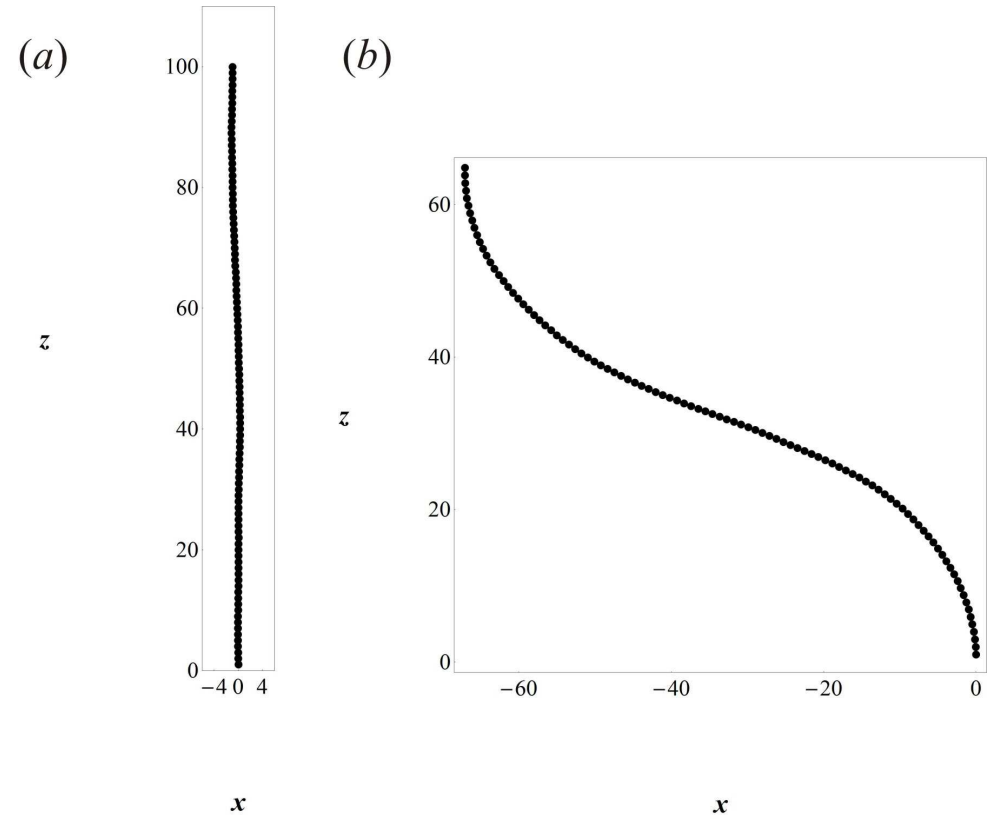

Figure 4.2: Snapshots of filament configurations in $d = 2$ spatial dimensions for $L_p/L = 100$ corresponding to $\bar{T} \simeq 10^{-3}$ with both ends clamped. Monte Carlo simulation data for (a) unbuckled configuration and (b) the buckled configuration. The compressional force acts along the z axis. The unbuckled filament has the length $L = \sigma \cdot N$ what corresponds to $z = 100$.

4.3.1 Projected length as a function of applied force

In this section we present the force-extension relation for buckling of thermally fluctuating filaments. The simulation results for the reduced projected length $\langle L_{\|} \rangle / L$ as a function of the reduced force $\bar{F} \equiv F/F_{c,0}$ in Fig. 4.3 are in good agreement with our analytical result (3.59). Here, both ends of filament are clamped. Deviations become appreciable only for the largest values of the reduced temperature $\bar{T} \simeq 10^{-1}$, i.e., the smallest values of the stiffness parameter L_p/L, for which we performed simulations. For these values it becomes necessary to include higher order terms in the expansion in $\bar{T}$ underlying the analytical result (3.59). The buckled filament increases its mean projected length in the direction of applied force, upon increasing the temperature. The *intersection* of force-extension curves for different stiffness parameters L_p/L (different temperatures $\bar{T}$) is clearly confirmed.

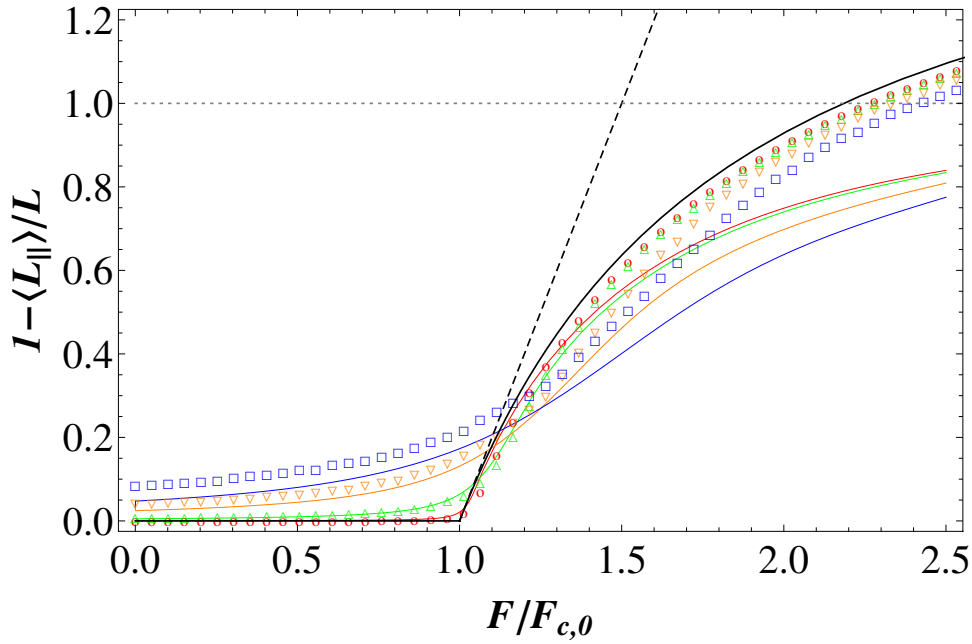

Figure 4.3: Monte Carlo simulation results for buckling of a filament in two spatial dimensions with both ends clamped. Reduced projected length $\langle L_{\parallel}\rangle/L$ as a function of the reduced force $F/F_{c,0}$ for $L_p/L = 100$ (red, ∘), 10 (green, △), 2 (orange, ▽), and 1 (blue, □) corresponding to $\bar{T} \simeq 10^{-3}, 10^{-2}, 5\times10^{-2}$, and 10^{-1}. The solid curves show the analytic result (3.59) for filaments with both ends clamped. The black line corresponds to the zero temperature solution in Fig. 2.3 and the dashed line corresponds to the linear approximation (2.23). The dotted line corresponds to a loop configuration when $\langle L_{\parallel}\rangle = 0$.

Since for each value of force 3000 data points are taken to calculate the mean value $\langle L_{\parallel}\rangle$ we can calculate the standard deviation for each data point which is shown as error bars in Fig. 4.4, [58]. Since the standard deviations are not changing significantly for different boundary conditions we neglect the error bars on other plots in this thesis.

In Fig. 4.5 we present the force-extension relation for a filament with one end clamped and one end free. Also in this case one can observe the stretching effect and a clear *intersection* of force-extension curves for different values of parameter L_p/L. Note, for a filament with one free end all projected lengths are smaller than for a filament with two clamped ends at the same values of L_p/L.

As we showed in Section 2.4 a filament of contour length L with one free end behaves at $T = 0$ like a filament with both ends clamped but with contour length $2L$. One can expect a similar relation in the presence of thermal fluctuations.

In the presence of thermal fluctuations, however, the fluctuation modes do not fulfill this symmetry relation exactly. Fluctuation modes with even n of a filament with two clamped ends and contour length $2L$ do not satisfy the correct boundary conditions if they are restricted to a filament with contour length L and one free and one clamped end. This leads to slightly different behavior of the function $h(\bar{T})$, see (3.43). Therefore, one expects, that a filament with one clamped and one free end and $L_p/L = 2$ behaves similar to a filament with both ends clamped and $L_p/L = 1$. In particular, this means that a filament with one free and one clamped end behaves similar to a filament with both ends clamped at a reduced temperature temperature $\bar{T}$ (3.38), which is twice as large. Therefore, a filament with one free and one clamped end shows much more pronounced effects from thermal fluctuations, as it can also be seen in the corresponding simulation results in Figs. 4.3 and 4.5. Note, that this is only an approximation and the complete calculation from Chapter 3 should be repeated for one clamped and one free boundary conditions in order to obtain a complete description of the mean projected length $1 - \langle L_{||}\rangle/L$ as a function of reduced force $\bar{F}$.

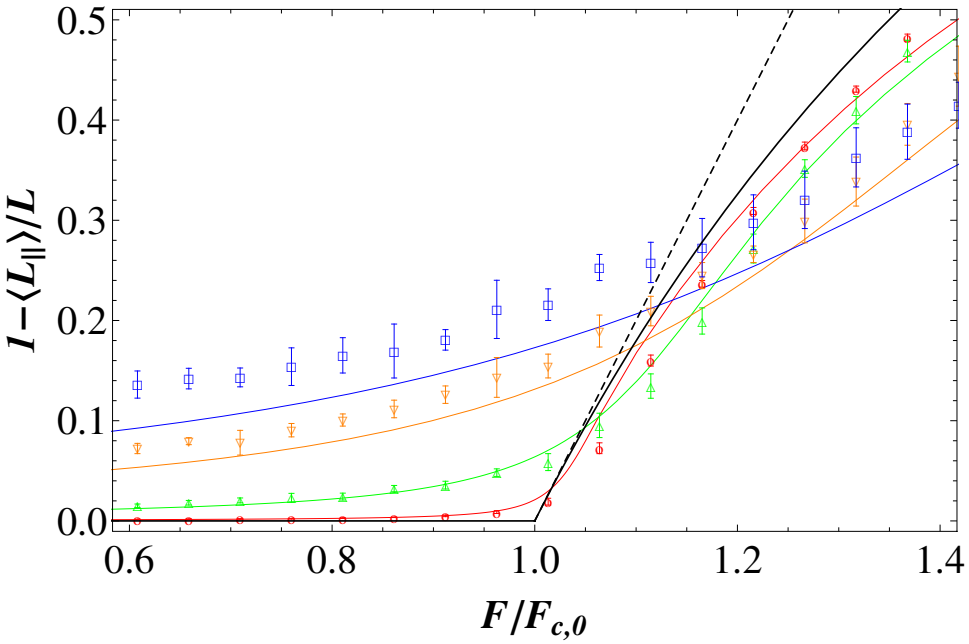

Figure 4.4: Monte Carlo simulation results for buckling of a filament in two spatial dimensions with both ends clamped. Reduced projected length $\langle L_\parallel \rangle / L$ as a function of the reduced force $F/F_{c,0}$ for $L_p/L = 100$ (red, $\circ$), 10 (green, $\triangle$), 2 (orange, $\triangledown$), and 1 (blue, $\square$) corresponding to $\bar{T} \simeq 10^{-3}, 10^{-2}, 5\times10^{-2}$, and 10^{-1}. The error bars are calculated as the standard deviation of the mean value $\langle L_\parallel \rangle$ for 3000 measurements for one step size of force. The solid curves show the analytic result (3.59) for filaments in two spatial dimensions with both ends clamped. The black line corresponds to the zero temperature solution in Fig. 2.3 and the dashed line corresponds to the linear approximation (2.23).

One can notice that in both cases of boundary conditions considered in simulations for the stiffness parameter $L_p/L = 100$ (red circles) the $T = 0$ solution (black solid line) can be considered as a good approximation for reduced projected force $\langle L_\parallel \rangle / L_{c,0}$ as a function of the reduced force $F/F_{c,0}$.

4.3.2 Projected length as a function of contour length

From our Monte Carlo simulations we can also obtain the results for the reduced projected length $\langle L_\parallel \rangle / L_{c,0}$ as a function of the reduced contour length $\bar{L}$. Note that for fixed force we have the relation $L/L_{c,0} \equiv \sqrt{F/F_{c,0}}$, see Chapter 2. In Fig. 4.6 we present the MC simulation data for this relation together with the analytical solution (3.67). Also in this case we observe a good agreement between the simulation results and the analytical solution for $\langle L_\parallel \rangle / L_{c,0}$. The existence of a cusp rounded by thermal fluctuations close to the critical length L_c predicted in Chapter 3 is also clearly confirmed.

The case of a filament with one end clamped and one end free is presented in Fig. 4.7. One can see that the shortening for filaments with one free end is larger than for filaments with both ends clamped. This can again be explained by the fact that a filament with one free and one clamped end behaves similarly to a filament with both ends clamped at a reduced temperature $\bar{T}$, which is twice as large. Note, that also for filaments with one end free the stretching effect occurs. Finally, also for these boundary conditions the $T = 0$ solution (black solid line) can be still considered as a good approximation for $L_p/L = 100$ (red circles).

The relation between the reduced projected length $\langle L_\parallel \rangle / L_{c,0}$ and the reduced contour length $\bar{L}$ can be estimated from our analytical results the relation between a filament with one free and one clamped end of length L and a filament with two clamped ends of length $2L$ but a full calculation is required in order to find the exact relation for $\langle L_\parallel \rangle / L_{c,0}$ as a function of $\bar{L}$ in case

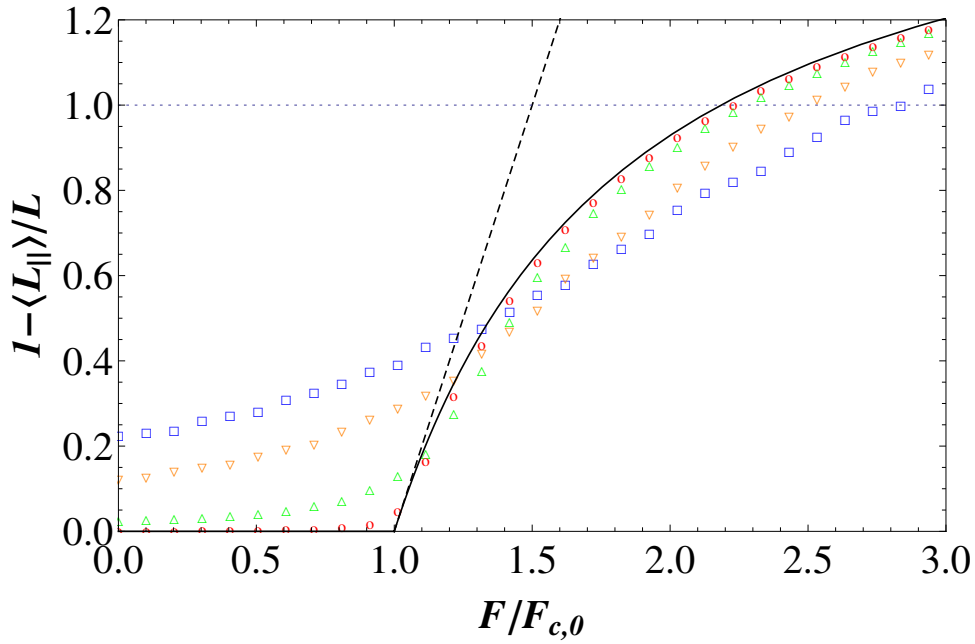

Figure 4.5: Monte Carlo simulation results for buckling of a filament in two spatial dimensions with one end free and one end clamped. Reduced projected length $\langle L_\parallel \rangle / L$ as a function of the reduced force $F/F_{c,0}$ for $L_p/L = 100$ (red, ∘), 10 (green, △), 2 (orange, ▽), and 1 (blue, □) corresponding to $\bar{T} \simeq 10^{-3}, 10^{-2}, 5 \times 10^{-2}$, and 10^{-1}. The black line corresponds to the zero temperature solution from Fig. 2.3 and the dashed line corresponds to the linear approximation (2.23). The dotted line corresponds to a loop configuration when $\langle L_\parallel \rangle = 0$.

of filaments with one free and one clamped end.

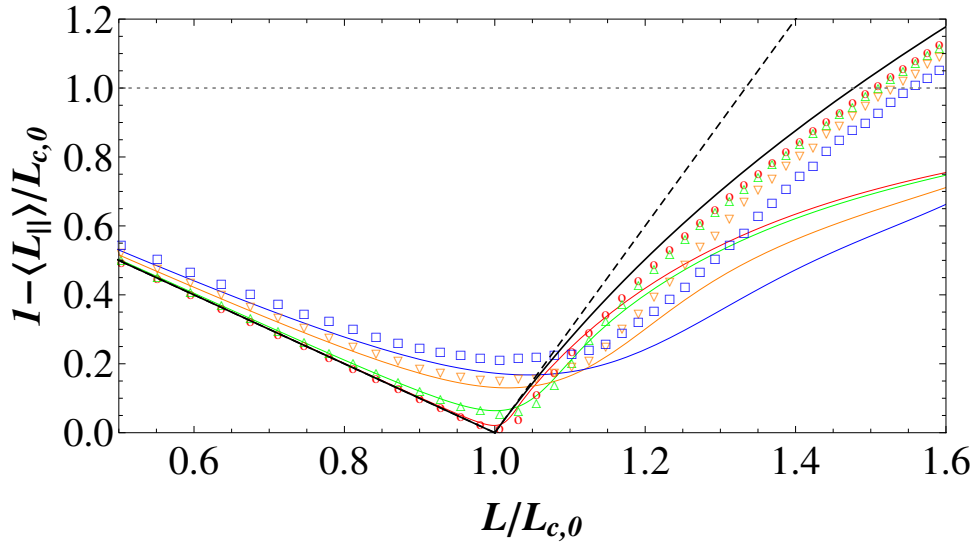

Figure 4.6: Monte Carlo simulation results for buckling of a filament in two spatial dimensions with both ends clamped. Reduced projected length $\langle L_\parallel \rangle / L_{c,0}$ as a function of the reduced contour length $L/L_{c,0}$ for $L_p/L = 100$ (red, ∘), 10 (green, △), 2 (orange, ▽), and 1 (blue, □) corresponding to $\bar{T} \simeq 10^{-3}, 10^{-2}, 5 \times 10^{-2}$, and 10^{-1}. The solid curves show the analytic result (3.59). The black line corresponds to the zero temperature solution from Fig. 2.4 and the dashed line corresponds to the linear approximation (2.25). The dotted line corresponds to a loop configuration when $\langle L_\parallel \rangle = 0$.

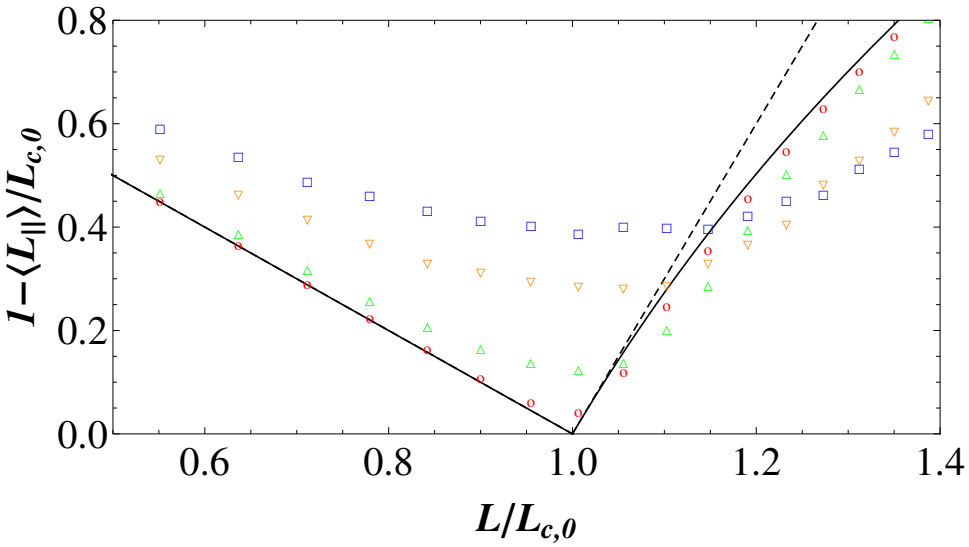

Figure 4.7: Monte Carlo simulation results for buckling of a filament in two spatial dimensions with one end free and one end clamped. Reduced projected length $\langle L_\parallel \rangle / L_{c,0}$ as a function of the reduced length $L/L_{c,0}$ for $L_p/L = 100$ (red, ∘), 10 (green, △), 2 (orange, ▽), and 1 (blue, □) corresponding to $\bar{T} \simeq 10^{-3}, 10^{-2}, 5 \times 10^{-2}$, and 10^{-1}. The solid curves show the analytic result (3.59). The black line corresponds to the zero temperature solution from Fig. 2.4 and the dashed line corresponds to the linear approximation (2.25). The dotted line corresponds to a loop configuration when $\langle L_\parallel \rangle = 0$.

4.3.3 Monte-Carlo Simulations in tangent angle representation

For the case of two spatial dimensions it is possible to rewrite the simulation code in the tangent angle representation. This allows for another check of our analytical predictions from Chapter 3.

In this Section we simulate discretized versions of both the full Hamiltonian (3.2) and its fourth order approximation (3.31). In these simulations, we employ clamped boundary conditions at both ends of the filament. For free boundary conditions, also the simulation in tangent angle representation is complicated by the fact that the filament "flips around" and reaches its trivial absolute minimum at $\phi(s) = \pi$ (for the Hamiltonian (3.2)) by thermal activation out of the metastable buckled state. In the configuration $\phi(s) = \pi$ the end points have crossed corresponding to a filament that is stretched rather than compressed by the force F.

For the Monte Carlo simulation in tangent angle representation we discretize the inextensible filament into N segments of fixed length $b \equiv L/N$ with angles $\phi_i \equiv \phi(ib)$. In order to equilibrate the filament, we use two kinds of MC moves: (i) a local move in real space, which changes the angles of two neighboring segments $\phi_i \to \phi_i + \Delta\phi$ and $\phi_{i-1} \to \phi_{i-1} - \Delta\phi$ in opposite directions and, thus, induces a displacement of the point connecting both segments in the direction perpendicular to the local filament orientation; (ii) a collective move in Fourier space, which changes the amplitude $\tilde{\phi}_n$ of Fourier mode n by a random amount, $\tilde{\phi}_n \to \tilde{\phi}_n + \Delta\tilde{\phi}$. For the simulation results shown in Figs. 4.8 and 4.9, we used a discretization into $N = 200$ segments and performed 8×10^6 MC sweeps alternating local moves and moves in Fourier space. We perform both simulations of the full model (3.2) (see (a) in Figs. 4.8 and 4.9) and of a model where we use the fourth order approximation (3.31) (see (b) in Figs. 4.8 and 4.9).

The simulation results for the reduced projected length $\langle L_\parallel \rangle / L$ as a function of the reduced force $\bar{F}$ in Fig. 4.8 are in good agreement with our analytical result (3.59). Deviations become appreciable for the largest values of the reduced temperature $\bar{T} \simeq 10^{-1}$ for which we performed simulations. For these values it becomes necessary to include higher order terms in the expansion in $\bar{T}$ underlying the analytical result (3.59). In particular, also the MC simulations confirm that curves for the mean projected length $\langle L_\parallel \rangle$ as a function of force, taken at different temperatures

$\bar{T}$, *intersect* in the vicinity of the buckling force. The perfect agreement of the simulation data and the analytical results in (b) (even for large forces) is caused by the fact that only the fourth order approximation of (3.31) is simulated.

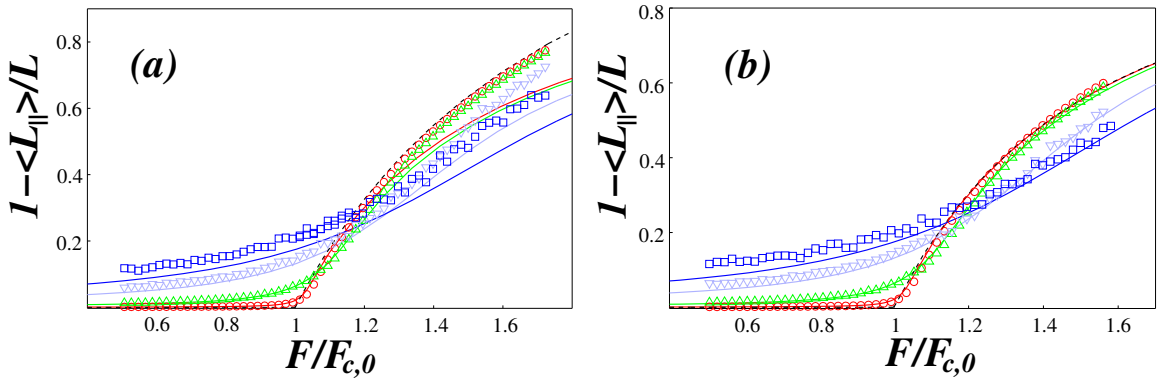

Figure 4.8: Results of Monte Carlo simulation in tangent angle representation for filament with both ends clamped. Reduced projected length $\langle L_\parallel\rangle/L$ as a function of the reduced force $F/F_{c,0}$ for $L_p/L = 100$ (red, ○), 10 (green, △), 2 (light blue, ▽), and 1 (blue, □) corresponding to $\bar{T} \simeq 10^{-3}, 10^{-2}, 5\times10^{-2}$, and 10^{-1}. The solid curves show the analytic result (3.59). The dashed black line corresponds to the zero temperature solution from Fig. 2.3. (a) Comparison with Monte Carlo simulation data for two clamped ends using the full model (3.2). (b) Comparison with Monte Carlo simulation data for two clamped ends using the fourth order approximation of eq. (3.31). The analytical zero temperature solution $1 - L_\parallel/L = 1 - \bar{F}^{-2}$ is included as a dashed line. The dotted line corresponds to a loop configuration when $\langle L_\parallel\rangle = 0$.

Also the MC results for the reduced projected length $\langle L_\parallel\rangle/L_{c,0}$ as a function of the reduced contour length $\bar{L}$ are in good agreement with the analytical result (3.67). The existence of a cusp rounded by thermal fluctuations close to the critical length L_c is clearly confirmed. Also in Fig. 4.9 (b) the perfect agreement (even for large contour lengths) of the simulation data and the analytical results is caused by the fact that only the fourth order approximation of (3.31) is simulated.

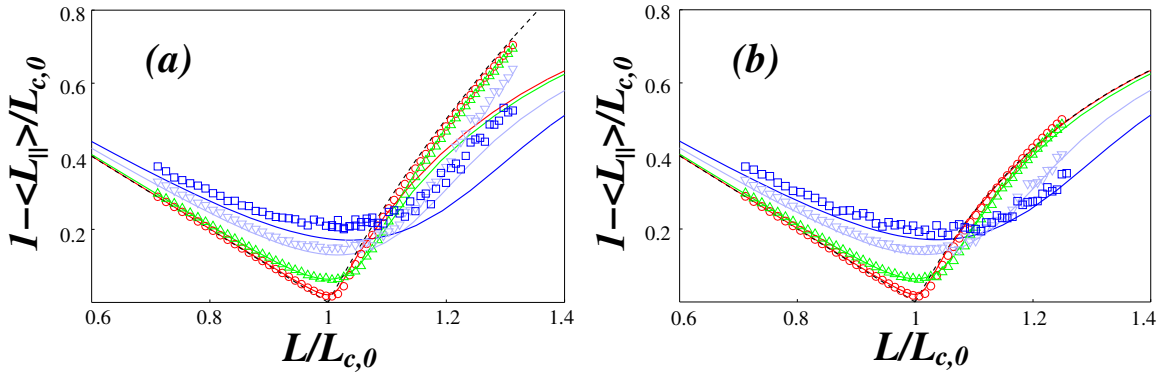

Figure 4.9: Results of Monte Carlo simulation in tangent angle representation for filament with both ends clamped. Reduced projected length $\langle L_\parallel\rangle/L_{c,0}$ as a function of the reduced contour length $L/L_{c,0}$ for $L_p/L = 100$ (red, ○), 10 (green, △), 2 (light blue, ▽), and 1 (blue, □) corresponding to $\bar{T} \simeq 10^{-3}, 10^{-2}, 5\times10^{-2}$, and 10^{-1}. The solid curves show the analytic result. (a) Comparison with Monte Carlo simulation data for two clamped ends using the full model (3.2). The analytical zero temperature solution from Fig. 2.4 is shown as dashed line. (b) Comparison with Monte Carlo simulation data for two clamped ends using the fourth order approximation of eq. (3.31). The analytical zero temperature solution $1-L_\parallel/L = 1-\bar{L}^{-4}$ is included as a dashed line.

4.4 Buckling in three spatial dimensions

In this Section we present the results of MC simulations of buckling instabilities of a fluctuating filament in three spatial dimensions. In this case the tangent vector $\mathbf{t}$ has three components. The projected length $\langle L_{||} \rangle$ is again the end-to-end distance projected on the z-axis, since there is no torsion and buckling occurs in one plane. The simulations are performed for a discrete worm-like chain with $N = 100$ beads, see 4.6. Also in three spatial dimensions we investigate four cases of stiffness parameter values, i.e., $L_p/L = 100$ (red, $\circ$), 10 (green, $\triangle$), 2 (orange, $\triangledown$), and 1 (blue, $\square$) corresponding to $\bar{T} \simeq 10^{-3}, 10^{-2}, 5 \times 10^{-2}$, and 10^{-1} and present the results in Figs. 4.11 and 4.12. In Fig. 4.10 (a) and (b) we present a sample configuration of a filament with $N = 100$ beads in $d = 3$ spatial dimensions before and after buckling, respectively.

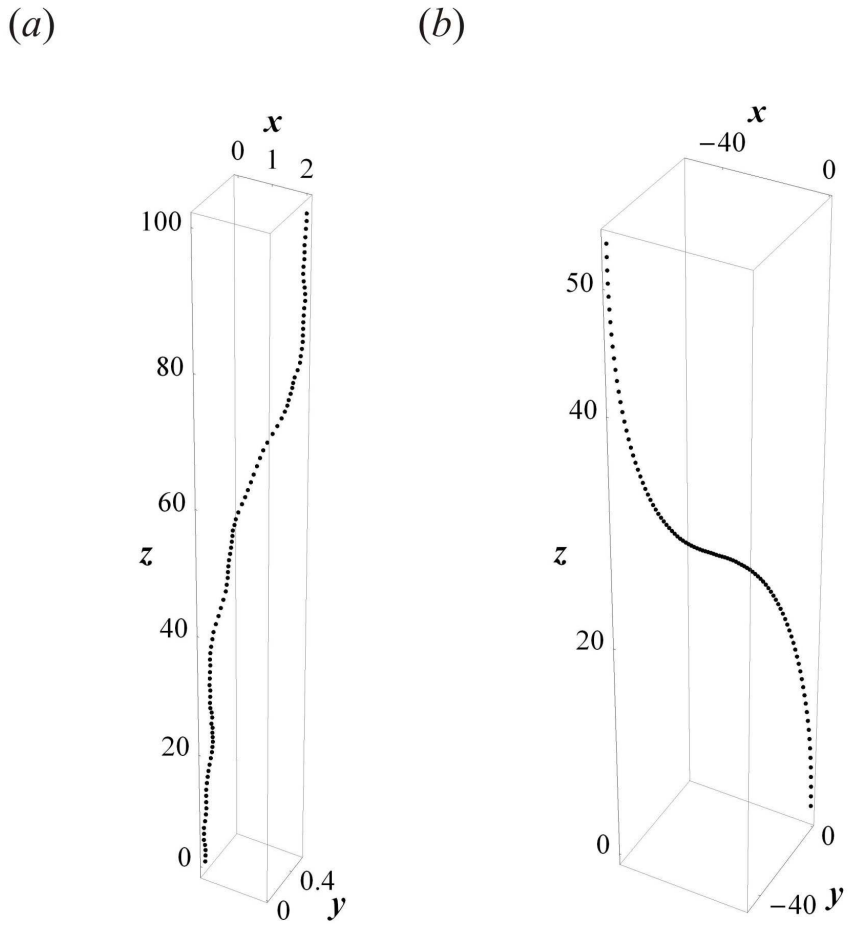

Figure 4.10: Snapshots of filament configurations in $d = 3$ spatial dimensions for $L_p/L = 100$ corresponding to $\bar{T} \simeq 10^{-3}$ with both ends clamped. Monte Carlo simulation data for (a) unbuckled configuration and (b) the buckled configuration. The buckled filament lies on one plane since there is no torque at its ends. Only the thermal fluctuations move the filament out of the plane. The unbuckled filament has the length $L = \sigma \cdot N$ what corresponds to $z = 100$.

4.4.1 Projected length as a function of applied force

First we present the force-extension relation for buckling. The simulation results for the reduced projected length $\langle L_\parallel \rangle / L$ as a function of the reduced force $\bar{F} \equiv F/F_{c,0}$ for filaments with both ends clamped in (a) in Fig. 4.3. In (b) we present simulation data for filaments with one free and one clamped end. One can see that in the case of a filament in three spatial dimensions with both

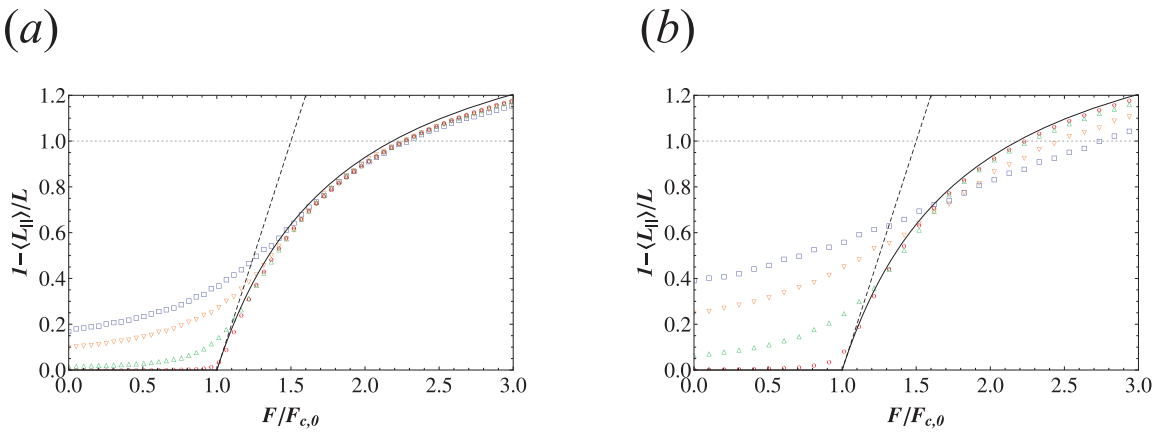

Figure 4.11: Reduced projected length $\langle L_\parallel \rangle / L$ as a function of the reduced force $F/F_{c,0}$ for $L_p/L = 100$ (red, $\circ$), 10 (green, $\triangle$), 2 (orange, ∇), and 1 (blue, $\square$) corresponding to $\bar{T} \simeq 10^{-3}, 10^{-2}, 5 \times 10^{-2}$, and 10^{-1}. Monte Carlo simulation data for filaments in $d = 3$ spatial dimensions with (a) both ends clamped and (b) one free and one clamped end. The black line corresponds to the zero temperature solution from Fig. 2.3 and the dashed line corresponds to the linear approximation 2.23. The dotted line corresponds to a loop configuration when $\langle L_\parallel \rangle = 0$.

ends clamped the intersection of force-extension curves for different values of stiffness parameter L_p/L is difficult to confirm before the filament forms a loop. In this case we observe a very weak stretching effect caused by thermal fluctuations, compare results from Section 4.3. The filament is governed by entropy and an increasing temperature leads to shortening of the filament in order to maximize its configurational entropy. However, for filaments with one clamped and one free end ((b) in Fig. 4.11) the stretching effect is much more pronounced for large forces $F/F_{c,0}$ and before the filament creates a loop, i.e., for $1 - \langle L_\parallel \rangle / L < 1$. Note, that at $T = 0$ a buckled rod of contour length L with one clamped and one free end behaves in the same way as a filament with both ends clamped but with contour length $L/2$, see Chapter 2. One can expect a similar behavior in the presence of thermal fluctuations where this leads to an effective temperature $\bar{T}$, which is twice as high for a filament with one free and one clamped end as compared to a filament with two clamped ends. Therefore, the effect of thermal fluctuations is more pronounced for a filament with one end free and one end clamped.

4.4.2 Projected length as a function of contour length

Also for the case of three spatial dimensions we can obtain the reduced projected length $\langle L_\parallel \rangle / L_{c,0}$ as a function of the reduced contour length $\bar{L} = L/L_{c,0}$. The simulation data are presented in Fig. 4.12 (a) and (b) for filaments with both ends clamped and filaments wit one clamped and one free end, respectively. Note that in case of $d = 3$ there also exists a cusp rounded by thermal fluctuations close to the critical length L_c. One can observe, that for large reduced length $L/L_{c,0}$ changing the boundary conditions to one free and one clamped end (b) in Fig. 4.12 leads to intersection of force-extension curves for different stiffness parameters L_p/L and the minima of $\langle L_\parallel \rangle / L_{c,0}$ is larger then for the case when both ends of filament are clamped.

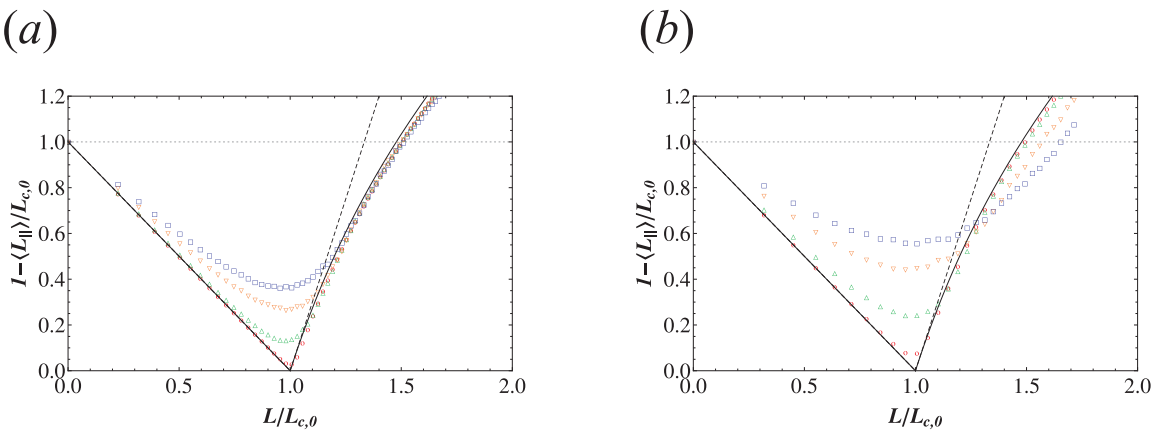

Figure 4.12: Reduced projected length $\langle L_\parallel \rangle / L$ as a function of the reduced contour length $\bar{L} \equiv L/L_{c,0}$ for $L_p/L = 100$ (red, ○), 10 (green, △), 2 (orange, ▽), and 1 (blue, □) corresponding to $\bar{T} \simeq 10^{-3}, 10^{-2}, 5 \times 10^{-2}$, and 10^{-1}. Monte Carlo simulation data for filaments in $d = 3$ spatial dimensions with (a) both ends clamped and (b) one free and one clamped end. The black line corresponds to the zero temperature solution from Fig. 2.4 and the dashed line corresponds to the linear approximation (2.25). The dotted line corresponds to a loop configuration when $\langle L_\parallel \rangle = 0$.

4.4.3 The rotation of a buckled filament induced by thermal fluctuations

For the case of three spatial dimensions one can easily imagine how the filament's configuration looks like. The filament end can move in space (freely for the case of a filament with one end free). Therefore, we can project the end of the filament on the plane perpendicular to the acting compressional force $\mathbf{F}$, i.e., the xy-plane.

For the case of a filament with both ends clamped as well as for a filament with one end free we observe that after the filament buckles it conserves its shape under thermal fluctuations and starts to rotate around the z-axis (axis parallel to the compressional force). One can show that the end position of the filament before buckling is Gaussian distributed within the xy-plane [59]. For finding the probability density for the position of the filament tip after buckling one could adapt the result from [60]. The projections of the end of the filament with $L_p/L = 1$ and both ends clamped on the xy- plane before and after buckling are presented in the Fig. 4.13 (a) and (b), respectively. The case before buckling corresponds to the force $F = 0.5\ F_{c,0}$. The projected length is smaller than the contour length but the filament is still unbuckled. After buckling, i.e., for $F = 1.5\ F_{c,0}$ one can observe that the end tends to rotate around the z-axis - the outer ring is darker. Since L_p/L corresponds to high temperatures or to more flexible filament, the end can still move a lot on the plane and the outer ring is not very narrow. In Fig. 4.14 (a) and (b) we plot the probability $\Omega(D)$ for finding the projected end at distance

$$D = \sqrt{x^2 + y^2} \tag{4.12}$$

from the origin point at $x = y = 0$ before and after buckling, respectively. The large distance D in case of $L_p/L = 1$ before buckling is caused by large fluctuations. The distribution of distances D becomes more narrow after buckling.

The projections on the xy-plane of the end of the filament with $L_p/L = 100$ and both ends clamped before and after buckling are presented in Fig. 4.15 (a) and (b), respectively. The case before buckling corresponds to the force $F = 0.5\ F_{c,0}$. Also for this case one can easily see that the end of the filament is distributed on the xy-plane, see (a) in Fig. 4.13, but it is not far away from the initial point at $x = y = 0$. After buckling, i.e., for $F = 1.5\ F_{c,0}$ one can observe that the end starts to rotate around the z-axis. Since $L_p/L = 100$ corresponds to low temperatures (or semiflexible filaments) the outer ring is very narrow and well visible. This means that after a semiflexible filament buckles most of the fluctuations energy is used for its rotation, i.e., the soft

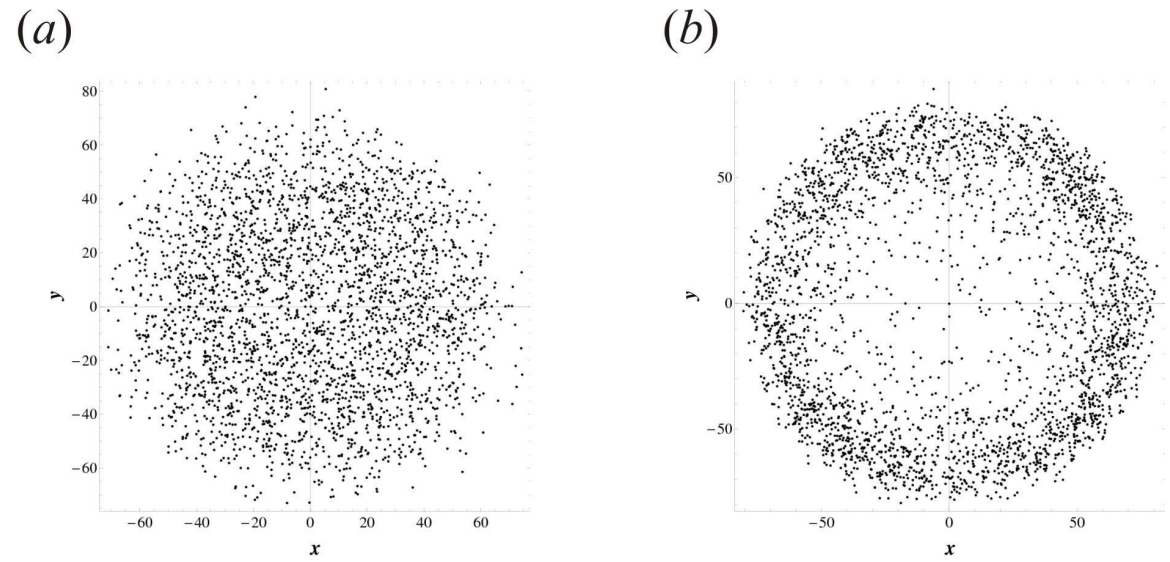

Figure 4.13: Projection of the end of a fluctuating filament in three spatial dimensions on the xy-plane for stiffness parameter $L_p/L = 1$ corresponding to $\bar{T} \simeq 10^{-1}$. Both ends of the filament are clamped. (a) Projection of the end for $F = 0.5\ F_{c,0}$, i.e., before buckling. (b) Projection of the end for $F = 1.5\ F_{c,0}$, i.e., after buckling.

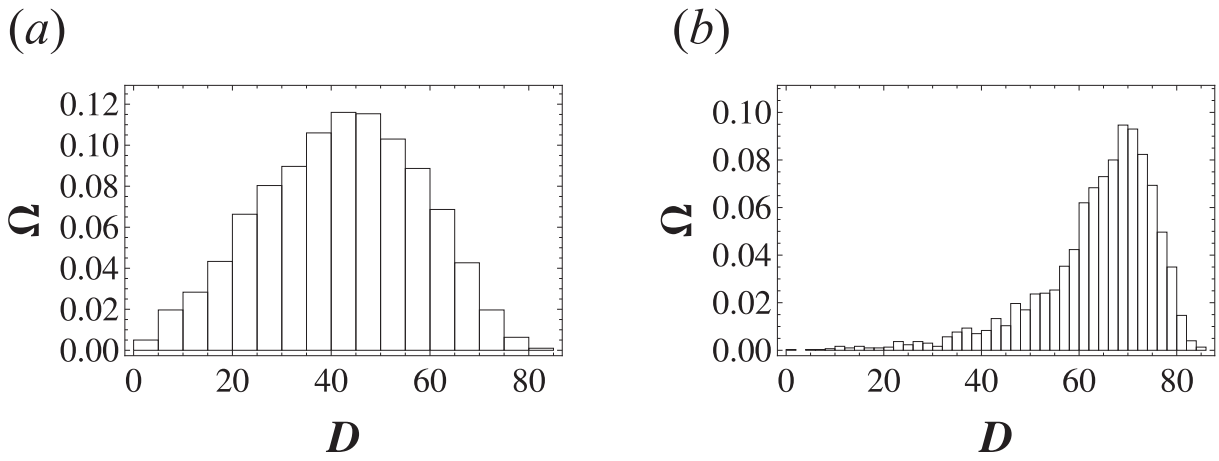

Figure 4.14: Probability $\Omega(D)$ that the end of the filament projected on the xy-plane is at the distance D, see (4.12) for $L_p/L = 1$. (a) before buckling for $F = 0.5\ F_{c,0}$ and (b) after buckling for $F = 1.5\ F_{c,0}$. Both ends of the filament are clamped.

mode gets dominant. In Fig. 4.16 (a) and (b) we plot probabilities $\Omega(D)$ for the case $L_p/L = 100$ representing the probabilities that the projected end of the filament is at the distance D from the origin at $x = y = 0$ before and after buckling, respectively. We confirm a close distance D to the initial point at $x = y = 0$ before buckling and a very narrow peak after buckling, i.e., small fluctuations of the projected end after the filament buckled.

Finally, we can also investigate the projections of the end of the filament with $L_p/L = 100$ and with one end free. These projections on the xy- plane are presented in Fig. 4.17 (a) and (b) before and after buckling, respectively. The case before buckling corresponds to the force $F = 0.5\ F_{c,0}$ and the end of the filament is distributed on the xy-plane, see (a) in Fig. 4.17. After buckling (for $F = 1.5\ F_{c,0}$) one observes that the end starts to rotate around the z-axis. However, since the projected end can freely move the outer ring is not as narrow as for the filament with both ends clamped as presented in Fig. 4.15. This is proven in Fig. 4.18 (a) and (b) where we plot the probabilities $\Omega(D)$ for the case of $L_p/L = 100$ and filament with one

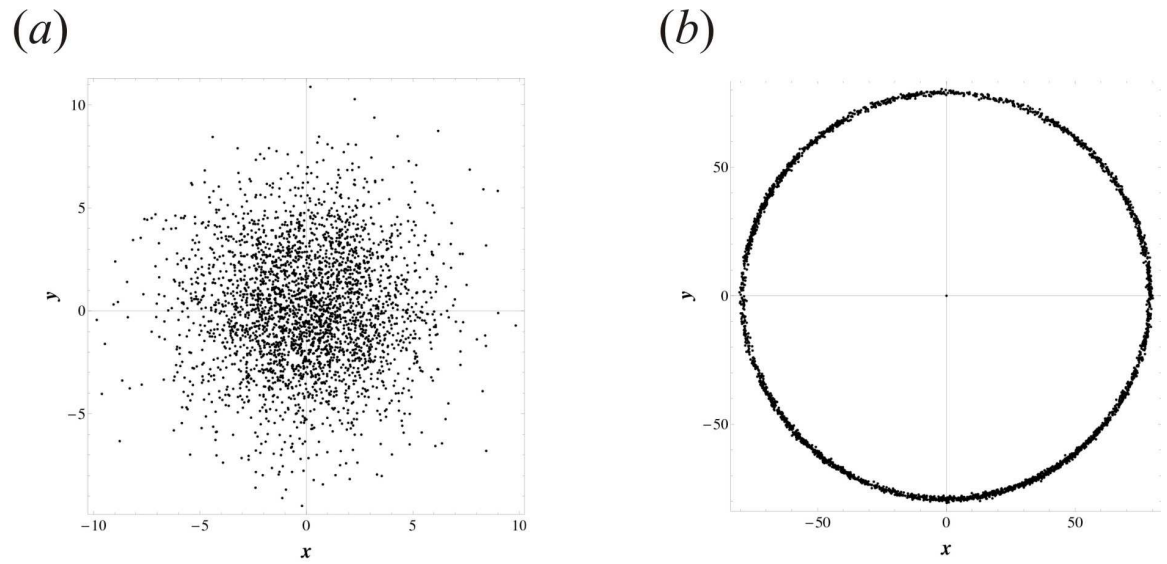

Figure 4.15: Projection of the end of a fluctuating filament in three spatial dimensions on the xy-plane for stiffness parameter $L_p/L = 100$ corresponding to $\bar{T} \simeq 10^{-3}$. Both ends of the filament are clamped. (a) Projection of the end for $F = 0.5\ F_{c,0}$, i.e., before buckling. (b) Projection of the end for $F = 1.5\ F_{c,0}$, i.e., after buckling.

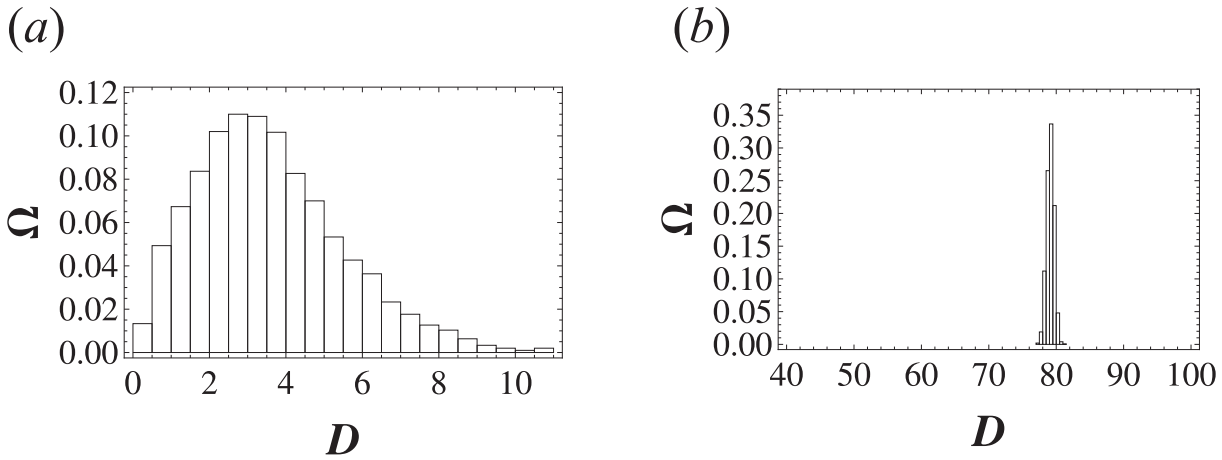

Figure 4.16: Probability $\Omega(D)$ representing the probability that the end of the filament projected on the xy-plane is at the distance D, see (4.12) for $L_p/L = 100$. (a) before buckling for $F = 0.5\ F_{c,0}$ and (b) after buckling for $F = 1.5\ F_{c,0}$. Both ends of the filament are clamped.

free end. The distance D from the origin point at $x = y = 0$ before buckling is larger than for the case of a filament with both ends clamped. We also confirm a broader peak in (b) in Fig. 4.18 which means that the end moves more than the end of a filament with clamped boundary conditions.

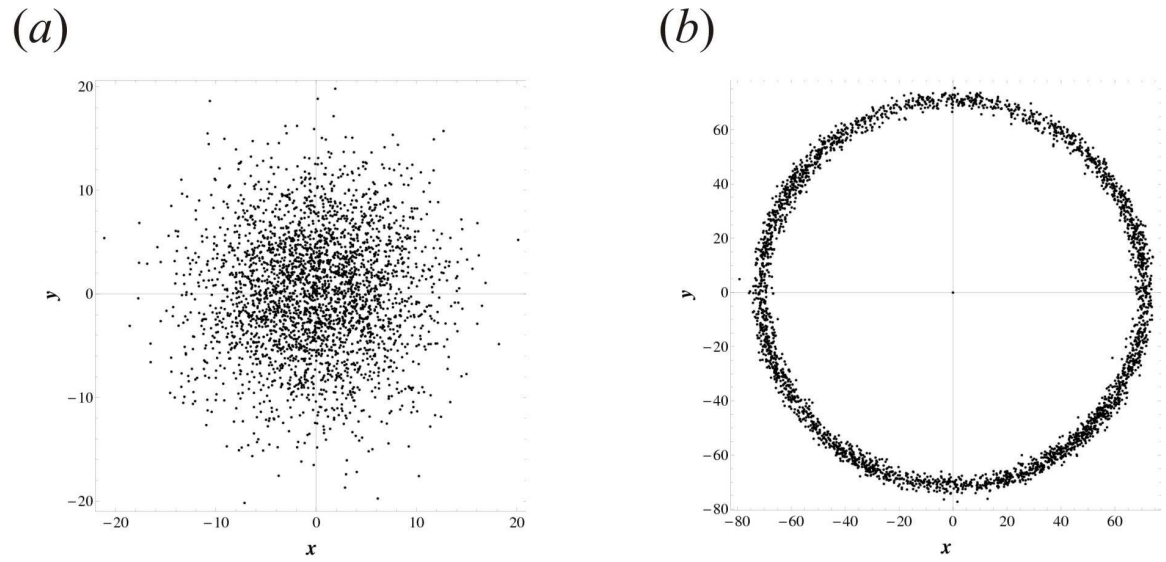

Figure 4.17: Projection of the end of a fluctuating filament in three spatial dimensions on the xy-plane for stiffness parameter $L_p/L = 100$ corresponding to $\bar{T} \simeq 10^{-3}$. Considered is a filament with one end clamped and one end free. (a) Projection of the end for $F = 0.5\ F_{c,0}$, i.e., before buckling. (b) Projection of the end for $F = 1.5\ F_{c,0}$, i.e., after buckling.

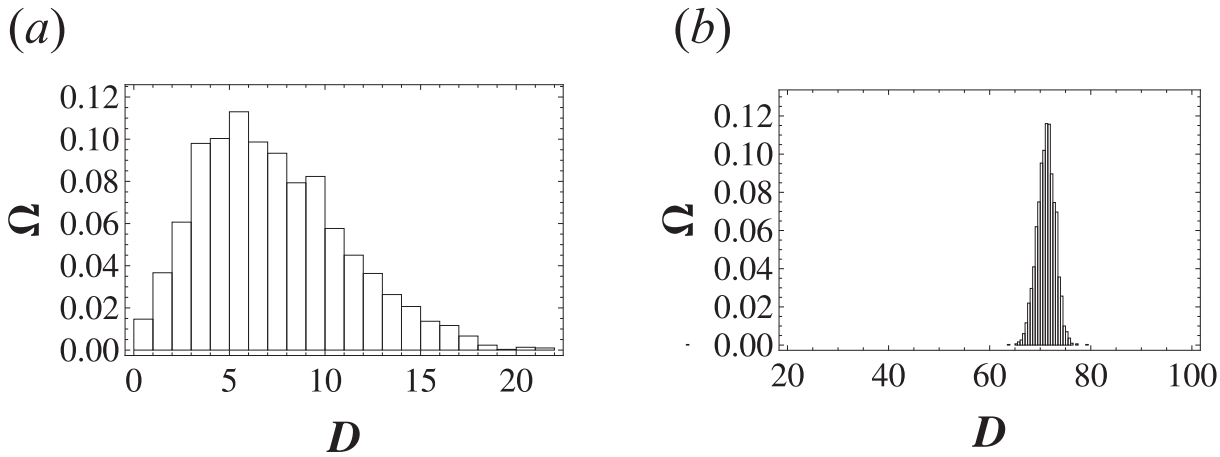

Figure 4.18: Probability $\Omega(D)$ that the end of the filament projected on the xy-plane is at the distance D, see (4.12), for $L_p/L = 100$ and filament with one clamped and one free end. (a) before buckling for $F = 0.5\ F_{c,0}$ and (b) after buckling for $F = 1.5\ F_{c,0}$.

Both for two clamped ends and one free and one clamped end the semiflexible filaments start to rotate after buckling. These results prove that after buckling most of the fluctuations energy is used to rotate the filament, i.e., the soft mode gets dominant.

4.5 Buckling in four spatial dimensions

In this section we expand the simulation code to four spatial dimensions to check if the intersection of simulated force-extension curves for different values of rigidity parameter L_p/L vanishes for dimensions $d > 3$. Again, the simulations are performed for the case of both ends clamped and the case when one end of the filament is free, see Fig. 4.1. For four dimensions the tangent vector $\mathbf{t}(s)$ has four components. Since there is no torque the buckling occurs in one two-dimensional plane, however, now the fluctuations take place in four dimensions. We investigate four cases of stiffness parameter values, i.e., $L_p/L = 100$ (red, $\circ$), 10 (green, $\triangle$), 2 (orange, $\triangledown$), and 1 (blue, $\square$) corresponding to $\bar{T} \simeq 10^{-3}, 10^{-2}, 5\times10^{-2}$, and 10^{-1}. We present results for these simulations in Fig. 4.19 and Fig. 4.20.

4.5.1 Projected length as a function of applied force

In this section we investigate the force-extension relation for buckling in $d = 4$ dimensions. We want to check if the intersection of force-extension curves occurs also in $d > 3$ dimensions and perform MC simulations for a filament with both ends clamped, see (a) in Fig. 4.19 and for a filament with one end clamped and one end free, see (b) in Fig. 4.19.

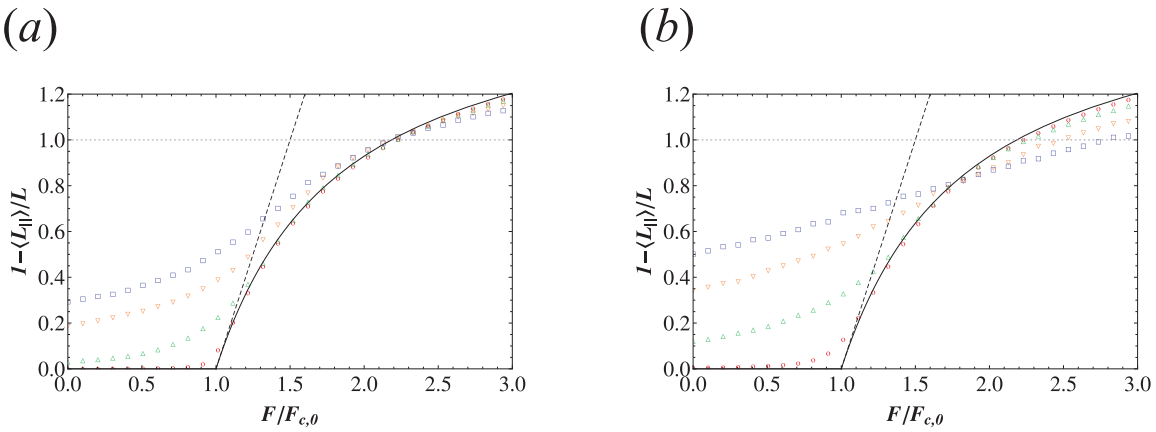

Figure 4.19: Reduced projected length $\langle L_\parallel\rangle/L$ as a function of the reduced force $F/F_{c,0}$ for a filament in four spatial dimensions. (a) Filament with two clamped ends. (b) Filament with one free end and one clamped end. Presented results correspond to $L_p/L = 100$ (red, $\circ$), 10 (green, $\triangle$), 2 (orange, $\triangledown$), and 1 (blue, $\square$) corresponding to $\bar{T} \simeq 10^{-3}, 10^{-2}, 5\times10^{-2}$, and 10^{-1}. The black line corresponds to the analytical zero temperature solution in two dimensions $1 - L_\parallel/L = 1 - \bar{F}^{-2}$ from Fig. 2.3 and the dashed line corresponds to the linear approximation (2.23). The dotted line corresponds to a loop configuration when $\langle L_\parallel\rangle = 0$.

The results presented in Fig. 4.19 prove that also for filaments in four spatial dimensions changing of the boundary conditions leads to a significant change of force-extension relation after the filament buckles.

One can observe that the intersection of force-extension curves for different values of stiffness parameter L_p/L does not occur for two clamped ends until the filament attains a looped configuration, i.e., for $1 - \langle L_\parallel\rangle/L > 1$. For filaments with one free end one can observe, however, the intersection occurs before the filament creates a loop, i.e., for $1 - \langle L_\parallel\rangle/L < 1$. The reason for this behavior is again the fact that a filament of contour length L with one free end behaves at $T = 0$ like a filament with both ends clamped but with contour length $2L$ since also for $d = 4$ the buckling occurs in one plane (no torque), see previous sections.

4.5.2 Projected length as a function of contour length

Analogous to the previous sections also for filaments in four spatial dimensions one can observe the reduced projected length $\langle L_\parallel \rangle / L_{c,0}$ as a function of the reduced length $L/L_{c,0}$. These results are presented for two clamped ends and one end free in (a) and (b) in Fig. 4.20, respectively. We observe, that for large reduced length $L/L_{c,0}$ changing of the boundary conditions to one free and one clamped end (b) leads to intersection of data points for different stiffness parameters L_p/L. Also the minima of $\langle L_\parallel \rangle / L_{c,0}$ is larger then for the case when both ends of filament are clamped.

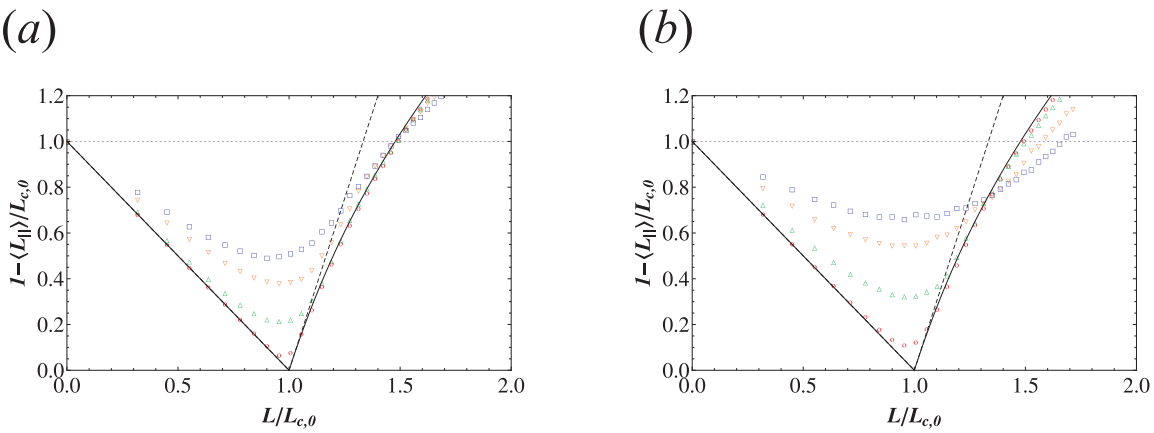

Figure 4.20: Reduced projected length $\langle L_\parallel \rangle / L_{c,0}$ as a function of the reduced length $L/L_{c,0}$ for filament in four spatial dimensions. (a) Filament with two clamped ends. (b) Filament with one free end and one clamped end. Presented results correspond to $L_p/L = 100$ (red, $\circ$), 10 (green, $\triangle$), 2 (orange, $\triangledown$), and 1 (blue, $\square$) corresponding to $\bar{T} \simeq 10^{-3}, 10^{-2}, 5 \times 10^{-2}$, and 10^{-1}. The black line corresponds to the analytical zero temperature solution in two dimensions $1 - L_\parallel/L = 1 - \bar{F}^{-2}$ from Fig. 2.4 and the dashed line corresponds to the linear approximation (2.25). The dotted line corresponds to a loop configuration when $\langle L_\parallel \rangle = 0$.

The results presented above lead to conclusion that changing the boundary conditions causes a significant change in the behavior of a fluctuating filament after buckling. In the case of one free end and one clamped end thermal fluctuations always lead to stretching of the filament also in case of fluctuations in four dimensions.

4.6 Summary

In this chapter we presented results of Monte Carlo simulations for buckling instabilities of thermally fluctuating filaments. The simulations were performed for the cases of two, three and four spatial dimensions. We investigated two different kinds of boundary conditions, i.e., filaments with both ends clamped and filaments with one end clamped and one free end. Our analytical model for buckling (with both ends clamped) in two spatial dimensions in the presence of thermal fluctuations is confirmed by the simulation results.

Using the computer simulation method we showed that changing the boundary conditions causes a significant change in the behavior of a fluctuating filament after buckling. In the case of one free end and one clamped end, thermal fluctuations always lead to stretching of the filament.

We showed that for the case of two spatial dimensions thermal fluctuations lead to stretching of the filament after it buckles both for clamped boundary conditions and for mixed boundary conditions. The theoretically predicted intersection of force-extensions curves for different stiffness parameters L_p/L is confirmed as can be seen in Fig. 4.3. This phenomenon is much less pronounced in $d > 2$ dimensions. For three spatial dimensions the intersection of force-extension curves is difficult to confirm. However, changing the boundary conditions to one free and one clamped end, we showed that in this case the intersection occurs also for $d > 2$, see Figs. 4.11 (b) and 4.19 (b).

Since a filament of contour length L with one free end behaves at $T = 0$ like a filament with both ends clamped but with contour length $2L$ one can expect a similar relation in the presence of thermal fluctuations. In this case, however, one expects a different analytical form of the force-extension curve since a different set of Fourier modes should be considered in the analytical approach. Therefore, one can only approximately say, that a filament with one clamped and one free end and $L_p/L = 2$ behaves similar to a filament with both ends clamped and $L_p/L = 1$. It follows then that a filament with one free end and one clamped end behaves as a filament with two clamped ends at a reduced temperature $\bar{T}$ which is twice as large. Note, that the above argument concerns only the case of two spatial dimensions and a complete theory for dimensions higher than two is missing. However, also in $d > 2$ we observe the stretching effect in case of filaments with one clamped and one free end.

Until now we investigated systems where the value of the compressional force was not changing stochastically but always increased (in a deterministic way) so the bent of the filament increased and the mean projected length of the filament always decreased. In the next Chapter we will consider buckling instabilities caused by a stochastically changing compressional force. We will present a stochastic model for buckling under the action of molecular motors. The force generated by the motors will act on a semiflexible filament which will eventually buckle. The value of the acting force will change stochastically in time according to the stepping of molecular motors and processes of binding and unbinding of motors.

Chapter 5

Buckling of semiflexible filaments under the action of molecular motors

5.1 Introduction

In the previous three Chapters we presented the analytical models for buckling in the absence (Chapter 2) and in the presence (Chapter 3) of thermal fluctuations and the Monte Carlo simulation results for buckling of semiflexible filaments in the presence of thermal fluctuations (Chapter 4). We assumed a constant compressional force acting on the filament along the z-axis and did not consider the origin of the force explicitly.

In this Chapter, we present a model for buckling of semiflexible filaments under the action of molecular motors. In this model the compressional force acting on the filament has its origin in the action of motors walking along a clamped filament. First, we describe some basic knowledge about molecular motors and parameters describing a molecular motor walking along a filament. Next, we introduce a model for buckling of a filament under the action of a single molecular motor or several motors. We present a deterministic model and a "semi"-stochastic model and solve them numerically. Finally, we introduce the mean first passage time needed to unbind all motors acting on the filament such that it returns to its straight configuration.

5.1.1 Single Motor on a Bead

Let us consider the motion of a bead transported by a single motor along a filament, possibly subject to an external force [61, 62, 63]. This situation is depicted in Fig. 5.1. The structure of many motors can be investigated using X-ray crystallography and the transport properties of motors have been studied both *in vivo* and *in vitro*. Measurements of transport properties of the motor in vitro are performed in two basic experimental setups: the gliding and the bead assay.

In the **gliding assay**, motors are adsorbed with their cargo domain to a glass substrate, where they are immobilized but not inactivated [64]. When microtubules in the solution come close to the substrate, they are "captured" by the motors. After binding the filaments "glide"

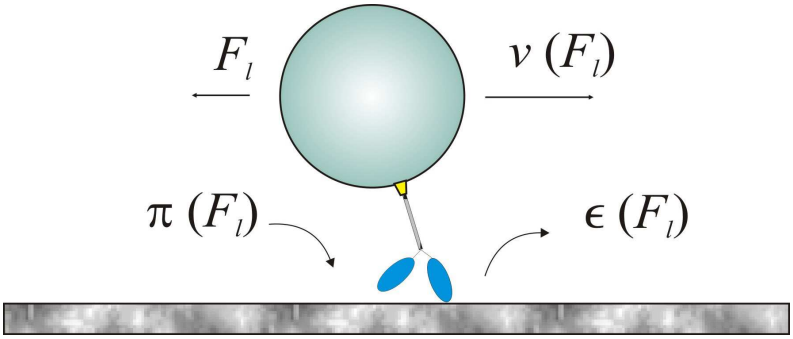

Figure 5.1: Single motor on a bead which is subject to the load force F_l. The motor binds to the filament (grey bar) with rate $\pi(F_l)$ if it is close to the filament. When bound, it walks along the filament with velocity $v(F_l)$ and unbinds from it with rate $\epsilon(F_l)$.

along the surface. In a typical gliding assay more than one motor drives the motion of a single microtubule. In the **bead assay**, microtubules are attached to the substrate, and the motors, bound to a bead, diffuse in the solution until they find a microtubule, bind to it and walk along it [22, 65]. The motion of the bead can then be monitored in a light microscope. In order to acquire information about the motion of a single motor, the bead assay is more useful, because in a typical bead assay it is only a single motor that propels the bead (in opposite to the gliding assay).

In a bead assay, an **optical tweezer** can be employed. In this way the exerted force can be controlled. An optical trap uses laser light to manipulate microscopic dielectric objects [22, 66, 67]. The radiation pressure from a focused laser beam is able to trap small particles. In the biological sciences, these instruments can be used to apply forces in the pN-range and to measure displacements of objects ranging in size from 10 nm to over 10 μm. When a bead with a single motor is trapped, it allows us to study the motion of this single motor under controlled force.

We present now a coarse-grained model of a single motor on a bead [61, 62, 63]. This model will be used in Chapter 5. Following the convention of the literature, the force F_l exerted by the optical tweezer is taken to be positive if it opposes the motor motion, i.e., if it is a 'load' for the motor. Therefore, we will call the force acting on the load the **load force** F_l. When pulling the bead along the filament, the motor has to work against the load force. The best-studied motor is kinesin 1, for which all parameters have been measured, and because of this fact we will consider this motor in further parts of this thesis. In this coarse-grained model, a motor is characterized by the filament unbinding rate $\epsilon(F_l)$, the filament binding rate $\pi(F_l)$, and the velocity $v(F_l)$.

5.1.2 The Binding Rate

Before we can talk about the motor's movement along the filament, the motor has to bind to it. Before binding a motor diffuses in the solution. After it comes close enough to the filament it binds to it. The binding process is complicated on the atomic scale and will not be discussed here. Furthermore, the diffusion of a motor in the solution will be neglected in the next parts of this thesis.

Since there are no experimental data about the force dependence of the motor binding rate $\pi(F_l)$, this dependence is difficult to estimate. If a force F_l acts on the bead when the motor is not bound to the filament, only the motion of the bead-motor complex is affected, and not the motor itself. The motor is in its relaxed state. There could be, however, a weak force-dependence of the binding process once the motor is in contact with the filament. This possibility will be neglected in this thesis. Therefore, when the bead is close to the filament, the motor binds with the zero-force rate π_0, independently of the force on the bead [61], i.e.,

$$\pi(F_l) = \pi_0 \ . \tag{5.1}$$

The binding rate π of molecular motors is of the order of 1 s^{-1}, see Table 5.1.

5.1.3 The Unbinding Rate

Once a motor is bound to the filament, it moves in its preferred direction given by filament polarity. However, it doesn't stay bound to the filament forever. Because of applied force or stochastic thermal fluctuations the motor unbinds after some time (when the force gets large enough or thermal fluctuations win over the motor-filament binding energy). Assuming that the probability for unbinding is constant in time, the time that the motor stays bound to the filament is distributed exponentially and characterized by a single unbinding rate. When no force acts on the motor, we denote this rate by ϵ_0. For most motors, this rate is of the order of 1 s^{-1}, see Table 5.1. When a force F_l acts on the bead, the unbinding rate increases because the filament-motor bond is put under strain. According to Bell or Kramers predictions the increase of the rate for

the bond breaking process is approximately exponential [68, 69, 70]:

$$\epsilon(F_l) = \epsilon_0 \exp\left(|F_l|/F_d\right), \tag{5.2}$$

where F_d denotes the detachment force. This detachment force F_d can be expressed as $F_d = T/x_c$, where x_c is the extension of the energy barrier between the bound and unbound state and is of the order of 1 nm; F_d is of the order of a few pN.

We assume in (5.2) that the unbinding rate depends only on the absolute value $|F_l|$ of the force. In this thesis we assume that forces acting on the bead are parallel to the filament. In general this is presumably wrong - forces perpendicular and parallel to the filament can make different impact on the motor.

5.1.4 Force-Velocity Relation

As we mentioned before, after the motor bound to the filament it steps along it. For kinesin I motor this happens with a forward rate of around 100 s^{-1} so the motor makes roughly 100 steps per second. Therefore, we can consider the forward motion as a smooth process with velocity v. When no force is applied to the motor, it moves forward with its forward velocity v_0. The motion under force can be studied using an optical trap method. Fig. 5.2(b) shows the force-velocity-curve obtained for kinesin I, [71].

When a load force F_l is applied, the motor velocity v depends on this force. When the load force F_l is acting on the motor, it slows down his motion along the filament. When the load force is increased, the velocity v decreases until the force reaches the stall force F_s and the motor stops ($v = 0$). The decrease is approximately linear and has been observed both for kinesin 1 [72, 71, 73, 74, 65, 75, 76, 66], and cytoplasmic dynein [77]. The motion of such a motor subjected to the opposing load force can be studied in a controlled way in an optical trap experiment [66, 67]. In the presented coarse-grained model the linear decrease is given by

$$v(F_l) = \begin{cases} v_A(\frac{v_0}{v_A} - \frac{F_l}{F_s}) & \text{for } F_l \leqslant 0 \quad \text{(assisting force)} \\ v_0(1 - \frac{F_l}{F_s}) & \text{for } 0 \leqslant F_l \leqslant F_s \quad \text{(substall load force)} \\ v_B(1 - \frac{F_l}{F_s}) & \text{for } F_l \geqslant F_s \quad \text{(superstall load force)} \end{cases} \tag{5.3}$$

where we introduce three regimes of molecular motor movement [63]. All three regimes of the force-velocity relation $v(F_l)$ are plotted in Fig. 5.2. In the first regime, the **assisting force regime**, the applied load force is negative, i.e., forces are pulling in the same direction as the motor walks. In the second regime, the **substall force regime**, the motor moves in its preferred direction and its velocity decreases as the force increases until it stops at $F_l = F_s$. If the motor is subjected to load forces higher than F_s it is forced to walk backwards. This regime is called **superstall force regime**. However, a motor under a high force $F_l \gg F_s \gtrsim F_d$ unbinds very fast due to the exponential increase of the unbinding rate $\epsilon(F_l)$.

One has to remember that the velocity $v(F_l)$ is the **mean velocity** of a single motor. In reality stepping of the motor is a stochastic process. Hence, one should consider the velocity of the motor as a stochastic variable so the value of $v(F_l)$ fluctuates in time. In this case taking the mean value for $v(F_l)$ is a mean field approximation.

When the load force F_l gets large, i.e, $F_l \gg F_s$, the linear form predicts fast backward motion. This regime is experimentally not relevant (and will be also neglected in this thesis) because the stall force of motors is of the same order of magnitude or larger then the detachment force. In further parts we will focus on the substall regime where

$$v(F_l) = v_0(1 - F_l/F_s) \tag{5.4}$$

with v_0 denoting the forward velocity which the motor has when $0 \leqslant F_l \leqslant F_s$ (substall regime).

The presented linear form of the force-velocity relation has several advantages: it captures the essential features of the experimental force-velocity relation, it is simple with not too many

Parameters	kinesin 1	Refs.	dynein	Refs.
Forward velocity v_0	1 $\mu m\ s^{-1}$	[71, 78]	1 $\mu m\ s^{-1}$	[79, 80]
Backward velocity v_B	6 $\mu m\ s^{-1}$	[71]	-	-
Attachment rate π_0	5 s^{-1}	[81]	2.5 s^{-1}	[79, 82]
Detachment rate ϵ_0	1 s^{-1}	[83, 78]	0.5 s^{-1}	[79, 84]
Stall force F_s	6 pN	[83, 76]	1.1 pN or 7 pN	[77, 85, 86] and [84]
Detachment force F_d	3 pN	[83]	-	-

Table 5.1: Single motor parameters of kinesin I and cytoplasmic dynein, taken from the in vitro experiments of the cited references. For parameters with "-" entry no measurements are available [63].

parameters, and allows us a simple analytic and numerical solution of the model equations considered in Chapter 5. It is also of advantage, that it has a unique inverse which will be of importance later.

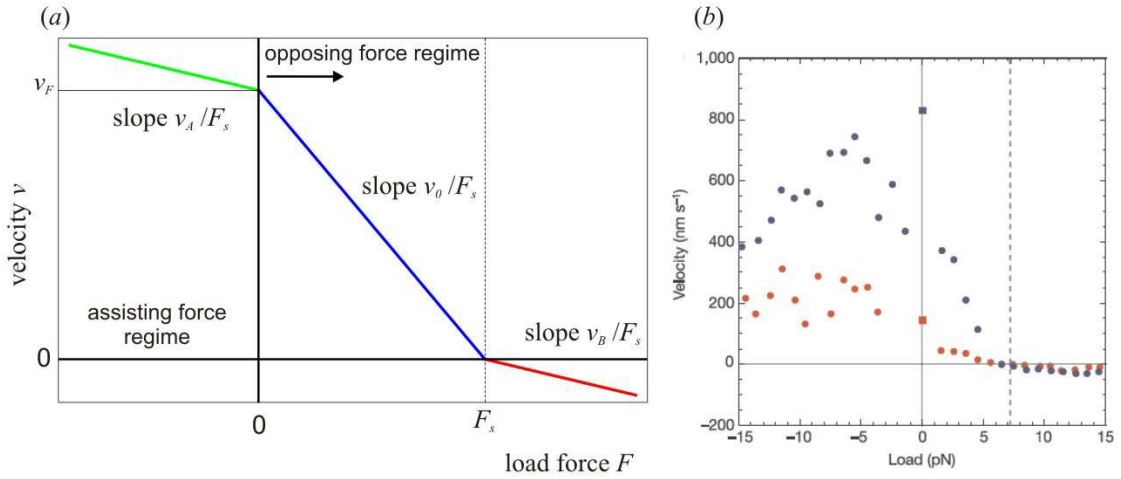

Figure 5.2: Single-motor velocity-force relation: (a) The force-velocity relation $v(F_l)$ is modeled as a function existing in three regimes: assisting force (green line), substall regime (blue line) and superstall regime (red). This relation is given by (5.3) [63]. (b) The force-dependence of the motor velocity has been measured for kinesin 1 in an optical trap which applies a load force on the bead [71]. Red dots are for an ATP concentration of 10 μM, blue dots for $1mM$.

Some estimations for the single motor parameters of kinesin I and cytoplasmic dynein are presented in Table 5.1. The values are taken from the in vitro experiments and corresponding referenced are included. Entries with "-" mean that no measurements are available. In this thesis we will use the kinesin I values for these parameters.

5.2 Buckling under Action of Molecular Motors

In the previous section we reviewed a model describing cargo transport by molecular motors. However, not only vesicles or organelles can be a cargo. Also filaments are transported by motors. The filament is a dynamic structure - it changes its length, bends and buckles. Also thermal fluctuations should not be neglected on the nanoscale. All these phenomena make the cell structure and function very interesting from the physical point of view.

Under compression, a rod (or filament) undergoes **buckling**. It changes its shape dramatically as soon as the applied compressional force exceeds the **critical force**, F_c, also called the Euler force. After it buckled, little additional force is needed to increase bending. The buckling of rods and filaments was the subject of the last three chapters.

We observe such buckling instabilities also under the action of molecular motors. New experimental methods allow us to see the filaments undergoing buckling and to observe the effects of this phenomena both for microtubules [36, 87, 88, 37, 11, 89] and actin filaments [90]. In Fig. 5.3 and 5.4 we present several experimental observations of buckling of filaments.

One can see that the filament in Fig. 5.3 (1) is buckled and the buckling amplitude increases in time. Here, we present a series of images showing bending of GFP-labeled microtubules in a strain that also expresses a fusion of Peb1, the EB1-homologue of *U. maydis* [91] with monomeric red fluorescent protein [92]. A microtubule slides over a second microtubule (arrows) and forms a loop. RFP-Peb1 (arrowhead) indicates that the microtubule slides with plus-end trailing (here, the elapsed time is given in seconds and the bar corresponds to 2 μm) [72]. The origin of this buckling is the action of a molecular motor, see the cartoon (2) in Fig. 5.3. The cartoon illustrates how a plus-end-directed kinesin molecule could accomplish such a bending event. The motor (red) cross-bridges two microtubules in a bundle. Although it walks toward the plus-end of one microtubule, this microtubule is pushed backward and bent [72]. Such a buckling effect can be easily observed using optical microscopy.

Another possibility for buckling of filaments in a cell is the buckling caused by filament growth, see (3) in Fig. 5.3. A filament constantly changes its length because of polymerization and depolymerization processes, see Chapter 1. When the filament polymerizes, its contour length L increases and if this length exceeds the critical length for buckling $L_{c,0}$, see Chapter 2, the filament buckles. One can see here a series of micrographs taken from a real-time video tape recording to show bending of microtubules. One microtubule (arrow) clearly bends (real-time observation of microtubule in vivo). The time in seconds is given in each frame. (The bar corresponds to 10 μm) [93].

In (4) one can see the sliding and bending of a microtubules in FB2rGFPTub1. A stationary contact between microtubules (arrows) appears to support this motion (the bar denotes 2 μm and the time in seconds is given in upper right corner) [71]. Finally, one can see in (5) in Fig. 5.3 that we can observe a lot of buckled filaments in a cell. Here, (a) presents a fixed CHO cell, stained for microtubules (red) and the nucleus (blue), showing highly bent microtubules throughout the cell and the inset shows schematically that microtubules are believed to grow fairly straight and subsequently become bent under the action of intracellular forces (yellow arrowheads). In (b) microtubules undergo significant bending fluctuations in time, as seen by the microtubule highlighted in this GFP-tubulin-transfected CHO cell. Consecutive images are separated by 8 seconds ($t = 0$ at top) [94]. These experimentally observed phenomena lead to the conclusion that a theoretical model for buckling of filaments has many applications.

One of the most spectacular buckling events occurs during cell division, *mitosis*. Filaments under the action of molecular motors are buckled and a characteristic shape of these filaments (*mitotic spindle*) can be observed during the cell division, see Fig. 5.4, (a). The movement of the motors to the opposite ends of the cell leads to the movement of chromosomes [1, 4]. *In vitro* experiments have shown that mixtures of kinesin motors and microtubules can spontaneously create complex spatio-temporal patterns [95]. Analogous self-organization processes are essential for eukaryotic cell division [96]. During mitosis, motor proteins organize microtubules in a bipolar

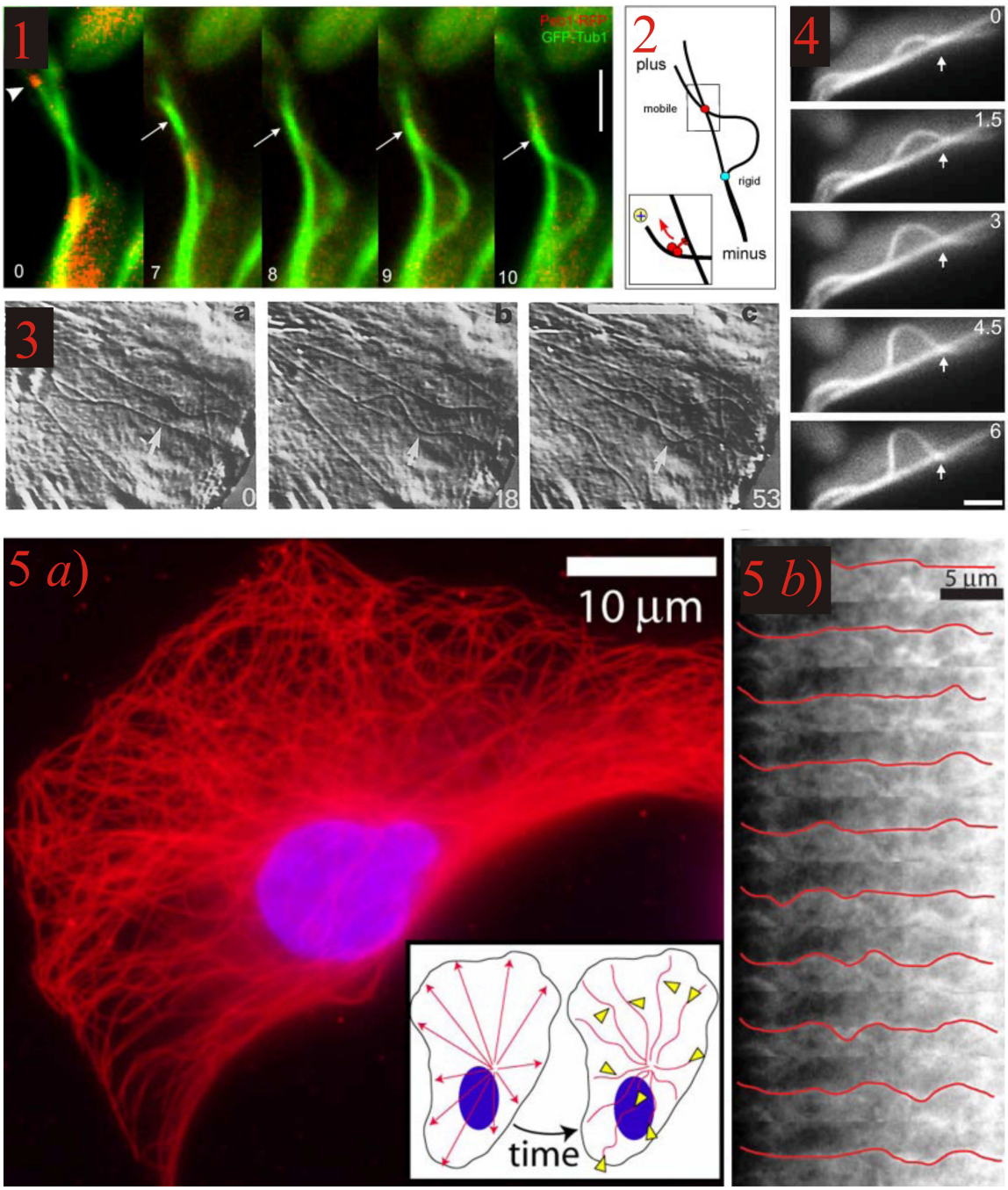

Figure 5.3: Buckling of filaments in biological systems. See text for details.

structure, the *mitotic spindle*, which serves as a scaffold to transmit the necessary forces for chromosome segregation [97]. The spindle consists of two microtubule asters. They overlap in the central region, see Fig 5.4. The microtubules, with their minus-ends located at the aster poles, are crosslinked by many different motors [96, 98]. One particular type of motor, the plus-ended bipolar kinesin (e.g. Eg5 or Klp61F), has been shown to be essential for the stability of the mitotic spindle. A decrease in its concentration below a certain threshold value causes the collapse of the spindle [99, 100], and its total inhibition prevents bipolar spindle formation [101]. Eg5 motors have been shown to drive the microtubule poleward flux [100] and homolog motors to induce the formation of (interpolar) microtubule bundles [102]. Bipolar motors are composed of two connected units, each one composed of two motor domains. Both units can move

simultaneously and independently on microtubules [103]. These motors are able to crosslink the microtubules [102] and slide them with respect to each other when they are in an antiparallel configuration [103], as in the central region of the spindle. As a result, these motors produce an outward force along the spindle axis and generate a microtubule flux toward the poles [100]. Typical forces involved in mitosis are in the nanoNewton range [104]. However, individual motors cannot exert forces larger than a few picoNewtons, so their collective action is required to ensure the stability of the mitotic spindle. At metaphase, this dynamic structure reaches a steady state with microtubules of nearly constant length undergoing permanent treadmilling [100, 105], polymerizing at the plus end and depolymerizing at the minus end. For a full description of mitosis and its phases see [1, 4].

Accurate chromosome segregation is essential for genome inheritance in eukaryotes. Microtubules compose the mitotic spindle and microtubule-based motor proteins play a vital role in mitosis. Several members of the kinesin motor family are involved in spindle formation, chromosome movement, and cytokinesis. Although dynein is not needed for spindle formation or chromosome movements, it plays an important role in orienting the mitotic spindle at the mother-bud neck before cytokinesis [106, 107, 108].

Mitotic functions of cytoplasmic dynein and all 25 kinesins in *Drosophila S*2 cells have been studied in [101]. It has been shown that four kinesins are involved in bipolar spindle assembly, four kinesins are involved in metaphase chromosome alignment, dynein plays a role in the metaphase-to-anaphase transition, and one kinesin is needed for cytokinesis [101].

(1) (2)

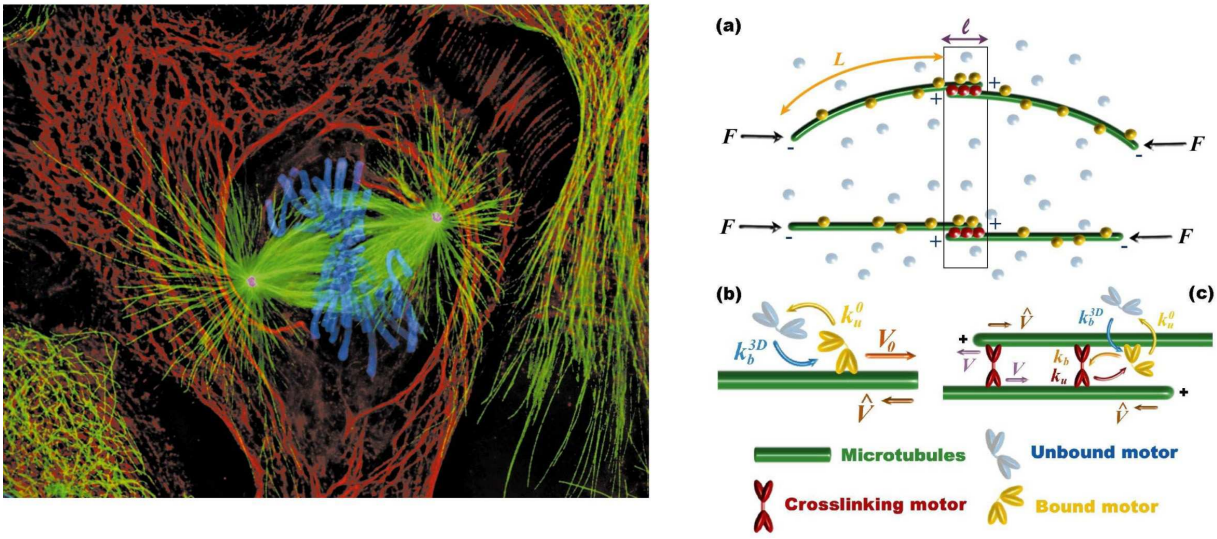

Figure 5.4: (1) Image of a newt lung cell in metaphase stained for centrosomes (magenta), microtubules (green), chromosomes (blue) and intermediate filaments (red). It is a maximal intensity projection through the entire cell volume. From [109]. (2) Cartoon representing the buckling of microtubules in mitotic spindle. (a) Antiparallel array of microtubules under the action of a longitudinal force F. Buckled and non-buckled arrays are shown. The minus and plus ends of microtubules are depicted as $-$ and $+$, respectively. Motors are represented by red and yellow dots. In the non-overlapping region of length L there are no antiparallel filaments and the motors are not subject to any force. The motors in the overlapping region of length ℓ sustain the structure by crosslinking and sliding antiparallel filaments. (b-c) Possible kinetic events of a motor in the non-overlapping region (b) and in the overlapping region (c). The velocities V and $\hat{V}$ are the crosslinking motor velocity and the microtubule poleward velocity, respectively. From [107].

5.3 Model for buckling of semiflexible filaments under the action of molecular motors

As we saw in the previous section, molecular motors play an important role in transport of organelles and the organization of a living cell. In addition, motors can also transport filaments as a cargo, see previous subsections. In this section, we present a model for buckling of semiflexible filaments under the action of molecular motors based on the model for cargo transport by a single molecular motor presented in Fig. 5.1. A cartoon representing the model is shown in Fig. 5.5. We consider a semiflexible filament of contour length L as the cargo (blue rod in Fig. 5.5) and let the motors walk along a filament immobilized, i.e. firmly attached, to a surface (red rod in Fig. 5.5). The bunch of n actively pulling motors consists of n_0 motors at time $t = 0$, i.e., $n(t = 0) = n_0$ and changes during the process because of unbinding and rebinding with rates $\epsilon(F)$ and π, respectively. The total number of motors in the system is given by n_{tot}.

In our model, the load force F_l discussed in section 5.1.1 corresponds to the force acting on the filament as we discussed in Chapters 2 and 3. Since we have n actively pulling motors the effective load force for a single motor is given by [61]

$$F_l = \frac{F}{n} \tag{5.5}$$

if we ignore force fluctuations. This relation corresponds to the assumption that the motors, which are pulling the cargo filament, share the load equally.

One could also use the immobilized filament as a cargo and let the motors walk along the filament with one end free and push it against the wall, compare gliding assay in section 5.1.1.

The obvious condition for buckling is that the critical force $F_{c,0}$ has to be smaller then n times the stall force F_s for a single motor, i.e,

$$F_{c,0} < nF_s \ , \tag{5.6}$$

since we have n motors which share the cargo, see (5.5). Otherwise the motors would not be able to buckle the cargo filament before they start to step backwards along the immobilized filament. Note, that one end of the cargo filament is clamped and one is free and can freely move along the wall. We neglect here, however, the friction forces between the end of the cargo filament and the wall. We also assume that typical velocities are sufficiently small to neglect viscous forces in the surrounding solution. In our model we consider only the component of the force acting parallel to the direction of the walk of molecular motors. In two and three spatial dimensions one should, in general, distinguish tangential and normal components of the force F.

The second approximation that we consider is related to the force-extension relation for buckling. In Chapter 2, we showed that the analytical solution (2.21) at $T = 0$ can be approximated by the linear relation (2.23)

$$1 - \frac{L_{||}}{L} = 2\left(\frac{F}{F_{c,0}} - 1\right). \tag{5.7}$$

This approximation applies to the case when the force after buckling is near the critical force, i.e., for $F \simeq F_{c,0}$. In our model, the projected length $L_{||}$ corresponds to the position x of the bunch of motors from the wall, see Fig. 5.5. One can easily rewrite (5.7) and get the linear equation for the force as a function of position $x \equiv L_{||}$

$$F(x) = \frac{3}{2}F_{c,0} - \frac{x}{2L}F_{c,0} \ . \tag{5.8}$$

Note that x decreases as the motors move towards the wall. Now we can use the linear velocity-force relation of the motors in the substall regime, see (5.3). In case of a bunch of n motors linking two filaments the motors share the load and we get the relation

$$v(F(x)) = -v_0\left(1 - \frac{F(x)}{nF_s}\right), \tag{5.9}$$

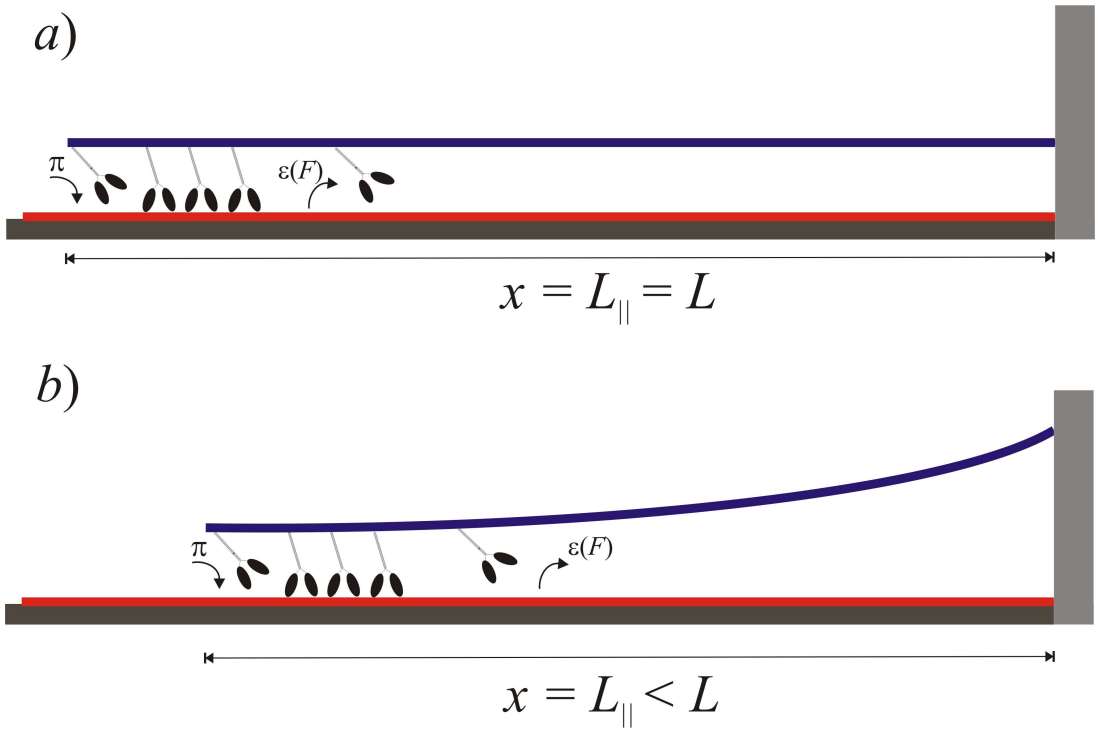

Figure 5.5: Cartoon representing the model for buckling of semiflexible filaments under the action of molecular motors. A bunch of motors is linking two filaments, one immobilized (firmly attached) to the surface (red) and one being displaced and playing the role of a cargo filament (blue). The left end of the cargo filament is clamped and the right end is free and can freely move along the wall (gray). The motors try to step forward along the red filament towards the wall on the right. (a) The unbuckled configuration at time $t = t_0$. The motors cannot exert sufficient force to buckle the cargo filament and the distance x between the left end and the wall is equal to the contour length L. (b) The buckled configuration when the motors move along the red filament and exert the force needed to buckle the cargo filament. The distance x is now equal to the projected length $L_{||}$.

where the minus sign denotes that the motor walks in the wall direction starting from $x = L$, i.e., the distance $x \equiv L_{||}$ decreases with time t when the cargo filament is buckled. Note that the force $F(x)$ depends on the position x of motors and $v(F)$ is the **mean velocity** of n motors. The velocity v_0 is the velocity of a single motor without cargo which is 1 $\mu m/s$ for kinesin I. One should note that the motors can pass through the wall at $x = 0$ and walk on. In this case the process corresponds to flattening (or stretching) of a buckled filament. The maximal flattening is taken to occur at $x = -L$. So the last restriction of our model reads

$$-L \leqslant x \leqslant L \ . \tag{5.10}$$

After the motors reach the position $x = -L$ the motors stop since we restrict that the free end of cargo filament is fixed at $x = 0$. In this case there would be a strong backwards force since the filament is inextensible and the motors stop. In fact, the motors stop even before $x = -L$ since there is always a bent with a large curvature, see b) in Fig. 5.6.

In our considerations we start with n_0 motors linking the immobilized filament and the cargo filament at time $t = 0$. Once the movement starts the motors can unbind from the filament according to the Bell theory or bind to it with rate π. For the purpose of simplicity we always start with all motors in the system n_{tot} bound to the filaments, i.e., $n_0 = n_{tot}$. In this case the first process is the unbinding.

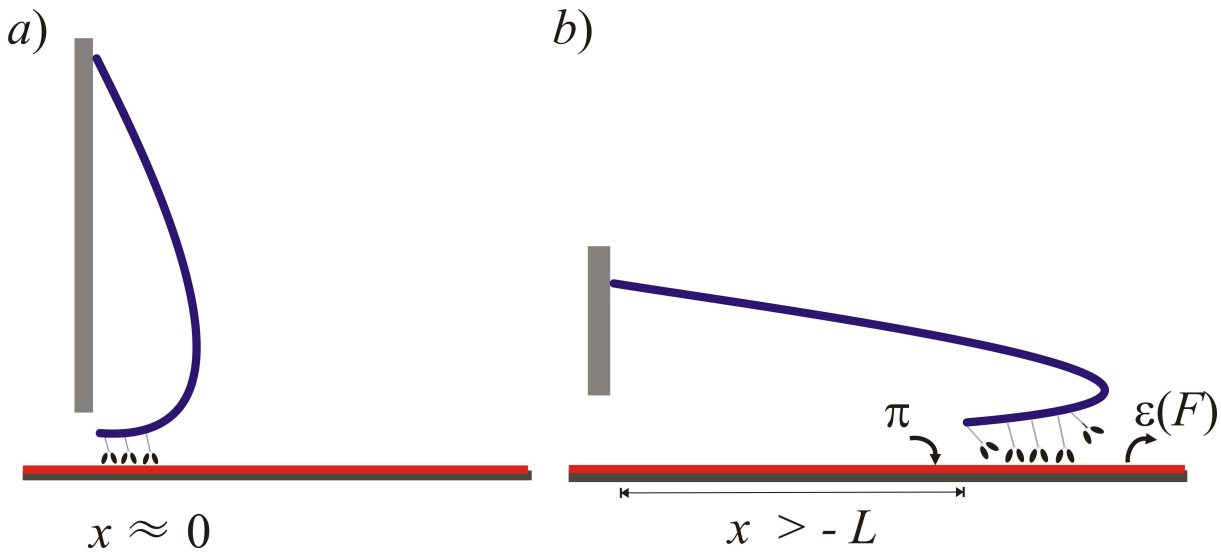

Figure 5.6: Buckled configurations of the cargo filament after the motors "passed through" the wall. *a*) The motor bunch is near $x = 0$ but at negative x. *b*) The motor bunch is near $x = -L$, i.e., at the minimal position it can reach according to the restriction (5.10).

Since we have a bunch of motors which share the load, see (5.5), we have to rewrite the Bell equation (5.2) as follows

$$\epsilon_n(F) = \epsilon(n, F) = n\epsilon_0 \exp\left(\frac{F(x)}{nF_d}\right) \ , \tag{5.11}$$

where the force $F(x)$ is the force from the force-extension relation (5.8), F_d is the detachment force for a single motor and n denotes the number of bound (i.e., linking) motors. The binding rate is given by

$$\pi_n = \pi(n) = \pi_0 \left(n_{tot} - n\right) \ . \tag{5.12}$$

Since the bond rupture is a discrete process, the stochastic dynamics of the system presented in Fig. 5.5 can be described by the one-step master equation [61, 70]

$$\partial_t p_n(t) = -\epsilon_n p_n + \epsilon_{n+1} p_{n+1} - \pi_n p_n + \pi_{n-1} p_{n-1} \ , \tag{5.13}$$

where $p_n(t)$ is the probability that n motors link the immobilized and the cargo filament and $n \geqslant 1$. Here, the ϵ_n and π_n are the reverse and forward rates between the possible states n ($0 \leqslant n \leqslant n_{tot}$) and given by (5.11) and (5.12), respectively. The rate ϵ_n is the transition rate from a state with n attached motors to a state with $n-1$ attached motors by unbinding and π_n the transition rate from a state with n attached motors to a state with $n+1$ attached motors by binding.

5.4 Buckling under the action of a single molecular motor

First, we focus our investigations on a system with only one motor, i.e., $n_{tot} = n_0 = 1$. Since we assume here that already one motor can buckle the filament, we investigate a system with the cargo filament of the contour length $L = 25\ \mu m$, i.e., the critical force $F_{c,0} = 0.09\ pN$ is small. We establish the position-time relation for the single motor. Further, we use the parameters for a kinesin I motor on a microtubule so all the values are known from experiments, see Table 5.1.

The initial position of the motor is assumed to be $x = L$, i.e., the cargo filament is "catched" by the motor at the end. Now, the motor starts to walk along the immobilized filament and pushes the cargo filament against the wall, what leads to buckling of the cargo filament. The force acting on the motor corresponds then to the compressional force acting on the filament as presented in previous sections. The projected length $\langle L_{||} \rangle$ denotes then the position x of the motor on the immobilized filament. Simulation data for projected length as a function of reduced force can be simply rewritten giving the dependence of reduced force $F/F_{c,0}$ on position (projected length) $x \equiv L_{||}$.

In case of a single motor in the system and no motor binding ($n_{tot} = n_0 = 1$ and $\pi = 0$) we can check our approximations by investigating three different cases of establishing the distance x as a function of time t. First, we use the linear approximation for the projected length $L_{||}$ as a function of applied force $F(x)$ and rewrite this to get the expression for the force $F(x)$ as a function of the distance x. Note, that the force applied on the motor increases when the distance x decreases. In this case the position of the motor can be calculated analytically by integrating (5.9) and reads

$$x(t) = L\left(3 - \frac{2F_s}{F_{c,0}}\right) + 2L\left(\frac{F_s}{F_{c,0}} - 1\right)\exp\left(-\frac{F_{c,0}v_0}{2F_sL}\ t\right). \tag{5.14}$$

This solution for the reduced distance x/L as a function of dimensionless time $\bar{t} \equiv t\ v_0/L$ is plotted in Fig. 5.7 *a*) for four different values of parameter $F_{c,0}/F_s = 0.1$ (red), 0.3 (green), 0.6 (blue), 0.7 (black). The dashed gray line corresponds to $x = 0$, i.e., when the motor reaches the wall. After that the motor passes the wall and the cargo filament creates a loop. In this case we observe stretching of the cargo filament, compare Chapter 2.

In the second approach we use the full analytical expression for buckling given by the elliptic integrals, see Chapter 2. In order to get the force as a function of position x we discretize this expression and solve the equation of motion numerically [110].

Finally, we can also introduce our simulation results from Chapter 4 for the mean projected length $\langle L_{||}(F) \rangle$. The numerical integration result is plotted in Fig. 5.7 *b*) - *d*) for four different values of parameter $F_{c,0}/F_s = 0.1$ (red), 0.3 (green), 0.6 (blue), 0.7 (black). The dashed gray line corresponds to $x = 0$. Here, we present results for $L_p/L = 1$ (*b*), $L_p/L = 10$ (*c*), $L_p/L = 100$ (*d*) and for parameter $F_{c,0}/F_s = 0.1$ (red), 0.3 (green), 0.6 (blue), 0.7 (black). We used simulation results for two (circles) and three (triangles) spatial dimensions. Notice that in case for three spatial dimensions (triangles in *b*) - *d*) in Fig. 5.7) the starting position at $t = 0$ for $L_p/L = 1$ is smaller than for the case of two dimensions. The origin of this behavior is the existence of the third dimension in which the cargo filament can fluctuate, compare Chapter 4.

In Fig. 5.8 we compare these three approaches and present the results for four different values of parameter $F_{c,0}/F_s$, *a*) $F_{c,0}/F_s = 0.9$, *b*) $F_{c,0}/F_s = 0.5$, *c*) $F_{c,0}/F_s = 0.3$ and *d*) $F_{c,0}/F_s = 0.1$. We choose the stiffness parameter to be $L_p/L = 100$ which corresponds to microtubules and used the simulation results in two spatial dimensions. Here, the solid line corresponds to the solution (5.14) using the linear approximation (5.7), red triangles correspond to analysis with use of simulation data for $1 - \langle L_{||} \rangle / L$ as function of $F/F_{c,0}$ from Chapter 4 and blue circles correspond to numerical integration using full $T = 0$ solution (2.21) for $1 - L_{||}/L$ as function of $F/F_{c,0}$ given by elliptic integrals, see Chapter 2.

Note, that for $F_{c,0}/F_s = 0.9$ presented in *a*) the quality of data presented by triangles (using simulation data) is not good and the approximation should be treated carefully.

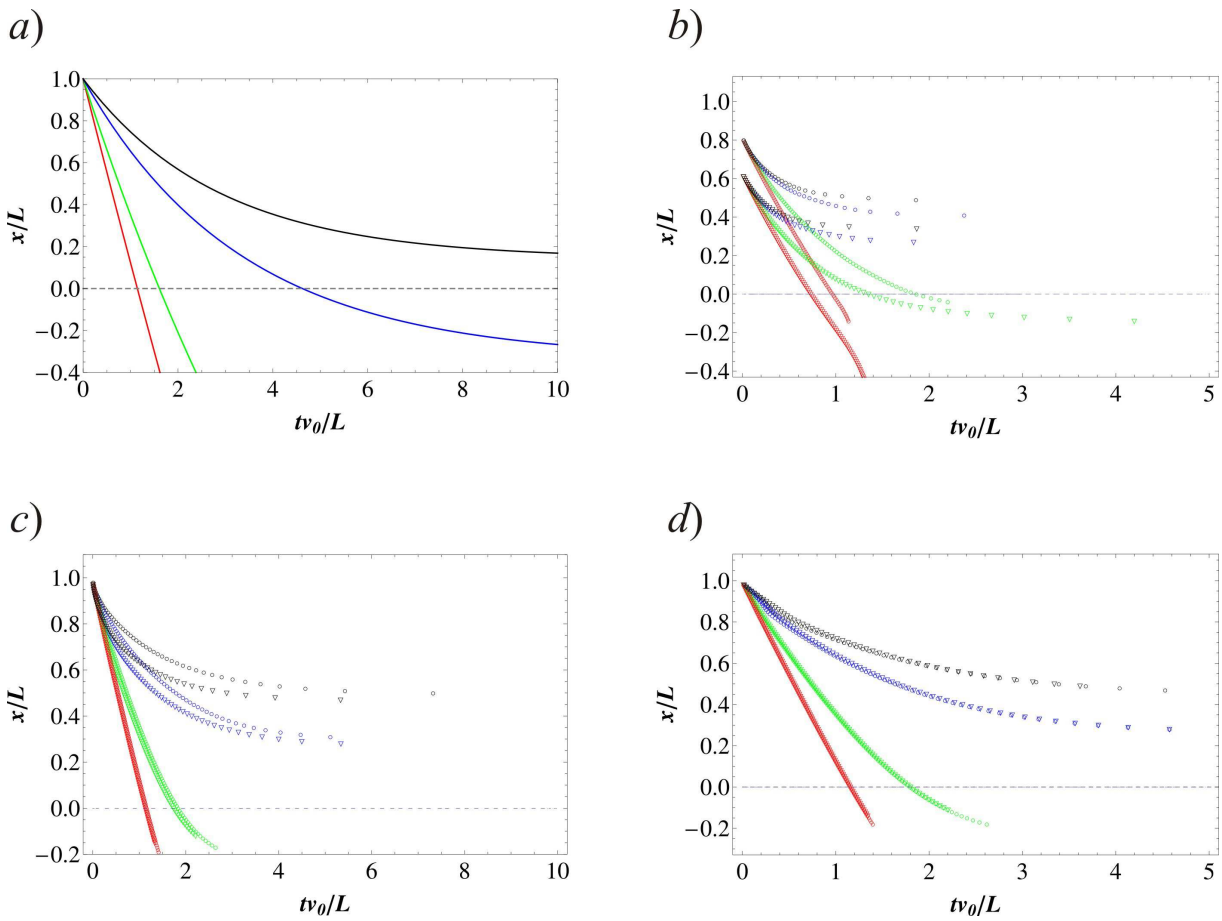

Figure 5.7: Reduced position of a single molecular motor as function of the reduced time $\bar{t}$. *a*) Analytical solution (5.14). *b*) - *d*) Numerical integration results using the simulation results for $F(\langle L_{||} \rangle)$ from Chapter 4 for $L_p/L = 1$ (*b*), $L_p/L = 10$ (*c*), $L_p/L = 100$ (*d*). Results for parameter $F_{c,0}/F_s = 0.1$ (red), 0.3 (green), 0.6 (blue), 0.7 (black). Here, we used simulation results for two ($\circ$) and three ($\triangledown$) spatial dimensions, see Chapter 4.

However, for the case of small critical force, presented in *d*), all three approaches are in good agreement with each other in the short times regime, i.e., $0 < t < 5$ seconds. In this time the motor reaches, and even passes, the wall. Also note, that changing the boundary conditions of the cargo filament one changes only the critical force $F_{c,0}$. Therefore, the parameter $F_{c,0}/F_s$ can be changed by changing the boundary conditions.

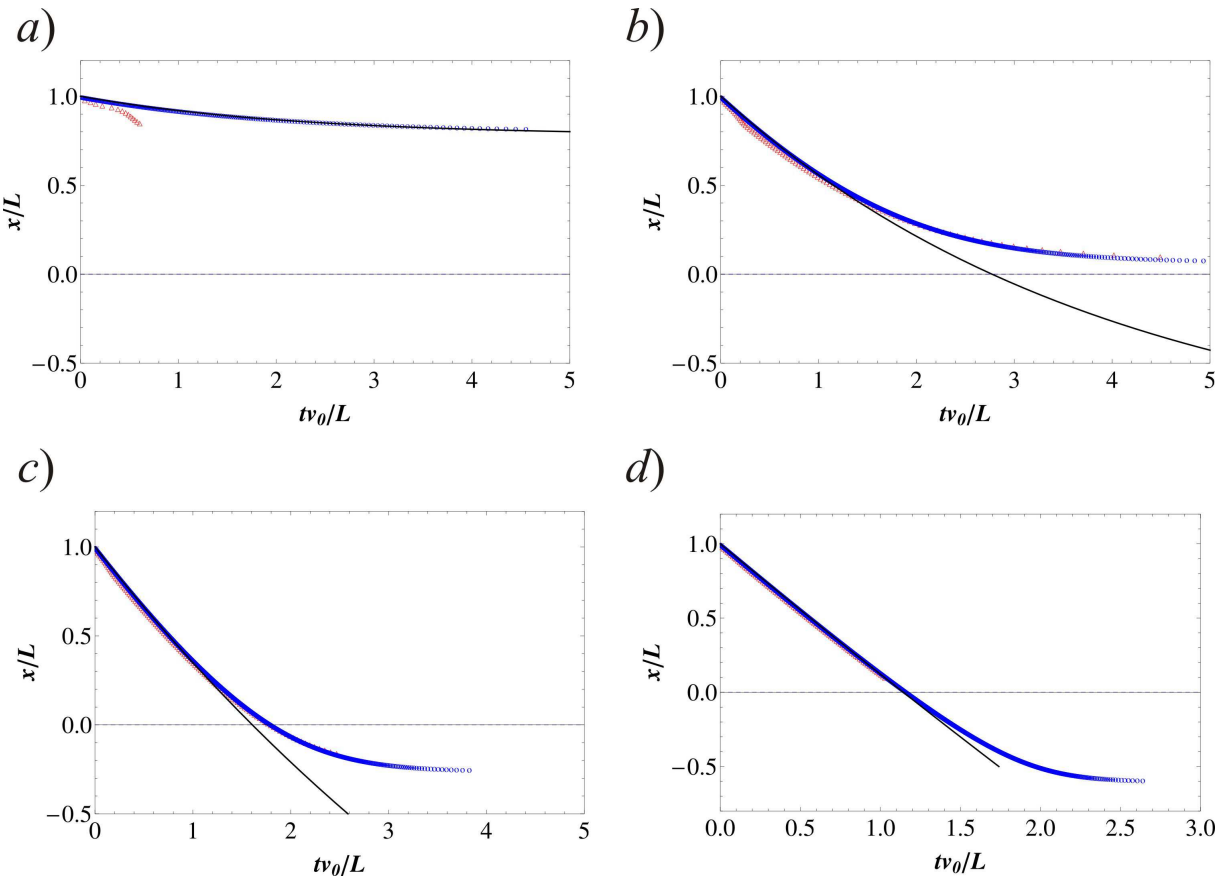

Figure 5.8: Position-time relations for a single molecular motor in case of cargo filament with stiffness parameter $L_p/L = 100$. Comparison of three approaches (see text for details) for four different values of parameter $F_{c,0}/F_s$ *a*) $F_{c,0}/F_s = 0.9$, *b*) 0.5, *c*) 0.3 and *d*) 0.1. The solid line corresponds to the solution (5.14) using the linear approximation (5.7), red triangles correspond to analysis with use of simulation data for $1 - \langle L_{||} \rangle / L$ as function of $F/F_{c,0}$ from Chapter 4 and blue circles correspond to numerical integration using full $T = 0$ solution (2.21) for $1 - L_{||}/L$ as function of $F/F_{c,0}$, see Chapter 2.

The results presented in *a*) - *d*) in Fig. 5.8 show that the linear approximation for the force-extension relation for buckling at $T = 0$ is a good approximation of buckling under the action of molecular motors in the short times regime. This is also the simplest case of the load force dependent on the position. In next sections of this work we will use this linear approximation for the systems with $n > 1$ molecular motors.

5.5 "Semi"-stochastic model for buckling under the action of bunch of molecular motors

In the previous section we showed that our assumptions made for the model are good in the short times regime in case of a single motor. Now, we will introduce a group of molecular motors of the same type which are walking along the immobilized filament in the same direction and which can unbind and rebind.

In this section we solve numerically the stochastic equation (5.13) for the probability $p_n(t)$ that n motors link two filaments at time t [110]. In general, the probability $p_n(t)$ depends also on the position $x(t)$ of motors. Since we do not consider any fluctuations in the distance between motors and treat the variable x as deterministic, see Section 5.1.4, the probability $p_n(t)$ depends only on n and t. We call this model "semi"-stochastic because only the processes of unbinding and rebinding of motors are stochastic and the position of motors is deterministic and given by the velocity-force relation (5.9), which we average over n in a mean field approximation. We also assume here that the distance between the motors is constant in time. Then, the bunch of motors in our model can be considered as one giant motor complex which exerts the force equal to the force exerted by n motors. We restrict our considerations to $n_0 = n_{tot}$ motors, i.e., all motors are bound at time $t = 0$ and we investigate systems with $n_{tot} = 5$ motors. We consider two different contour lengths of the cargo filament, $L = 25\ \mu m$ and $L = 5\ \mu m$. This corresponds to two values of the critical force, $F_{c,0} = 0.09\ pN$ and $F_{c,0} = 2.2\ pN$, respectively. Note, that in case of $L = 25\ \mu m$ the critical force is two orders of magnitude smaller than the stall force F_s for kinesin I. For short filaments the critical force increases according to $F_{c,0} \propto 1/L^2$.

5.5.1 Probability $p(t)$ for a single molecular motor

In the case of a single motor initially attached to the immobilized filament, i.e., $n_{tot} = n_0 = 1$ and assuming that there is no rebinding in the system ($\pi = 0$) one can rewrite the equation (5.13) as follows

$$\partial_t p(t) = -\epsilon(F) p(t), \tag{5.15}$$

where $p(t)$ is the probability that a single motor links both filaments and $\epsilon(F)$ is given by (5.11) with $n = 1$. We can integrate the equation (5.15)

$$\int_1^p \frac{d\tilde{p}}{\tilde{p}} = -\int_0^t dt' \epsilon_0 \mathrm{e}^{F(x)/F_d} \tag{5.16}$$

with

$$F(x) = F_s + (F_{c,0} - F_s) \exp\left(-\frac{F_{c,0} v_0}{2 F_s L}\ t\right), \tag{5.17}$$

where we use (5.7) and (5.14). The solution of (5.16) is given by

$$p(t) = \exp\left[-B\left(Ei[-A] - Ei\left[-A\mathrm{e}^{-\frac{F_{c,0} v_0}{2F_s L}\ t}\right]\right)\right], \tag{5.18}$$

where $Ei[x]$ denotes the exponential integral function of x [31] and

$$A = \frac{F_s - F_{c,0}}{F_d}, \tag{5.19}$$

$$B = \epsilon_0 \frac{2LF_s}{F_{c,0} v_0}\ \mathrm{e}^{F_s/F_d}. \tag{5.20}$$

Therefore, knowing all the parameters for the system (5.18) gives the probability $p(t)$ that a single motor links the firmly attached and the cargo filaments as function of time t.

5.5.2 Probability $p_n(t)$ for a bunch of molecular motors

In this Section we solve numerically [110] the master equation for probability $p_n(t)$ that n motors are bound at time t, see (5.13). In order to solve this equation we use the mean field approximation in the velocity-force relation (5.9) by taking the average $\langle 1/n \rangle$ of bound motors in each integration of the equation of motion, i.e.,

$$v(t) = \dot{x} = -v_0 \left(1 - \left\langle \frac{1}{n} \right\rangle \frac{F(x)}{F_s} \right) , \tag{5.21}$$

where we use (5.8) for the force $F(x)$, (5.11) and (5.12).

In Fig. 5.9 *a*) and *b*) we present the probabilities $p_n(t)$ that n motors are bound to the filament at time t for the case when there is no rebinding in the system, i.e., $\pi = 0$ and for $L = 25\ \mu m$ and $L = 5\ \mu m$, respectively. The solid lines in the figure correspond to the probabilities $p_5(t)$ (red), $p_4(t)$ (green), $p_3(t)$ (blue), $p_2(t)$ (pink), $p_1(t)$ (cyan). The black solid line represents the probability $p_0(5)$ that the cargo and the immobilized filament are not linked by any motor. In

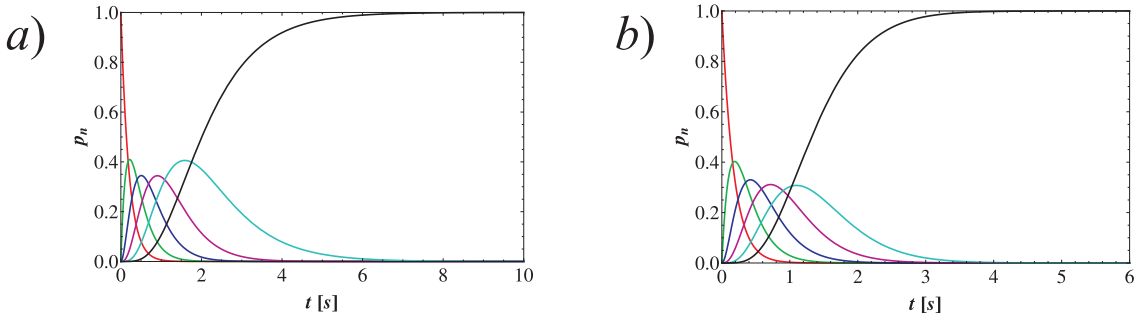

Figure 5.9: The numerical result for $p_n(t)$ established from (5.13) using (5.21) with (5.8) and (5.11) with no rebinding in the system, i.e., $\pi = 0$. *a*) the result for the cargo filament of contour length $L = 25\ \mu m$ and *b*) for the cargo filament of contour length $L = 5\ \mu m$. The solid lines correspond to the probabilities $p_5(t)$ (red), $p_4(t)$ (green), $p_3(t)$ (blue), $p_2(t)$ (pink), $p_1(t)$ (cyan) and $p_0(5)$ (black).

Fig. 5.10 we present the probability $p_n(t)$ that n motors are bound to the filament at time t for the case when there is rebinding in the system, i.e., $\pi_0 = 5s^{-1}$ where the colors are the same as for the case with $\pi_0 = 0$. One can see, that in case of long cargo filaments the bunch of motors links the filaments for much longer time, however the number of linking motors changes. In Fig. 5.11 *a*) and *b*) we present the probability $p_n(t)$ that n motors are bound to the filament at time t for the case when there is rebinding in the system, i.e., $\pi_0 = 5s^{-1}$ for $L = 25\ \mu m$ and $L = 5\ \mu m$, respectively.

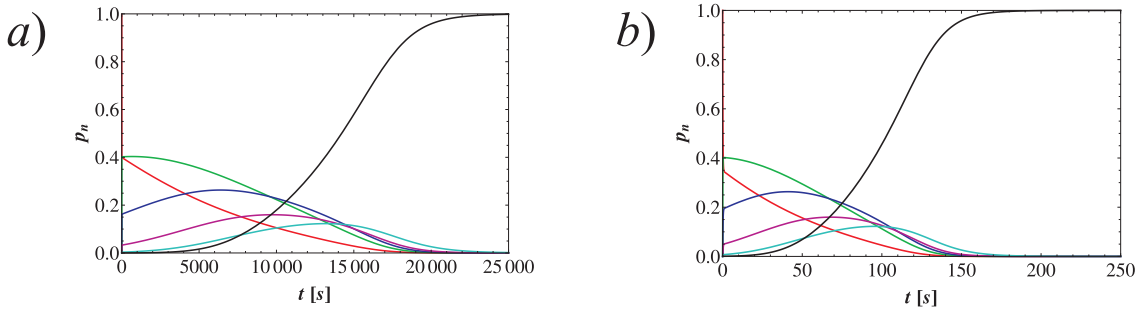

Figure 5.10: The numerical result for $p_n(t)$ established from (5.13) using (5.21) with (5.8) and (5.11) and with rebinding in the system $\pi_0 = 5\ s^{-1}$, see (5.12). *a*) the result for the cargo filament of contour length $L = 25\ \mu m$ and *b*) for the cargo filament of contour length $L = 5\ \mu m$. The solid lines correspond to the probabilities $p_5(t)$ (red), $p_4(t)$ (green), $p_3(t)$ (blue), $p_2(t)$ (pink), $p_1(t)$ (cyan) and $p_0(5)$ (black).

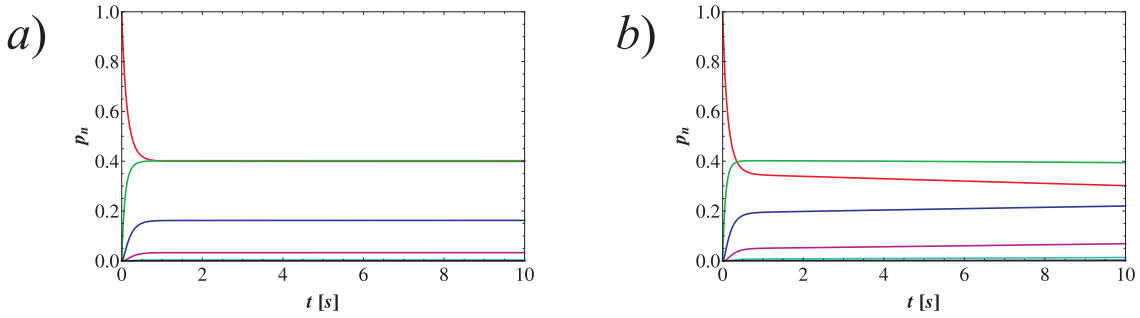

Figure 5.11: The numerical result for $p_n(t)$ established from (5.13) using (5.21) with (5.8) and (5.11) with rebinding in the system $\pi_0 = 5s^{-1}$ (see (5.12)) in short times regime. *a*) the result for the cargo filament of contour length $L = 25\ \mu m$ and *b*) for the cargo filament of contour length $L = 5\ \mu m$. The solid lines correspond to the probabilities $p_5(t)$ (red), $p_4(t)$ (green), $p_3(t)$ (blue), $p_2(t)$ (pink), $p_1(t)$ (cyan) and $p_0(5)$ (black).

By numerical integration of the velocity $v(t)$ we can also determine the position $x(t)$ of the clamped end of the cargo filament. We plot $x(t)$ for $L = 25\ \mu m$ and $L = 5\ \mu m$ for $n_0 = 5$ in Fig. 5.12 in *a*) and *b*), respectively. We present here the numerical result for $x(t)$ established from (5.13) for $\pi_0 = 0$ (red dashed lines) and $\pi_0 = 5s^{-1}$ (blue dashed lines) in short times regime. In case of $L = 25\ \mu m$ we observe the perfect overlap of both functions. In *b*) we present the very short times regime. Here, for $\pi_0 = 0$ the motors need longer to get to $x = 3.6\ \mu m$ since the motors can only unbind. For $L = 5\ \mu m$ and $\pi = 0$ at time $t \approx 1.5\ s$ all n_0 motors are, however, unbound, see next section. Therefore, the red curve for $t > 1.5$ represents only the numerical solution and not the physical situation. One can see that for long filaments ($L = 25\ \mu m$) there is no significant difference in $x(t)$ during the first seconds for $\pi_0 = 0$ and $\pi_0 = 5s^{-1}$. This means that for long filaments the load force does not influence the motors and the velocity of the bunch of motors is independent on the binding rate π in short times regime. For short filaments, however, the positive binding rate π causes an *increase* of the velocity of the bunch of motors for times smaller than the mean first passage time τ, see the next section.

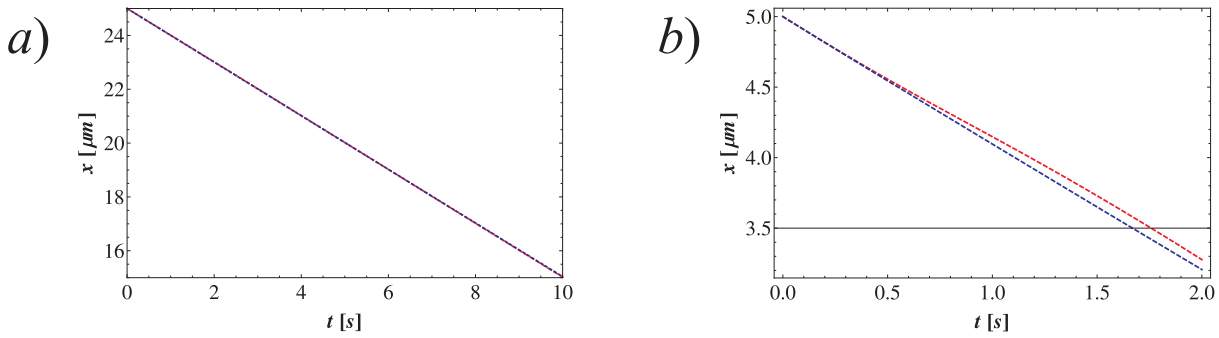

Figure 5.12: The numerical result for $x(t)$ determined from (5.13) using (5.21) with (5.8) and (5.12) for $\pi = 0$ (red) and $\pi_0 = 5s^{-1}$ (blue) in short times regime. *a)* Result for the cargo filament of contour length $L = 25\ \mu m$. Note the perfect overlap of both functions. *b)* Result for the cargo filament of contour length $L = 5\ \mu m$. Note that in case of $\pi = 0$ the motors need longer to get to $x = 3.5\ \mu m$ since the motors can only unbind. For $L = 5\ \mu m$ and $\pi = 0$ at time $t \approx 1.5\ s$ all n_0 motors are unbound, see Section 5.5.3.

5.5.3 Mean first passage time

It is of interest to know how long the cargo filament stays buckled under the action of the bunch of molecular motors. The quantity which describes this time is the mean first passage time τ which gives the time needed to unbind all bound motors, i.e., the time needed for a transition from state with n_0 bound motors at $t = 0$ to a state with $n = 0$ bound motors. This corresponds to the transition from the buckled to the unbuckled state of the cargo filament [70, 52, 111]. As long as the motors link two filaments and the force exerted by them is sufficient, the cargo filament stays buckled and the bent gets larger with time t since the effective force is increasing when the projected length $L_{||}$ is decreasing. The motors on the other hand unbind from the immobilized filament with a rate given by (5.2) which is increasing with force.

We look for the time when the last motor unbinds for the first time and the cargo filament returns to its straight (unbuckled) configuration. We consider the probability $p_n(t)$ as the probability that exactly n motors are bound at time t and start with n_0 motors bound at $t = 0$. Now, we look for the escape probability $-\partial_t p_n(t)$ from the state with n motors bound to the state with $n-1$ or $n+1$ bound motors with $1 \leqslant n \leqslant n_0$. Then, the mean first passage time τ_n for leaving the state with n bound motors reads

$$\tau_n = -\int_0^\infty dt\ t\ \partial_t p_n(t) = \int_0^\infty dt p_n(t), \tag{5.22}$$

with $0 < n < n_{tot}$ where we integrated by parts. For calculating the total mean first passage time τ needed to unbind all $n_0 \equiv n(t = 0)$ motors we calculate all the mean first passage times τ_n for $1 \leqslant n \leqslant n_0$ and finally we sum them all over n, i.e.,

$$\tau[L, \pi] = \sum_{n=1}^{n_0} \tau_n, \tag{5.23}$$

where L and π_0 in the brackets on the left hand side denote the contour length of cargo filament and the binding rate determined by π_0, respectively. This lets us calculate the quantity τ which could be observed in an experiment. In case of a single molecular motor one can numerically calculate the mean first passage time τ using the analytical solution (5.18) for $p(t)$.

Now we can calculate the values of τ for different cases of contour length L and rebinding rate π using the parameters for kinesin I and microtubules, see Table 5.1. For $n_0 = 5$ motors and cargo filament of contour length $L = 25\ \mu m$ and $\pi = 0$ we get

$$\tau[L = 25\ \mu m, \pi = 0] = 2.24\ s. \tag{5.24}$$

That means, that in case of no binding, $\pi = 0$, and microtubule with $L = 25\ \mu m$ as cargo filament all $n_0 = 5$ kinesin I motors bound at time $t = 0$ detach after 2.24 seconds. If there is rebinding in the system, one gets

$$\tau[L = 25\ \mu m, \pi_0 = 5s^{-1}] \approx 13825\ s. \tag{5.25}$$

One can clearly see that a positive binding in the system causes a significant *increase* of the mean first passage time τ. The binding of new motors during buckling of the cargo filament increases the force the bunch of motors can exert so the motors can buckle the cargo filament more easily. However, the mean first passage time (5.25) is very large and corresponds to the situation when a bunch of motors passes through the wall, walks till it reaches the position $x = -L$, i.e., the motors stretch the looped cargo filament, and after that they pull the cargo filament behind them. In this case the load force gets very large since the filament is not extensible, see (5.10) and Fig. 5.6. Therefore, for positive π we can consider only short times regime within our approximation.

In Fig. 5.13 we plot the following relations for a binding rate $\pi = 0$: *a*) mean first passage time τ as function of contour length L. One can see that the mean first passage time τ increases with increasing contour length L of the cargo filaments. The reason for this behavior is the decrease of the critical force for the cargo filament, i.e., the motors can buckle the filament more easily. *b*) Position $x(\tau)$ of the last motor at its detachment time as function of contour length L. This position is always positive , i.e., the last motor unbinds before the bunch of motors reached the wall at $x = 0$ for all contour lengths L. We define F_τ as the value of the force $F(x)$ at the position $x(t = \tau)$, i.e.,

$$F_\tau \equiv F\left(x(t = \tau)\right). \tag{5.26}$$

In *c*) we plot the force F_τ for different mean first passage times τ. The times τ can be changed by changing the cargo filament length L. Therefore, the force F_τ is dependent on the contour length L, i.e., $F_\tau = F_\tau(L)$. Another possibility to change the mean first passage time is the change of number of motors n. However, in this work we only consider the case $n_0 = n_{tot} = 5$. In *d*) we present the numerical value of the force F_τ as function of contour length L. One can see, that for long filaments the value of $F_\tau(L)$ as function of L approaches zero. For an infinitely long cargo filament the critical force vanishes and the force F in (5.7) approaches zero. Hence, every motor unbinds from the filament like in case where there is no cargo, i.e., with rate ϵ_0. The values for $F_{c,0}$ correspond to a cargo filament with one clamped and one free end. In case of $L = 1\ \mu m$ the critical force is $F_{c,0} = 54.28\ pN$ and does not fulfill the condition (5.6). Hence, the values of all observables cannot be discussed in terms of our model. For $L = 3\ \mu m$ we get $F_{c,0} = 6.03\ pN$, i.e., $F_{c,0} \simeq F_s$ and the condition (5.6) is fulfilled. The cargo filament of contour length $L = 3\ \mu m$ is the shortest filament we can treat in terms of the model, unless we change the boundary conditions.

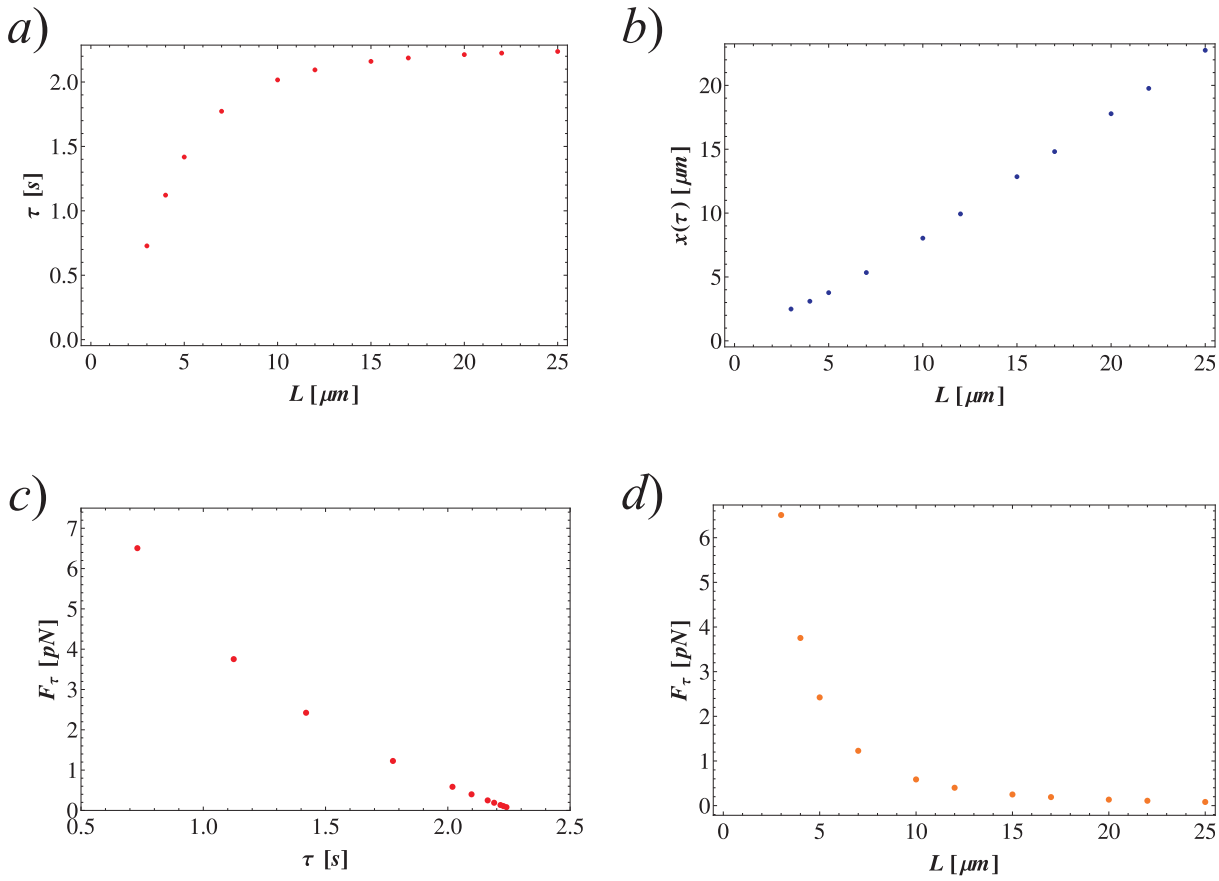

Figure 5.13: Numerical analysis of buckling under the action of molecular motors in case of $\pi = 0$ for different contour lengths of the cargo filament. *a*) Mean first passage time τ as function of contour length L. *b*) Position of the last motor at its detachment time as function of contour length L. *c*) Force $F_\tau = F(x(t = \tau))$ plotted for different mean first passage times τ. The times τ can be changed by changing the length L. *d*) Numerical values F_τ of the force at mean first passage time, i.e., the maximal force when the last motor unbinds, as function of contour length L.

Now, we calculate the mean first passage time for cargo filament with $L = 5\ \mu m$ and $\pi = 0$ and get

$$\tau[L = 5\ \mu m, \pi = 0] = 1.42\ s. \tag{5.27}$$

For $L = 5\ \mu m$ and positive binding rate $\pi_0 = 5s^{-1}$ we get

$$\tau[L = 5\ \mu m, \pi_0 = 5s^{-1}] = 100.63\ s. \tag{5.28}$$

Again, because of rebinding in the system the mean first passage time becomes very large. Note, that also in the case of $L = 5\ \mu m$ in the presence of rebinding the model is restricted to short times regime when $x > -L$.

In Fig. 5.14 we plot the same relations as in Fig. 5.13 for the binding rate $\pi_0 = 5s^{-1}$. Note, that while the position $x(\tau)$ in Fig. 5.13 *b*) is positive for all contour lengths, the position $x(\tau)$ in Fig. 5.14 *b*) becomes negative with increasing L. The large negative values for $x(\tau)$ in *b*) correspond to large distances behind the wall. Thus, the positive rebinding allows the motors to walk much further and longer and the motors can pass the position $x = 0$. This means that the cargo filament is being pulled already but the force $F(x)$ is still given by (5.7). This case is an artefact of our model, since we can only consider the case $L > x > -L$. Furthermore, already for the cargo filament of contour length $L = 3\ \mu m$ the position of last motor at $t = \tau$ is $x = -4.66\ \mu m$. That means that $n_0 = 5$ kinesin I motors are enough to buckle the cargo filament with one free end, to reach the wall and finally to pull the looped filament till it gets

straight. This phenomenon occurs only if there is binding in the system given by the binding rate π_n. Finally, in *c*) and *d*) in Fig. 5.14 we observe that in case of $\pi_0 = 5s^{-1}$ the force F_τ

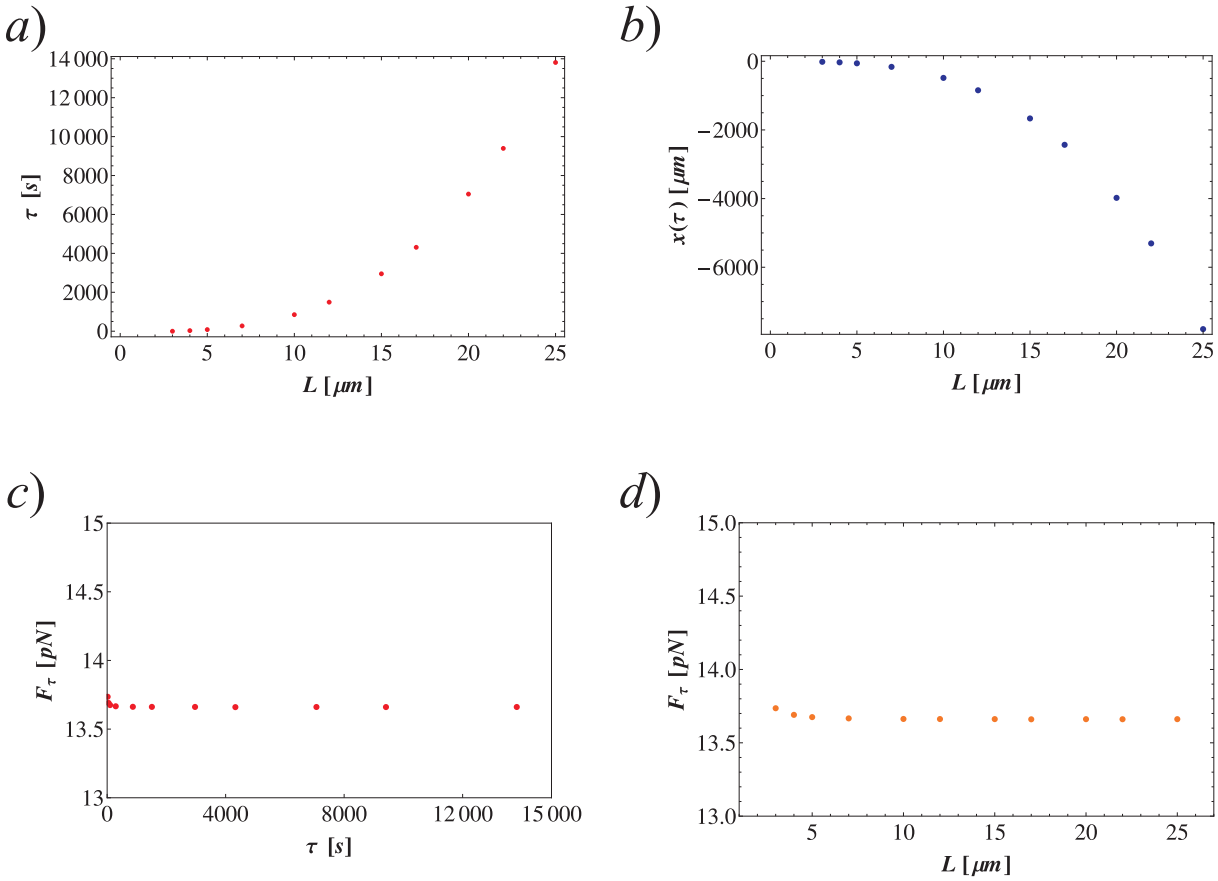

Figure 5.14: Numerical analysis of buckling under the action of molecular motors in case of $\pi_0 = 5s^{-1}$ for different contour lengths of cargo filament. *a*) Mean first passage time τ as function of contour length L. *b*) Position of the last motor at its detachment time as function of contour length L. *c*) Force $F_\tau = F(x(t = \tau))$ plotted for different mean first passage times τ. The times τ can be changed by changing the length L. *d*) Numerical values F_τ of the force at mean first passage time, i.e., the maximal force when the last motor unbinds, as function of contour length L. The first point in *c*) and *d*) corresponds to $L = 3\ \mu m$ when $F_{c,0} = 6.03\ pN$, i.e., $F_{c,0} \simeq F_s$, so the condition (5.6) is fulfilled. The values for $F_{c,0}$ correspond to a cargo filament with one clamped and one free end.

becomes constant and does not depend on L for large L. The detachment force for a giant motor complex made up from n bound motors is given by $F_{d,n} = n\ F_d$. Therefore, when the force becomes $F = F_{d,n}$ all bound motors have to unbind and the value of $F_{d,n}$ does not depend on L. In the next section we will introduce a critical force for destabilization of the cluster made by linking motors in terms of the deterministic equation for $N = \langle n \rangle$, i.e., the mean number of linking (bound) motors.

5.5.4 Critical force $\tilde{F}_{crit}$ for destabilization of bound motors.

The force destabilizes the linked filament configuration, while rebinding stabilizes it. It has been shown by Bell that in the framework of the deterministic equation for the mean numbers of linking motors,

$$\frac{d\langle n\rangle}{dt} = \frac{dN}{dt} = -\langle \epsilon_n(F)\rangle + \langle \pi_n\rangle, \tag{5.29}$$

the cluster remains stable up to a critical force $\tilde{F}_{crit}$ [69, 112]. In equilibrium we have

$$N_{eq} \mathrm{e}^{\frac{F}{F_d N_{eq}}} = \gamma \left(n_{tot} - N_{eq}\right), \tag{5.30}$$

where $\gamma \equiv \pi_0/\epsilon_0$ is the dimensionless rebinding rate (given by the ration of binding and unbinding rates) and N_{eq} is the equilibrium state $N_{eq} = \gamma n_{tot}/(1+\gamma)$ of closed links with the initial condition $N(0) = n_{tot}$, i.e., with all motors bound at the beginning. N_{eq} increases linearly with the rebinding rate constant γ from $N_{eq} = 0$ for $\gamma = 0$ and saturates at n_{tot} for $\gamma > 1$. In the deterministic description, the lifetime of the cluster (linked filaments) is infinite, because the completely dissociated state $N \equiv \langle n\rangle = 0$ (the average number of closed links between two filaments) is never reached.

Equation (5.30) applies to a model when the force F is *independent* on the position x. In case of the model for buckling under the action of molecular motors, the force $F = F(x)$ is always x-dependent after buckling. Hence, we use (5.30) only as an approximation for small forces $F(x)$.

At small force F, eq. (5.30) has two roots, with the larger one corresponding to a stable equilibrium. As force increases, a saddle-node bifurcation occurs. Above the critical force $\tilde{F}_{crit}$, no roots exist and the linked configuration becomes unstable. Exactly at critical loading, the two roots collapse and the slopes of the two terms become equal. This gives an additional equation

$$\mathrm{e}^{\tilde{F}_{crit}/(F_d N_c)} \left(1 - \frac{\tilde{F}_{crit}}{F_d N_c}\right) = -\gamma, \tag{5.31}$$

where N_c denotes the number of closed links. These two equations, (5.30) and (5.31), allow to determine the critical values for force and the cluster size:

$$\tilde{F}_{crit} = F_d \; n_{tot} \; \mathrm{pln}\left(\frac{\gamma}{\mathrm{e}}\right) \tag{5.32}$$

and

$$N_c = n_{tot} \; \frac{\mathrm{pln}\left(\frac{\gamma}{\mathrm{e}}\right)}{1 + \mathrm{pln}\left(\frac{\gamma}{\mathrm{e}}\right)}, \tag{5.33}$$

where the product logarithm $\mathrm{pln}(a)$ is defined as the solution x of $x\mathrm{e}^x = a$ [112]. For small forces, the unstable fixed point is very close to zero. This implies that the stable fixed point is an attractor for most initial conditions. Close to the critical force, the unstable fixed point is close to the stable one and only the initial conditions above N_c will reach the stable fixed point. Equations (5.32) and (5.33) scale in a trivial way with n_{tot}, but in a complicated way with γ. For $\gamma < 1$, we have $\tilde{F}_{crit} \approx F_d \; \gamma \; N_{tot}/\mathrm{e}$. Thus the critical force vanishes with γ, because the cluster always decays in the absence of rebinding. For $\gamma > 1$ and up to $\gamma \approx 100$, we have

$$\tilde{F}_{crit} \approx 0.5 \; n_{tot} \; F_d \; \ln \gamma. \tag{5.34}$$

This weak dependence on γ shows that the single bond force scale set by F_d also determines the force scale on which the linked filaments as a whole disintegrates. Note, that $\tilde{F}_{crit}$ is larger than the detachment force F_d. For $n_0 = 5$ with $\pi_0 = 5s^{-1}$ and $\epsilon_0 = 1s^{-1}$ we get

$$\tilde{F}_{crit} \approx 12 \; pN. \tag{5.35}$$

Therefore, when the load force gets larger than $\tilde{F}_{crit}$ the filaments get separated (i.e., all motors unbind) and the numerical analysis from this section has no physical meaning. The critical force $\tilde{F}_{crit}$ predicted in (5.35) is in good agreement with the force values at mean first passage time τ presented in *c*) and *d*) in Fig. 5.14.

5.5.5 Vanishing force analysis

In the absence of force the problem is equivalent to the unbinding of multiple beads which has been considered in Refs. [112, 113]. Therefore, the stochastic equation (5.13) can be solved analytically. In this case the reverse rates are linear in n and $\epsilon(0) = 0$ at $n = 0$. Using the generating functions approach [114] one can show that

$$p_n(t) = \binom{n_{tot}}{n} \frac{\left(\gamma + \mathrm{e}^{-(1+\gamma)\epsilon_0 t}\right)^n \left(1 - \mathrm{e}^{-(1+\gamma)\epsilon_0 t}\right)^{n_{tot}-n}}{\epsilon_0 (1+\gamma)^{n_{tot}}}. \tag{5.36}$$

In Fig. 5.15 we present the vanishing force solutions for $p_n(t)$ (5.36) as dashed lines together with the numerical results for $p_n(t)$ established from (5.13). The lines correspond to the probabilities $p_5(t)$ (red), $p_4(t)$ (green), $p_3(t)$ (blue), $p_2(t)$ (pink), $p_1(t)$ (cyan) and $p_0(5)$ (black). One can see that the probabilities found using these two methods are in very good agreement. This analytical

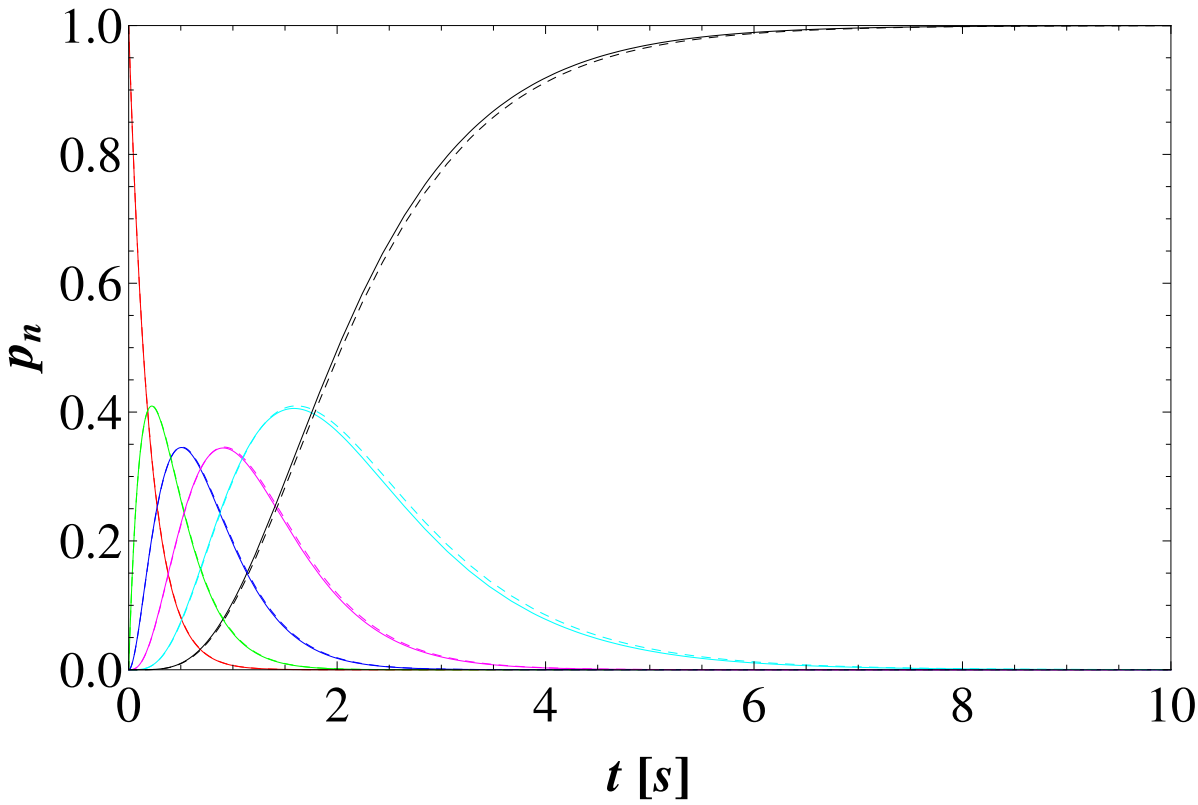

Figure 5.15: Probability $p_n(t)$ that n motors are bound to the filament at time t. We use the rebinding rate $\pi = 0$ and the cargo filament with the contour length $L = 25\ \mu m$. The numerical result for $p_n(t)$ established from (5.13) is presented by solid lines and the vanishing force solutions for $p_n(t)$ (5.36) (from [112]) are presented by dashed lines. The lines correspond to the probabilities $p_5(t)$ (red), $p_4(t)$ (green), $p_3(t)$ (blue), $p_2(t)$ (pink), $p_1(t)$ (cyan) and $p_0(5)$ (black).

result can also be used to establish the mean first passage time $\tau_{F=0}$ for unbinding all motors in the absence of the load force. Since the load force is close to zero for long filaments, when $F_{c,0}$ goes to zero, we expect that the vanishing force solution is a good approximation in this case. For $\pi = 0$ we get

$$\tau_{F=0}[L = 25\ \mu m, \pi = 0] = 2.28\ s, \tag{5.37}$$

where the index denotes the vanishing force case. Now, we can compare this mean first passage time to the mean first passage time for the positive force $F > 0$, $\tau_{num}[L = 25\ \mu m, \pi = 0] = 2.24$ seconds. One can see that these results are in very good agreement.

5.6 Mean Field approximation

A quantity of large interest is the average number of closed links between two filaments $N(t) = \langle n \rangle = \sum_{n=1}^{n_{tot}} n p_n(t)$. In this section we introduce the mean field approximation for our model and present the result for $N(t)$. From the master equation (5.13) one can derive [112, 113]

$$\frac{dN}{dt} = \sum_{n=1}^{n_{tot}} n \frac{dp_n}{dt} = -\langle \epsilon_n(F) \rangle + \langle \pi_n \rangle \ , \tag{5.38}$$

where $\pi_n = \pi(n) = \pi_0(n_{tot} - n)$ and $\epsilon_n(F) = \epsilon(n, F)$ is given by (5.11). If $\epsilon_n(F)$ was a linear function in n (in general, π_n has to be also linear in n which is fulfilled in the case of our model) the equation (5.38) would become an ordinary differential equation for N,

$$\frac{dN}{dt} = -\epsilon(\langle n \rangle, F) + \pi\left(\langle n \rangle\right) = -N\epsilon_0 \mathrm{e}^{F/(NF_d)} + \pi_0(n_{tot} - N) \ , \tag{5.39}$$

where the force $F = F(x)$ depends on the position x. We use here eq. (5.9) with $\langle n \rangle$, i.e.,

$$v = \dot{x} = -v_0 \left(1 - \frac{F(x)}{\langle n \rangle F_s}\right) = -v_0 \left(1 - \frac{F(x)}{N F_s}\right) \ . \tag{5.40}$$

Since the unbinding rate $\epsilon_n(F)$ has to be linear in n we consider only the cases when the load force F is very small what corresponds to a weak critical force $F_{c,0}$. Here, we consider the cargo filament of contour length $L = 25\ \mu m$ and $n_0 = 5$ motors bound at time $t = 0$. In this section we also consider only the case without rebinding, i.e., $\pi = 0$. The mean number of closed links $N(t)$ is presented in Fig. 5.16. We started with $n_0 = 5$ motors and observe the decay of $N(t)$.

We interpret the result as follows. All n_0 motors unbind when N becomes 0.5 (gray line in Fig. 5.16). The value of time t when $N = 0.5$ corresponds to the mean first passage time from the previous section and amounts $\tau_{\mathrm{mf}} \approx 2.2$ seconds. One can see that this result is in a very good agreement with $\tau = 2.24\ s$ calculated in section 5.5. Since the approximation (5.39) is valid only for $\epsilon_n(F)$ linear in n the mean field model works fine for small forces F. As we showed in the section 5.5 the force $F(x)$ becomes large for long times t when there is rebinding in the system.

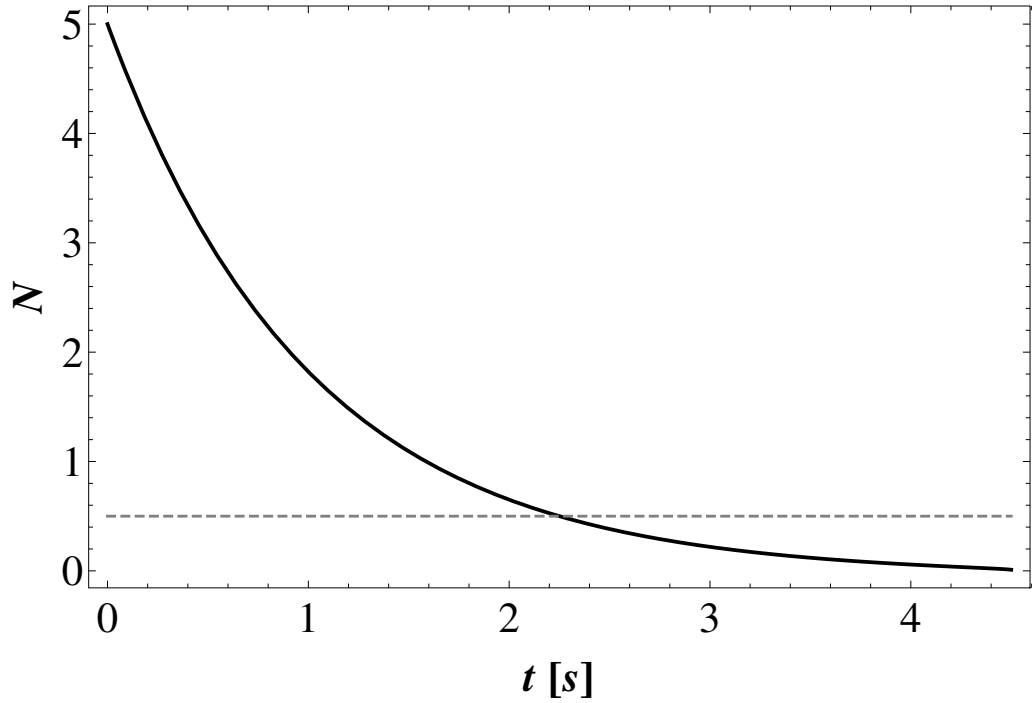

Figure 5.16: Mean number N of motors bound to the immobilized (firmly attached) filament as function of time t. The plot represents the numerical solution of mean field approximation (5.39) of our model of buckling of filaments under the action of molecular motors. The regime under the gray line $N = 0.5$ corresponds to the situation when motors are detached from the filament. The analysis is performed for a cargo filament of contour length $L = 25\ \mu m$ and $n_0 = 5$ motors bound at time $t = 0$ and without rebinding in the system, i.e., $\pi = 0$.

5.7 Simulation results of buckling under the action of molecular motors

Finally, we can also perform computer simulations where not only the unbinding and rebinding of motors are stochastic but also the stepping process of motors [115] in order to check our results from previous sections. In this section we present results of simulations for two cases of contour length, $L = 25\ \mu m$ and $L = 5\ \mu m$.

5.7.1 Simulation algorithm

The dynamics of the motors are given by a Markov process in continuous time on the one dimensional state space $n, 0 \leqslant n \leqslant n_{tot}$ of bound motors. The simulations are based on the usual Monte Carlo algorithm but in contrast to the more common case of MC simulations in equilibrium statistical mechanics [116], the Markov chain of states of the system is generated with the *true dynamics* of the system. The transition rates between the states of this Markov process are given by

$$\epsilon_n(x) = n\epsilon_0 \exp\left(F(x)/(nF_d)\right) \qquad \text{for the transition} \quad n \to n-1 \text{ for } n > 0, \tag{5.41}$$

$$\pi_n = \pi_0 \left(n_{tot} - n\right) \qquad \text{for the transition} \quad n \to n+1 \text{ for } n < n_{tot}\ . \tag{5.42}$$

Here, the force F is given by (5.8) with critical force $F_{c,0} = \pi^2\kappa/(4L^2)$. If the cargo is in the state of n bound motors it moves with velocity $v(x, n)$ given by (5.9)

$$v(x,n) \;=\; \begin{cases} -v_0\left(1 - \frac{F(x)}{nF_s}\right) & \text{for } n = 1, 2, \ldots, n_{tot} \\ 0 & \text{for } n = 0. \end{cases} \tag{5.43}$$

The simulation generates individual trajectories of this Markov process. For this purpose, time is discretized with time step Δt. In each time step $t \to t + \Delta t$ the number n of bound motors and the position x of the motors are updated according to the following rules

$$n \;\to\; \begin{cases} n-1 & \text{with probability} \quad \epsilon_n(x)\Delta t, \text{if } n > 0 \\ n+1 & \text{with probability} \quad \pi_n \Delta t, \text{if } n < n_{tot} \end{cases} \tag{5.44}$$

$$x \;\to\; x + \bar{\ell}/n \quad \text{with probability} \quad \omega(n, F)\ , \tag{5.45}$$

where $\omega(n, F)$ is the probability for stepping of one motor when n motors are active (i.e., bound) and reads

$$\omega(n, F) = v(n, F)\ \frac{\Delta t}{\bar{\ell}}\ n \tag{5.46}$$

and $\bar{\ell}$ is the step size and amounts 8 nm. One can also perform the simulations with a deterministic stepping, i.e.,

$$x \to x + v(n, x)\Delta t\ . \tag{5.47}$$

Results of simulations using the rule (5.47) are in very good agreement with the simulations using (5.46) for the time and lengths considered here, and we do not present these results in this work. The good agreement between the stochastic and deterministic method is caused by the time scale separation for stepping of motors $(100/s)$ and binding and rebinding processes $(1/s)$. One expects that for low ATP concentrations (the motors would walk slower) the difference between stochastic and deterministic method would be significant.

In detail, the probabilistic update of the motor number works as follows. For each step a random number r in the interval $(0, 1)$ is drawn. Then, the motor number n changes to $(n+1)$ if $r \leqslant \pi_n \Delta t$, and to $(n-1)$ if $\pi_\Delta t < r \leqslant \pi_n \Delta t + \epsilon_n(x)\Delta t$. Else, it remains unchanged. The hopping occurs if $\pi_n \Delta t + \epsilon_n(x)\Delta t < r \leqslant \pi_n \Delta t + \epsilon_n(x)\Delta t + \omega(n, F)$.

The results of simulations compared to the numerical analysis from previous section for $L = 25\ \mu m$ and $\pi = 0$ and $\pi_0 = 5s^{-1}$ are presented in Fig. 5.17 *a*) and *b*), respectively. Here,

the circles correspond to data from the MC simulations. We can now determine the mean first passage time τ also from the simulation results. The mean first passage time τ_{sim} is the average of the times when all motors unbind for the first time. In case of a cargo filament with contour length $L = 25\ \mu m$ and $\pi = 0$ (a) in Fig. 5.17) we get $\tau_{sim} = 2.2\ s$. This result agrees excellently with previous results from numerical analysis and the vanishing force equation for $p_n(t)$ (5.36). Since the simulations and the numerical results are in a very good agreement, we can say that for long cargo filaments and no rebinding the "semi"-stochastic model is sufficient and leads to good results for the mean first passage time τ. Note, that the extension-force relation (5.8) used in both cases is the same. One expects however a discrepancy between simulations and numerical results for long times t since in the latter method we use the mean value $\langle 1/n \rangle$ in every integration of the equation of motion (5.21).

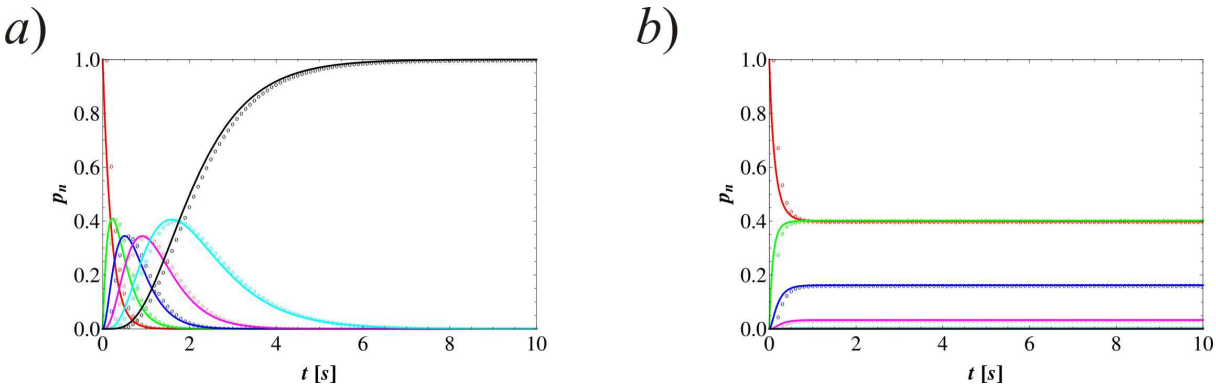

Figure 5.17: Numerical results from Section 5.5.2 compared to Monte Carlo simulation results for $p_n(t)$ for a cargo filament of contour length $L = 25\ \mu m$ and a) with no rebinding, i.e., $\pi = 0$ and b) with rebinding when $\pi_0 = 5s^{-1}$. The solid lines correspond to the probabilities $p_5(t)$ (red), $p_4(t)$ (green), $p_3(t)$ (blue), $p_2(t)$ (pink), $p_1(t)$ (cyan) and $p_0(5)$ (black) of the numerical analysis from section 5.5.2 and the circles are the MC simulations results (same colors). The time is given in seconds. The simulation results are in very good agreement with our numerical result from the previous section.

In Fig. 5.18 one can see that when the cargo filament becomes short, here $L = 5\ \mu m$, the MC simulations results (circles) and numerical result (solid lines) are in good agreement for a) $\pi = 0$ and b) $\pi_0 = 5s^{-1}$. In case of no rebinding in the system also the mean first passage time $\tau_{sim}[L = 5\ \mu m, \pi = 0] = 1.4\ s$ is in excellent agreement with the numerical result from Section 5.5.2.

However, the mean first passage time $\tau_{sim}[L = 5\ \mu m, \pi_0 = 5s^{-1}] = 17\ s$ diverges significantly from $\tau[L = 5\ \mu m, \pi = 5s^{-1}] = 100.63\ s$ determined numerically. The difference is caused by the mean field approximation in the numerical analysis from Section 5.5.2 where we take the mean value $\langle 1/n \rangle$, see (5.21) while the number of bound motors in MC simulations is exact. Also, in MC simulation the position of the motors, i.e., the distance $x(t)$, is a stochastic variable while in numerical approach $x(t)$ is a deterministic variable. Such discrepancy occurs also for $\tau_{sim}[L = 25\ \mu m, \pi_0 = 5s^{-1}] = 240\ s$ and $\tau[L = 25\ \mu m, \pi = 5s^{-1}] \approx 13825\ s$. However, results for $p_n(t)$ for short times regime are in a very good agreement also for positive rebinding rate π. One should remember that our model is restricted to small forces, i.e., short times, since we use the linear approximation (5.7) and the position of the motors is restricted to $-L \leqslant x \leqslant L$, see (5.10).

In a) and b) in Fig. 5.19 we plot the simulation results for the mean number of bound motors N as function of time t for cargo filament with contour length $L = 25\ \mu m$ and $L = 5\ \mu m$, respectively.

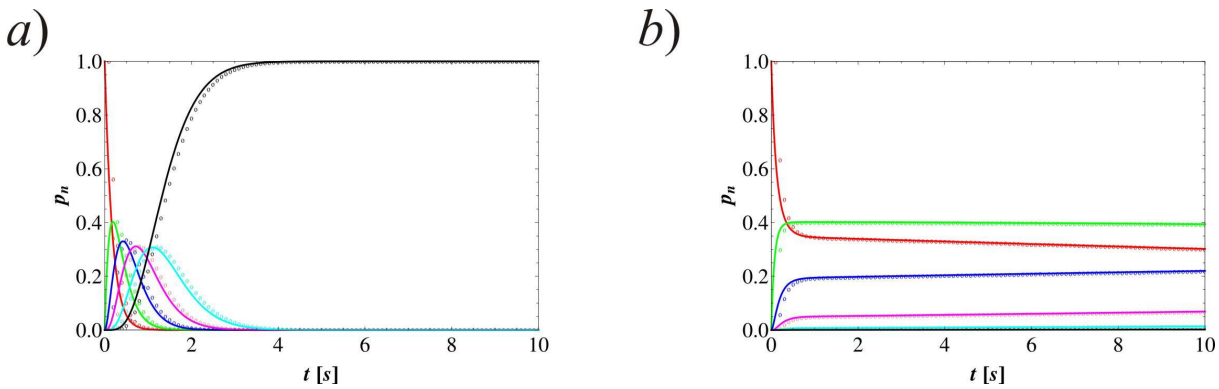

Figure 5.18: Comparison of the MC simulation results for $p_n(t)$ and the numerical solution from Section 5.5.2. Here, the cargo filament has the contour length $L = 5\ \mu m$ and a) there is no rebinding in the system, i.e., $\pi = 0$, b) there is positive rebinding $\pi_0 = 5s^{-1}$. The solid lines correspond to the probabilities $p_5(t)$ (red), $p_4(t)$ (green), $p_3(t)$ (blue), $p_2(t)$ (pink), $p_1(t)$ (cyan) and $p_0(5)$ (black) of the numerical analysis from section 5.5.2 and the circles are the MC simulations results (same colors). The time is given in seconds. The simulation results are in very good agreement with our numerical result from the previous section.

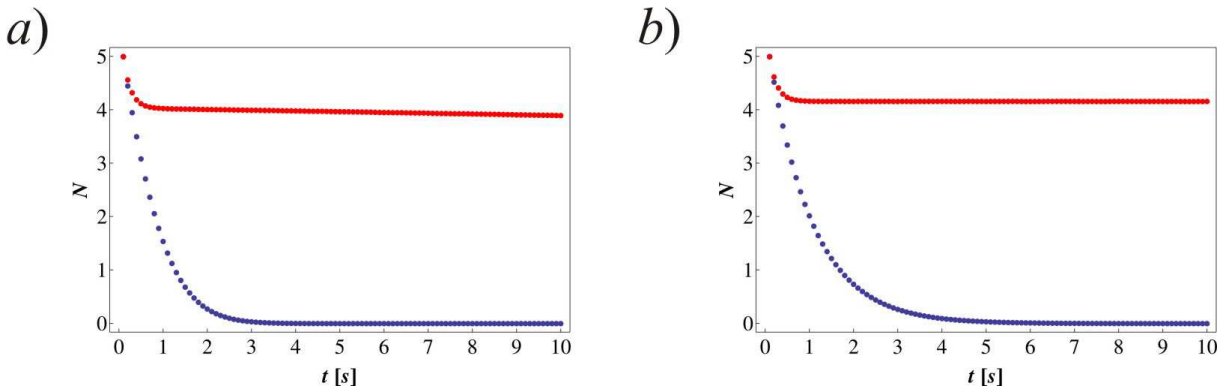

Figure 5.19: Simulation results for the mean number N of bound motors as function of time t in the absence (blue) and presence (red) of rebinding for the cargo filament of contour length $L = 25\ \mu m$, a) and the cargo filament of contour length $L = 5\ \mu m$, b).

Since we calculated the mean first passage time τ for the cargo filament of contour length $L = 25\ \mu m$ in four different ways, we can now compare all these results and get

$$\tau[L = 25\ \mu m, \pi = 0] = \begin{cases} \tau_{num} = 2.24\ s & \text{(numerical result)} \\ \tau_{F=0} = 2.28\ s & \text{(vanishing force result)} \\ \tau_{mf} = 2.20\ s & \text{(mean field approximation result)} \\ \tau_{sim} = 2.20\ s & \text{(simulations result)} \end{cases} \tag{5.48}$$

All four results are in an excellent agreement. Since the analytical solution (5.36) is a very good approximation for long cargo filaments one can clearly use it in order to determine the mean first passage time τ. For short filament with $L = 5\ \mu m$ and $\pi = 0$ the mean first passage times read

$$\tau[L = 5\ \mu m, \pi = 0] = \begin{cases} \tau_{num} = 1.42\ s & \text{(numerical result)} \\ \tau_{sim} = 1.4\ s & \text{(simulations result)} \end{cases} \tag{5.49}$$

Below we present the mean first passage times for the case of positive rebinding in the system

calculated numerically and from MC simulations for $L = 25\ \mu m$

$$\tau[L = 25\ \mu m, \pi_0 = 5s^{-1}] = \begin{cases} \tau_{num} = 13825\ s & \text{(numerical result)} \\ \tau_{sim} = 240\ s & \text{(simulations result)} \end{cases} \tag{5.50}$$

and for $L = 5\ \mu m$

$$\tau[L = 5\ \mu m, \pi_0 = 5s^{-1}] = \begin{cases} \tau_{num} = 100.63\ s & \text{(numerical result)} \\ \tau_{sim} = 17\ s & \text{(simulations result)} \end{cases} \tag{5.51}$$

The discrepancies prove that for systems with positive binding one should be carefully in using our "semi"-stochastic model for determining the mean first passage times. One expects that the main difference in results of the fully stochastic MC simulation (Markov process) and "semi"-stochastic numerical analysis (master equations) becomes significantly only in long times regime for positive binding rate π (in short times regime the probabilities $p_n(t)$ from numerical analysis and MC simulations are in very good agreement, see *b*) in Figs. 5.17 and 5.18). This is caused by the mean field approximation (5.21) we make in the "semi"-stochastic model. One could investigate different cases of the velocity of motors (i.e., very fast and very slow motors) in order to check the limits of the mean field approximation. One could also consider the differences between results using the mean values $\langle 1/n \rangle$ and $\langle n \rangle$ in the velocity-force relation of the motors (5.9).

5.8 Conclusions

In this chapter we presented a model of buckling of filaments under the action of molecular motors. A bunch of motors is linking two filaments, one firmly attached to the surface and one being a cargo. If motors exert a sufficient force on the cargo filament, which is pushed against a wall, it buckles. The distance of the motors corresponds to the projected length of the cargo filament. In this case the force in the velocity-force relation (5.9) and the Bell equation (5.11) depends on the position of motors. We presented a "semi"-stochastic model which describes the probability $p_n(t)$ that n molecular motors link the firmly attached (immobilized) filament with the cargo filament. We defined the mean first passage time until unbinding of all motors bound at $t = 0$. This time was calculated for two cases of contour length L of the cargo filament both in the absence and presence of the rebinding process in the system. We presented also a mean field theory for our model which is a good approximation in the case of small forces. Finally, we performed Monte Carlo simulations of the process of buckling under the action of molecular motors where the position of motors changes stochastically. The mean first passage times calculated from simulations and from numerical analysis were compared and are in perfect agreement with each other in the case both of long and short cargo filaments, when there is no rebinding in the system. Finally, we showed that for long cargo filaments and no rebinding one can easily use the vanishing force relation for $p_n(t)$ (5.36) determined analytically in the case of the force *independent* on the position. Also, in this case the mean first passage time gives an excellent agreement with simulation and numerical results. Therefore, the "semi"-stochastic approach, the mean field model from Section 5.6 and the vanishing force approach (Section 5.5.5) give very good results especially for long filaments, i.e., when the critical force $F_{c,0}$ becomes small. This clearly proves that our assumptions are good for such filaments.

Using two approaches we showed that for positive rebinding rates one can also apply the numerical approach in order to investigate the short times regime. In this regime the "semi"-stochastic model gives a very good approximation for the probabilities $p_n(t)$ as compared to the MC simulation results. However, the mean first passage time determined in simulations diverges from that determined in terms of the "semi"-stochastic model. The reason for this discrepancy is a mean field approximation we make in the "semi"-stochastic approach by using the mean $\langle 1/n \rangle$

in the velocity-force relation (5.21). We also showed that for positive rebinding rates the mean first passage time increases significantly.

Next step in creating a model for buckling of semiflexible filaments under the action of molecular motors would be the use of simulation data for the force-extension relation, see Chapter 4. Finally, in future one could consider a fully stochastic model for buckling under the action of molecular motors where the force $F(x)$ has two components, parallel and perpendicular to the direction of walking motors.

Chapter 6

Summary and Outlook

6.1 Summary

The aim of this work was to investigate buckling instabilities of semiflexible filaments in biological systems. After a short introduction about polymers, filaments and molecular motors we reviewed the buckling instability of rods on the macroscopic scale and introduced an analytical model for buckling of filaments in two spatial dimensions in the presence of thermal fluctuations and a "semi"-stochastic model for buckling of filaments under the action of molecular motors.

In Chapter 3 we studied the buckling instability of filaments or elastic rods in two spatial dimensions in the presence of thermal fluctuations. We presented an analytical solution based on a renormalization-like procedure where we integrate out short-wavelength fluctuations in order to obtain an effective theory governing the buckling instability. We calculated the resulting shift of the critical force by fluctuation effects, see (3.46). We found analytical expressions for the average projected filament length parallel to the force direction as a function of the applied force and as a function of the contour length of the filament as given by (3.59) and (3.67), respectively. These relations are presented for different stiffness parameters in Figs. 3.4 and 3.5. We found that, in the buckled state, thermal fluctuations lead to an increase in the mean projected length of the filament in the force direction, i.e., to a stretching of the buckled filament. As a function of the contour length, the mean projected length exhibits a cusp at the buckling instability, which becomes rounded by thermal fluctuations, see Fig. 3.5.

In Chapter 4 we presented Monte Carlo simulations for buckling of semiflexible filaments in the presence of thermal fluctuations. We investigated filaments in two spatial dimensions and confirmed our analytical results, see Fig. 4.3 and Fig. 4.6. We performed simulations both in tangent vector representation, see Fig. 4.3, and in tangent angle representation, see Fig. 4.8 Finally, we simulated buckling also in $d = 3$ and $d > 3$ spatial dimensions and showed that the increase in projected length by thermal fluctuations is less pronounced in higher dimensions and depends on the choice of boundary conditions.

In Chapter 5, which can be read separately, we presented a model for the buckling of semiflexible filaments under the action of molecular motors. We investigated a group of kinesin I motors with a microtubule as a cargo since all important model parameters are known from experiments. We studied a system in which a group of motors moves along a firmly attached (immobilized) filament carrying a second filament as a cargo. The cargo-filament is pushed against a wall and eventually buckles. Depending on boundary conditions we observe different buckling behaviors.

For a long cargo-filament the critical Euler force for buckling is much smaller than the stall force of a single molecular motor, which leads to buckling of the cargo-filament. We used an analytical linear approximation (5.8) of the resulting force-extension relation of the buckled filament. Using Bell-theory for unbinding of a motor and a linear velocity-force relation we obtained a Master equation for the probability $p_n(t)$ that n motors link both filaments at time t. Finally, we calculated the mean first passage time needed for unbinding of all linking motors which corresponds also to the transition between buckled and unbuckled state of cargo-filament. Our results show that for sufficiently long filaments the movement of kinesin motors is not affected by the load force generated by the cargo filament. Our numerical solution is confirmed by computer simulations, see Fig. 5.17 and 5.18.

6.2 Outlook

Our work predicts the increase of the critical force for buckling by thermal fluctuations in two spatial dimensions. The predictions of our model are, however, difficult to confirm in experiments, since experiments are more easily performed in three spatial dimensions, i.e., for filaments fluctuating in three directions.

The analytical model for the buckling of thermally fluctuating filaments can be extended to three spatial dimensions. However, the solution of the model in $d > 2$ is not trivial and can be performed only in the tangent vectors representation. Furthermore, several useful extensions of the model are possible, such as the introduction of a filament stretching energy for extensible filaments and the inclusion of torque moments at the ends of the filament.

For buckling by molecular motors we calculated the mean first passage time needed to unbound all motors acting on the cargo filament from the Master equation for the probabilities $p_n(t)$. With the help of our results, it should be possible to compare the numerical and analytical results for the mean first passage time with values determined in experiments. One expects that for long filaments the predicted mean first passage time would be in a very good agreement with experimental result.

Our model for buckling under the action of molecular motors could be extended in various ways. First, it could be extended by using the simulated force-extension curves of the buckled filament in the presence of thermal fluctuations instead of the linear approximation of these curves. Another extension is the introduction of two components of the load force, one parallel and one perpendicular to the direction of movement of motors. Finally, a full stochastic model for buckling under the action of molecular motors could be considered, where both the number of motors and also the position of motors are stochastic variables. Furthermore, the cargo initial shape or torque exerted on the cargo could be taken into account.

List of Symbols

$+$	plus end of the filament
$-$	minus end of the filament
a	microscopic cutoff, see Chapter 3
a_0	expansion coefficient, see Section 3.5.2
a_1	expansion coefficient, see Section 3.5.2
α	coefficients in Landau Free energy given by (3.42)
A_ν	coefficients in representation of $\epsilon(s)$, see (3.10)
b	bond length in discrete worm-like chain in tangent angle representation, see Chapter 4
β	coefficients in Landau free energy given by (3.44)
C	conserved energy, see (2.10)
C_1, C_2	constants in eigenfunction $\psi_\nu(s)$, see (3.13)
d	(spatial) dimension
$\partial_s \equiv \frac{\partial}{\partial s}$	partial derivative with respect to s
D	diameter of a polymer, see Section 1.2.1; distance of the projected end from the initial position, see (4.12)
$\mathcal{D}A_\nu$	path integral over all possible A_ν, see (3.18)
δ_{ij}	Kronecker delta
ϵ	expansion term, see (3.4)
$\epsilon(F)$	unbinding rate in case of single motor, see (5.2)
$\epsilon_n(F)$	unbinding rate in case of n bound motors, see (5.11)
E_b	elastic bending energy, see (2.1)
E_F	external force energy, see (2.2)
E_{init}	initial energy of the system, see Section 4.1.1
E_l	sum of bending and pulling energies, see (2.27)
E_{new}	new energy after random change of the initial energy, see Section 4.1.1
ΔE	energy change, see Section 4.1.1
E_Y	Young's modulus, see Section 1.4
$\mathbf{F}$	compressive force vector
F	absolute value of the force vector, $F \equiv \lvert\mathbf{F}\rvert$
$\mathcal{F}$	elliptic integral of the first kind, see (2.12)
F_c	critical force for buckling, also called Euler force at $T > 0$, see (3.46)
$F_{c,0}$	critical force for buckling, also called Euler force at $T = 0$, see (2.15)
F_d	motor detachment force
$F_{d,n}$	detachment force for a giant motor complex made up from n motors, see Section 5.5.3
F_{eff}	effective compressive force, see (3.49)
F_i	intersection force, see (3.65)
F_l	load force, see Chapter 5
F_s	motor stall force, see Chapter 5
F_τ	value of force F when the las motor unbinds, see (5.26)
$\bar{F}$	reduced force given by $\bar{F} \equiv F/F_{c,0}$
$\tilde{F}_{crit}$	critical force for decomposition of the filaments cluster, see Section 5.5.4
G	Gibbs free energy, see (3.6)
γ	rebinding rate, $\gamma \equiv \pi/\epsilon_0$
Γ	Gamma function
$\mathcal{G}$	elliptic integral of the second kind, see (2.20)

$h(\bar{F})$	sum of higher modes, see (3.43)
$\mathcal{H}$	Hamiltonian
$\mathcal{H}_2$	Hamiltonian with terms up to quadratic order, see (3.34)
$\mathcal{H}_4$	Hamiltonian with terms up to quartic order, see (3.34)
$\mathcal{H}_H$	Heisenberg hamiltonian, see (3.27)
$\mathcal{H}_{WLC}$	worm-like chain Hamiltonian, see (1.11)
$\mathcal{H}_{dWLC}$	discrete worm-like chain Hamiltonian, see (4.6)
i	index denoting being in the state i, see Chapter 4
I	moment of inertia, see Section 1.4
$\mathrm{I}_\nu(x)$	the modified Bessel function, see Section 3.5.2
j	index denoting the system being in the state j, see Chapter 4
κ	bending rigidity of a rod (Chapter 2) or a filament (Chapters $3-5$)
κ_0	unrenormalized bending rigidity of a filament, see (1.2)
K	wave vector, see (3.15)
$\mathrm{K}_\nu(x)$	the modified Bessel function, see Section 3.5.2
l	bond length in ideal chain models, see Section 1.3
ℓ	infinitesimal change of the length scale, see Section 3.5.1
	overlapping region length, see Fig. 5.4
$\bar{\ell}$	step size of a molecular motor, see Section 5.7.1
L	contour length of filament
L_l	fixed loop length, see (2.28)
L_K	Kuhn length, see Section 1.3
$L_{c,0}$	critical length for buckling at $T=0$, see (2.16)
L_c	critical length for buckling at $T>0$, see (3.47)
$\bar{L}_m$	contour length where the mean projected length $\langle L_{\|\|}\rangle$ becomes maximal, see (3.69)
L_p	persistence length of a polymer, see (1.1)
$\bar{L}_{c,0}$	reduced length given by $\bar{L}\equiv L/L_{c,0}$
$L_{\|\|}$	projected length in the absence of thermal fluctuations, see Chapter 2
$\langle L_{\|\|}\rangle$	mean projected length in the presence of thermal fluctuations, see Chapter 3
λ_ν	eigenvalues of eigenvector $\psi(s)$, see (3.16)
Λ	large scale momentum cutoff, see Section 3.5.1
m	index denoting the mode, see Chapter 3
M	bending moment, see (1.16)
N	maximal wave number given by $N=L/a$, see Chapter 3;
	number of beads in the discrete worm-like chain Hamiltonian, see Chapter 4;
	mean number of bound (linking) molecular motors, see Chapter 5
N_A	Avogadro constant
n	number of bonds in Chapter 1; in Chapter 3 the index denoting the mode; in Chapter 5 number of motors bound to filament, i.e., number of linking motors
ν	wave number, see Section 3.3
ν	indexes of the modified Bessel functions, see Section 3.5.2
n_0	initial number of motors bound to the filament an $t=0$, see Chapter 5
n_{tot}	total number of motors in the system, see Chapter 5
$\mathcal{O}$	higher order terms, see e.g. (2.22)
$\Omega(D)$	probability that the end of the filament projected on the xy-plane is at the distance D from the initial position at $x=y=0$, see Section 4.4.3
$\mathcal{P}(y)$	function defining the partition function (3.56), see (3.57)
$\phi(s)$	tangent angle, see Section 2.1
ϕ_i	tangent angle $\phi_i\equiv\phi(ib)$, see Section 4.3.3
$\tilde{\phi}_n$	n-th Fourier coefficient, see (3.32) and 3.33
ϕ_{max}	maximal value of the angle ϕ between spring and the vertical, see Section 2.2
$\pi(F_l)$	load-dependent binding rate of single motor, see Section 5.1.2
π	load-independent binding rate of single motor, see Section 5.1.2
π_0	zero-force binding rate of single motor, see Section 5.1.2
π_n	binding rate, see (5.12)
Φ	N-component field in general non-linear sigma model, see Section 3.4
$\psi_\nu(s)$	eigenfunctions of the operator $\left[-\frac{\kappa}{2}\partial_s^2-\frac{1}{2}F\right]$, see (3.10)
R_c	radius of curvature, see Section 1.4
R_l	radius of circular loop, see Section 2.2.3

s	arc length
$\mathbf{S}$	classical spin N-component vector in non-linear sigma model, see Section 3.4
$\mathbf{S}_i$	classical spin vector on the i-th node of the lattice, see Section 3.4
S_{cross}	cross section, see Section 1.4
σ	bond length in discrete worm-like chain, see Section 4.2
$\mathbf{t}(s)$	unit tangent vector, see Section 2.1
$\mathbf{t}_i$	unit tangent vector on the i-th bead of the discrete worm-like chain, see Section 4.2
t	time
t_0	time $t = 0$, see Chapter 5
T	absolute temperature in k_B units
$\bar{t}$	dimensionless time defined by $\bar{t} \equiv tv_0/L$, see Section 5.4
$\bar{T}$	reduced temperature, see (3.38)
τ	total mean first passage time for transition from state with n_0 bound motors to a state with $n = 0$ bound motors, see Section 5.23
τ_n	mean first passage time for transition from state with n bound motors to a state with $n - 1$ or $n + 1$ bound motors, see (5.22)
$\tau[L, \pi]$	total mean first passage time τ in case of cargo filament of contour length L and binding rate π, see Chapter 5
τ_{num}	mean first passage time τ established numerically, see Section 5.5.3
τ_{mf}	mean first passage time τ established in terms of the mean field approximation, see Section 5.6
τ_{sim}	mean first passage time τ established in simulations, see Section 5.7
v	velocity of a single motor or a bunch of motors, see Chapter 5
v_A	backward velocity of motor in the absence of the load force, see Section 5.1.4
v_B	backward velocity of motor in the absence of the load force, see Section 5.1.4
v_0	single motor forward velocity in the absence of the load force, see Section 5.1.4
V	crosslinking motor velocity, see Fig. 5.4
$V(\phi)$	energy potential, see Section 2.2
$\hat{V}$	microtubule poleward velocity, see Fig. 5.4
V_{ij}	pair interaction in non-linear sigma model, see (3.4)
$w_i(t)$	probability of being in state i at time t, see Chapter 4
$W(i \to j)$	transition probability from state i to state j per unit time, see Chapter 4
x	position of a motor or bunch of motors along the clamped filament; distance from the wall, see Chapter 5
x_c	extension of energy barrier between the bound and unbound state, see Section 5.1.3
x, y, z	Cartesian coordinates
ξ_ν	eigenvalue λ_ν over temperature, see (3.21)
Z	partition function

List of abbreviations

ADP	adenosine diphosphate
ATP	adenosine triphosphate
DNA	deoxyribonucleic acid
dWLC	discrete worm-like chain
GTP	guanosine triphosphate
MC	Monte Carlo
MT	microtubule
P_i	inorganic phosphate
RG	renormalization group
WLC	worm-like chain

Bibliography

[1] J. M. Tymoczko L. Stryer, J. M. Berg. *Biochemistry. 5th edition.* Freeman, New York, 2002.

[2] Elizabeth A. Shephard Hugh A. White Claudia G. Wiedemann Stephen R. Bolsover, Jeremy S. Hyams. *Cell Biology. A Short Course. Second edition.* John Wiley and Sons, Inc., Hoboken, New Jersey, 2004.

[3] http://en.wikipedia.org/wiki/Cytoskeleton.

[4] B. Alberts, D. Bray, A. Johnson, J. Lewis, M. Raff, K. Roberts, and P. Walter. *Essential cell biology. An introduction to the molecular biology of the cell.* Garland, New York, 1998.

[5] M. Doi and S. F. Edwards. *The Theory of Polymer Dynamics, Clarendon.* Oxford, 1986.

[6] P.G. de Gennes. *Scaling Concepts in Polymer Physics.* Cornell University Press, 1979.

[7] P. Gutjahr, R. Lipowsky, and J. Kierfeld. Persistence length of semiflexible polymers and bending rigidity renormalization. *Europhys. Lett*, 76(6):994–1000, 2006.

[8] J. Kierfeld, K. Baczynski, P. Gutjahr, and R. Lipowsky. Semiflexible Polymers and Filaments: From Variational Problems to Fluctuations. *AIP Conference Proceedings*, 1002:151, 2008.

[9] W. H. Taylor and P. J. Hagerman. Application of the method of phage T 4 DNA ligase-catalyzed ring-closure to the study of DNA structure. II: NaCl-dependence of DNA flexibility and helical repeat. *Journal of molecular biology*, 212(2):363–376, 1990.

[10] B. Alberts. *Molecular biology of the cell.* Routledge, 1989.

[11] F. Gittes. Flexural rigidity of microtubules and actin filaments measured from thermal fluctuations in shape. *The Journal of Cell Biology*, 120(4):923–934, 1993.

[12] H. Berk A. Zipursky S. L. Matsudaira P. Baltimore D. Lodish and Darnell J. E. *Molecular Cell Biology.* W. H. Freeman and Company, New York, 2000.

[13] W. H. Taylor and P. J. Hagerman. Application of the method of phage T 4 DNA ligase-catalyzed ring-closure to the study of DNA structure. II: NaCl-dependence of DNA flexibility and helical repeat. *Journal of molecular biology*, 212(2):363–376, 1990.

[14] J. Käs, H. Strey, and E. Sackmann. Direct imaging of reptation for semiflexible actin filaments. *Nature*, 368(6468):226–229, 1994.

[15] C. Dekker et al. Carbon nanotubes as molecular quantum wires. *Physics Today*, 52:22–30, 1999.

[16] M. Sano, A. Kamino, J. Okamura, and S. Shinkai. Ring closure of carbon nanotubes, 2001.

[17] A. Amzallag, C. Vaillant, M. Jacob, M. Unser, J. Bednar, J. D. Kahn, J. Dubochet, A. Stasiak, and J. H. Maddocks. 3D reconstruction and comparison of shapes of DNA minicircles observed by cryo-electron microscopy. *Nucleic Acids Research*, 34(18):e125, 2006.

[18] D.M. Hatters, C.A. MacRaild, R. Daniels, W.S. Gosal, N.H. Thomson, J.A. Jones, J.J. Davis, C.E. MacPhee, C.M. Dobson, and G.J. Howlett. The circularization of amyloid fibrils formed by apolipoprotein C-II. *Biophysical journal*, 85(6):3979–3990, 2003.

[19] M. Rubinstein and R. H. Colby. *Polymer physics.* Oxford University Press, USA, 2003.

[20] O. Kratky and G. Porod. Rontgenuntersuchung aufgeloster fadenmolekule. *Recl. Trav. Chim. Pays-Bas*, 68:1106–1122, 1949.

[21] L. D. Landau and E. M. Lifshitz. *Statistical Physics, Pt. 1.* Pergamon Press Oxford, 1980.

[22] J. Howard. *Mechanics of Motor Proteins and the Cytoskeleton.* Sinauer Associates, Sunderland, 2001.

[23] R. D. Vale. The molecular motor toolbox for intracellular transport. *Cell*, 112:467–480, 2003.

[24] K. Baczynski, R. Lipowsky, and J. Kierfeld. Stretching of buckled filaments by thermal fluctuations. *Physical Review E*, 76(6):61914, 2007.

[25] W. A. Oldfather, C. A. Ellis, and Donald M. Brown. Leonhard Euler's Elastic Curves. *Isis*, 20(1):72, 1933.

[26] S. S. Antmann. *Nonlinear Problems of Elasticity*. Springer, New York, 1995.

[27] L. D. Landau, E. M. Lifshitz, J. B. Sykes, W. H. Reid, A. M. Kosevich, and Pitaevskiĭ. *Theory of elasticity*.

[28] http://www.memagazine.org/contents/current/webonly/webex418.html.

[29] http://en.wikipedia.org/wiki/Buckling.

[30] L. D. Landau, E. M. Lifshitz, and R. J. Donnelly. *Mechanics, Vol. I of Course on Theoretical Physics*, volume 40. AAPT, 1972.

[31] M. Abramowitz and I.A. Stegun. *Handbook of Mathematical Functions with Formulas, Graphs, and Mathematical Table*. Courier Dover Publications, 1965.

[32] N. K. Lee, A. Johner, and S. C. Hong. Compressing a rigid filament: Buckling and cyclization. *The European Physical Journal E-Soft Matter*, 24(3):229–241, 2007.

[33] M. Emanuel, H. Mohrbach, M. Sayar, H. Schiessel, and I. M. Kulić. Buckling of stiff polymers: Influence of thermal fluctuations. *Physical Review E*, 76:061907, 2007.

[34] J. R. Blundell and E. M. Terentjev. Buckling of semiflexible filaments under compression. *arXiv.org cond-mat.soft*, 0902.2079v2, 2009.

[35] J. Kierfeld, P. Gutjahr, T. Kuhne, P. Kraikivski, and R. Lipowsky. Buckling, Bundling, and Pattern Formation: From Semi-Flexible Polymers to Assemblies of Interacting Filaments. *Journal of Computational and Theoretical Nanoscience*, 3(6):898, 2006.

[36] M. Dogterom and B. Yurke. Measurement of the Force-Velocity Relation for Growing Microtubules. *Science*, 278(5339):856, 1997.

[37] F. Gittes, E. Meyhofer, S. Baek, and J. Howard. Directional loading of the kinesin motor molecule as it buckles a microtubule. *Biophysical Journal*, 70(1):418–429, 1996.

[38] M. Elbaum, D. Kuchnir Fygenson, and A. Libchaber. Buckling Microtubules in Vesicles. *Physical Review Letters*, 76(21):4078–4081, 1996.

[39] R. E. Goldstein and A. Goriely. Dynamic buckling of morphoelastic filaments. *Physical Review E*, 74(1):10901, 2006.

[40] P. L. Hansen, D. Svenšek, V. Adrian Parsegian, and R. Podgornik. Buckling, fluctuations, and collapse in semiflexible polyelectrolytes. *Physical Review E*, 60(2):1956–1966, 1999.

[41] L. Golubović, D. Moldovan, and A. Peredera. Dynamics of the Euler Buckling Instability. *Physical Review Letters*, 81(16):3387–3390, 1998.

[42] P. Ranjith and P. B. S. Kumar. Dynamics of Folding in Semiflexible Filaments. *Physical Review Letters*, 89(1):18302, 2002.

[43] T. Odijk. Microfibrillar buckling within fibers under compression. *The Journal of Chemical Physics*, 108:6923, 1998.

[44] S. M. Carr, W. E. Lawrence, and M. N. Wybourne. Accessibility of quantum effects in mesomechanical systems. *Physical Review B*, 64(22):220101, 2001.

[45] H.B. Callen. Thermodynamics and an Introduction to Thermostatics. *New York*, 1985.

[46] J. Zinn-Justin. *Phase Transitions and Renormalization Group*. Oxford University Press, USA, 2007.

[47] M. Kaku. *Quantum field theory: a modern introduction*. Oxford University Press, 1993.

[48] G. S. Joyce. Classical Heisenberg model. *J. Math. Phys Phys Rev*, 155:478, 1964.

[49] A. M. Polyakov. *Gauge Fields and Strings*. Harwood Academic Pub, 1987.

[50] L. R. G. Treloar. *The Physics of Rubber Elasticity*. Oxford University Press, USA, 2005.

[51] K. Binder. *Monte Carlo and Molecular Dynamics Simulations in Polymer Science*. Oxford Univer-

sity Press, USA, 1995.

[52] C. W. Gardiner. Handbook of stochastic methods(for physics, chemistry and the natural sciences). *Springer series in synergetics*.

[53] S. Karlin and H.M. Taylor. *A First Course in Stochastic Processes*. Academic Press, 1975.

[54] S. Karlin and H.M. Taylor. *Solutions to problems-A first course in stochastic processes*. Academic Press New York, 1975.

[55] N. Metropolis, A.W. Rosenbluth, M.N. Rosenbluth, A.H. Teller, and E. Teller. Equation of State Calculations by Fast Computing Machines. *The Journal of Chemical Physics*, 21(6):1087, 1953.

[56] M. E. J. Newman and G. T. Barkema. *Monte Carlo methods in statistical physics*. Oxford University Press, USA, 1999.

[57] M. Hjorth-Jensen. *Computational Physics*. University of Oslo, 2008.

[58] J.R. Taylor. *An introduction to error analysis*. University Science Books Mill Valley, 1997.

[59] J. F. Marko and E. D. Siggia. Stretching DNA. *Macromolecules*, 28(26):8759–8770, 1995.

[60] A. Gholami, J. Wilhelm, and E. Frey. Entropic forces generated by grafted semiflexible polymers. *Physical Review E*, 74(4):41803, 2006.

[61] S. Klumpp and R. Lipowsky. Cooperative cargo transport by several molecular motors. *Proceedings of the National Academy of Sciences*, 102(48):17284–17289, 2005.

[62] P. Kraikivski, R. Lipowsky, and J. Kierfeld. Enhanced ordering of interacting filaments by molecular motors. *Physical review letters*, 96(25):258103, 2006.

[63] M.J.I. Müller, S. Klumpp, and R. Lipowsky. Tug-of-war as a cooperative mechanism for bidirectional cargo transport by molecular motors. *Proceedings of the National Academy of Sciences*, 105(12):4609, 2008.

[64] W.O. Hancock and J. Howard. Processivity of the motor protein kinesin requires two heads. *Journal of Cell Biology*, 140(6):1395–1405, 1998.

[65] E. Meyhofer and J. Howard. The Force Generated by a Single Kinesin Molecule Against an Elastic Load. *Proceedings of the National Academy of Sciences*, 92(2):574–578, 1995.

[66] K. Visscher, M. J. Schnitzer, and S. M. Block. Single kinesin molecules studied with a molecular force clamp. *Nature*, 400(6740):184–9, 1999.

[67] http://www.imb-jena.de/www_elmi/.

[68] H. A. Kramers. Brownian motion in a field of force and the diffusion model of chemical reactions. *Physica, 7*, (4), 1940.

[69] G. I. Bell. Models for the specific adhesion of cells to cells. *Science*, 200(4342):618, 1978.

[70] N. G. van Kampen. Stochastic Processes in Physics and Chemistry. *Amsterdam, New York*, 1992.

[71] N. J. Carter and R. A. Cross. Mechanics of the kinesin step. *Nature*, 435(7040):308–312, 2005.

[72] A. Straube, G. Hause, G. Fink, and G. Steinberg. Conventional Kinesin Mediates Microtubule-Microtubule Interactions In Vivo. *Molecular Biology of the Cell*, 17(2):907–916, 2006.

[73] H. Kojima, E. Muto, H. Higuchi, and T. Yanagida. Mechanics of single kinesin molecules measured by optical trapping nanometry. *Biophysical Journal*, 73(4):2012–2022, 1997.

[74] A. J. Hunt, F. Gittes, and J. Howard. The force exerted by a single kinesin molecule against a viscous load. *Biophysical Journal*, 67(2):766–781, 1994.

[75] M. Nishiyama, H. Higuchi, and T. Yanagida. Chemomechanical coupling of the forward and backward steps of single kinesin molecules. *Nature Cell Biology*, 4(10):790–797, 2002.

[76] K. Svoboda and S. M. Block. Force and velocity measured for single kinesin molecules. *Cell*, 77(5):773–84, 1994.

[77] S. Toba, T. M. Watanabe, L. Yamaguchi-Okimoto, Y. Y. Toyoshima, and H. Higuchi. Overlapping hand-over-hand mechanism of single molecular motility of cytoplasmic dynein. *Proceedings of the National Academy of Sciences*, 103(15):5741–5745, 2006.

[78] R. D. Vale, T. Funatsu, D. W. Pierce, L. Romberg, Y. Harada, and T. Yanagida. Direct observation of single kinesin molecules moving along microtubules. *Nature*, 380(6573):451–453, 1996.

[79] S. J. King and T. A. Schroer. Dynactin increases the processivity of the cytoplasmic dynein motor. *Nature Cell Biology*, 2:20–24, 2000.

[80] M. Nishiura, T. Kon, K. Shiroguchi, R. Ohkura, T. Shima, Y. Y. Toyoshima, and K. Sutoh. A Single-headed Recombinant Fragment of Dictyostelium Cytoplasmic Dynein Can Drive the Robust Sliding of Microtubules. *Journal of Biological Chemistry*, 279(22):22799, 2004.

[81] C. Leduc, O. Campas, K. B. Zeldovich, A. Roux, P. Jolimaitre, L. Bourel-Bonnet, B. Goud, J.F. Joanny, P. Bassereau, and J. Prost. From the Cover: Cooperative extraction of membrane nanotubes by molecular motors. *Proceedings of the National Academy of Sciences*, 101(49):17096, 2004.

[82] S. L. Reck-Peterson, A. Yildiz, A. P. Carter, A. Gennerich, N. Zhang, and R. D. Vale. Single-Molecule Analysis of Dynein Processivity and Stepping Behavior. *Cell*, 126(2):335–348, 2006.

[83] M. J. Schnitzer, K. Visscher, and S. M. Block. Force production by single kinesin motors. *Nature Cell Biology*, 2:718–723, 2000.

[84] R. Mallik, D. Petrov, S.A. Lex, S.J. King, and S.P. Gross. Building Complexity: An In Vitro Study of Cytoplasmic Dynein with In Vivo Implications. *Current Biology*, 15(23):2075–2085, 2005.

[85] H. Sakakibara, H. Kojima, Y. Sakai, E. Katayama, and K. Oiwa. Inner-arm dynein c of Chlamydomonas flagella is a single-headed processive motor. *Nature*, 400(6744):586–90, 1999.

[86] M. A. Welte, S. P. Gross, M. Postner, S. M. Block, and E. F. Wieschaus. Developmental regulation of vesicle transport in Drosophila embryos: forces and kinetics. *Cell*, 92(4):547–557, 1998.

[87] M. E. Janson, M. E. de Dood, and M. Dogterom. Dynamic instability of microtubules is regulated by force The online version of this article includes supplemental material., 2003.

[88] M. Elbaum, D. Kuchnir Fygenson, and A. Libchaber. Buckling Microtubules in Vesicles. *Physical Review Letters*, 76(21):4078–4081, 1996.

[89] M. Dogterom, J. W. J. Kerssemakers, G. Romet-Lemonne, and M. E. Janson. Force generation by dynamic microtubules. *Current Opinion in Cell Biology*, 17(1):67–74, 2005.

[90] D. R. Kovar and T. D. Pollard. Insertional assembly of actin filament barbed ends in association with formins produces piconewton forces. *Proceedings of the National Academy of Sciences*, 101(41):14725–14730, 2004.

[91] D. Drubin, A. Straube, M. Brill, B. R. Oakley, T. Horio, and G. Steinberg. Microtubule Organization Requires Cell Cycle-dependent Nucleation at Dispersed Cytoplasmic Sites: Polar and Perinuclear Microtubule Organizing Centers in the Plant Pathogen Ustilago maydis. *Molecular Biology of the Cell*, 14(2):642–657, 2003.

[92] R. E. Campbell, O. Tour, A. E. Palmer, P. A. Steinbach, G. S. Baird, D. A. Zacharias, and R. Y. Tsien. A monomeric red fluorescent protein. *Proceedings of the National Academy of Sciences*, 99(12):7877, 2002.

[93] L. Cassimeris. Real-time observations of microtubule dynamic instability in living cells. *The Journal of Cell Biology*, 107(6):2223–2231, 1988.

[94] C. P. Brangwynne, F. C. MacKintosh, and D. A. Weitz. Force fluctuations and polymerization dynamics of intracellular microtubules. *Proceedings of the National Academy of Sciences*, 104(41):16128, 2007.

[95] F. J. Nedlec, T. Surrey, A. C. Maggs, and S. Leibler. Self-organization of microtubules and motors. *Nature*, 389(6648):305, 1997.

[96] T. Wittmann, A. Hyman, and A. Desai. The spindle: a dynamic assembly of microtubules and motors. *Nature Cell Biology*, 3:E28–E34, 2001.

[97] T. J. Mitchison and E. D. Salmon. Mitosis: a history of division. *Nature Cell Biology*, 3:E17–E21, 2001.

[98] D. J. Sharp, G. C. Rogers, and J. M. Scholey. Microtubule motors in mitosis. *Nature*, 407(6800):41–7, 2000.

[99] T. M. Kapoor, T. U. Mayer, M. L. Coughlin, and T. J. Mitchison. Probing Spindle Assembly Mechanisms with Monastrol, a Small Molecule Inhibitor of the Mitotic Kinesin, Eg5. *The Journal of Cell Biology*, 150(5):975–988, 2000.

[100] D. T. Miyamoto, Z. E. Perlman, K. S. Burbank, A. C. Groen, and T. J. Mitchison. The kinesin Eg5 drives poleward microtubule flux in Xenopus laevis egg extract spindles Abbreviation used in this

paper: FSM, fluorescent speckle microscopy. *The Journal of Cell Biology*, 167(5):813–818, 2004.

[101] G. Goshima and R.D. Vale. The roles of microtubule-based motor proteins in mitosis: comprehensive RNAi analysis in the Drosophila S2 cell line. *The Journal of Cell Biology*, 162(6):1003, 2003.

[102] D. J. Sharp, K. L. McDonald, H. M. Brown, H. J. Matthies, C. Walczak, R. D. Vale, T. J. Mitchison, and J. M. Scholey. The Bipolar Kinesin, KLP61F, Cross-links Microtubules within Interpolar Microtubule Bundles of Drosophila Embryonic Mitotic Spindles. *The Journal of Cell Biology*, 144(1):125–138, 1999.

[103] L. C. Kapitein, E. J. Peterman, B. H. Kwok, J. H. Kim, T. M. Kapoor, and C. F. Schmidt. The bipolar mitotic kinesin Eg5 moves on both microtubules that it crosslinks. *Nature*, 435(7038):114–118, 2005.

[104] R. B. Nicklas. Measurements of the force produced by the mitotic spindle in anaphase. *The Journal of Cell Biology*, 97(2):542–548, 1983.

[105] T. J. Mitchison, P. Maddox, A. Groen, L. Cameron, Z. Perlman, R. Ohi, A. Desai, E. D. Salmon, and T. M. Kapoor. Bipolarization and Poleward Flux Correlate during Xenopus Extract Spindle Assembly. *Molecular Biology of the Cell*, 15(12):5603–5615, 2004.

[106] S.L. Rogers, G.C. Rogers, D.J. Sharp, and R.D. Vale. Drosophila EB1 is important for proper assembly, dynamics, and positioning of the mitotic spindle The online version of this article includes supplemental material. *The Journal of Cell Biology*, 158(5):873–884, 2002.

[107] O. Campas, J. Casademunt, and I. Pagonabarraga. Dynamic stability of spindles controlled by molecular motor kinetics. *Europhysics Letters*, 81(4):48003, 2008.

[108] K. Bloom. Nuclear migration: Cortical anchors for cytoplasmic dynein. *Current Biology*, 11(8):326–329, 2001.

[109] G. A. Dunn. A 1, 2, 3 in light microscopy. *Nature*, 408(23):16128, 2000.

[110] S. Wolfram. *The mathematica book*. Cambridge university press, 1999.

[111] S. Redner. *A Guide to First-Passage Processes*. Cambridge University Press, 2001.

[112] T. Erdmann and U. S. Schwarz. Stochastic dynamics of adhesion clusters under shared constant force and with rebinding. *The Journal of chemical physics*, 121:8997, 2004.

[113] T. Erdmann and U. S. Schwarz. Stability of adhesion clusters under constant force. *Physical Review Letters*, 92(4), 2004.

[114] D. A. McQuarrie. Kinetics of small systems I. *Journal of Chemical Physics*, 38(433), 1963.

[115] M. J. I. Müller. *private communications*.

[116] D. W. Heermann. *Computer simulation methods: in theoretical physics*. Springer-Verlag New York, Inc. New York, NY, USA, 1986.

Acknowledgments

At the end I would like to thank the people who supported me during my work on this thesis.

First of all I thank my supervisor Prof. Dr. Reinhard Lipowsky for encouraging me to work on the topic of buckling of filaments and buckling under the action of molecular motors, for all his ideas, help and financial support during my work at Max Planck Institute of Colloids and Interfaces.

I am also very grateful to Prof. Dr. Jan Kierfeld for introducing me to the topic of filaments, their buckling instabilities and their buckling under the action of molecular motors. Our discussions, his ideas and generous help and support, questions and patience made this thesis possible. Thank you.

I am very grateful to Dr. Bartosz Różycki for great discussions (not only about physics), his great help and comments.

I thank Dr. Melanie J. I. Müller very much for help in getting the simulation results for buckling under the action of molecular motors, her support, helpful discussions about motors and for carefully proofreading parts of the manuscript. And for all LaTeX tips.

I would like to thank also Dr. Angelo Valleriani and Dr. Christian Seidel for great organization of department workshops which always gave a great opportunity for discussions. Finally, I want to thank all my colleagues and coworkers for stimulating discussions and a great time in Golm and all members of our IT group for help and technical support.

Finally, I want to thank my beloved wife and my parents, the best parents a kid could hope for. For their help, support and faith in me and my scientific work ... for everything.

... and Thanks for All the Fish